Modelling Study of the Hydrodynamic Expansion of a

Laser Ablation Plume of Lithium in Vacuum

A Thesis for the Degree of

Doctor of Philosophy

By

Mark Stapleton, B Sc

Centre for Laser Plasma Research

National Centre for Plasma Science and Technology

School of Physical Sciences

Dublin City University

Research Supervisor

Dr J P Mosnier

December 2003

Declaration

I hereby certify that this material, which I now submit for assessment on the programme of study leading to the award of degree of Doctor of Philosophy is entirely my own work and has not been taken from the work of others save and to the extent that such work has been cited and acknowledged within the text of my work.

Signed: _Mark Hamilton_ ID No.: _99145170_

Candidate

Date: _30-1-2004_

Contents

Acknowledgements

Abstract

This work is concerned with the study of the important physical processes present in a laser ablation lithium plasma plume expanding into vacuum A numerical model has been developed encompassing three main areas, namely, hydrodynamics, atomic physics and radiative transfer and spectroscopy

A self-similar expansion model has been employed to study the hydrodynamics A comparison between the isothermal and isentropic self-similar solutions has been performed over a wide range of experimental initial conditions with varying fluence, laser wavelength and target spot size The effect of these variations is seen, where one of these models predicts experimental observations more accurately, depending on the initial conditions present Both models have been modified to include the bulk motion of the plasma by considering the pressure exerted by the expanding plume onto the target

The steady state collisional radiative model was used to calculate the electron, ion and energy level populations of lithium neutral in the expanding plume and is used as a post-processor to the hydrodynamics model The validity conditions of various equilibrium models and steady state conditions have been assessed, with particular emphasis on the spatial and temporal regions applicable to local thermodynamic equilibrium (LTE)

The information taken from the first two models allows the calculation of the full radiative transfer equation through plasma chords parallel to the target surface Results from this calculation have been compared with experimental time-integrated spectra This model was also used to explain a well-known anomalous line intensity ratio between two strong emission lines in neutral lithium produced in a laser ablation plasma

Chapter 1

Theory

1.1 Introduction

This chapter gives a description of the theoretical aspects of this work, paying particular attention to conditions relevant to the pulsed laser deposition (PLD) process As this work concerns the development of a complete single model that is capable of describing the laser plasma expansion, this chapter will give a detailed background of the different models currently used

This chapter is split into three main sections The first section concerns the definition and criterion for the existence of plasma This will lead to the description of plasma creation using a pulsed laser, particularly, in the regime of interest The models for plasma expansion dynamics will be introduced, with an emphasis on hydrodynamics models The following main section concerns the atomic physics within the plasma and how this may be analysed using the various equilibrium models available Finally, the theory of radiation transport and spectral analysis in plasma will be outlined This will include the theory required for analysing radiation transport and how synthetic spectra may be produced with a description of the different broadening mechanisms possible in a laser ablation

plasma

The International System of Units (SI) is used throughout this work unless otherwise stated

1.2 Plasma Definition

In this work, plasma with properties similar to that of a gas is of primary interest Hence, there is a necessity for the determination of regimes where a plasma may be approximately represented as a gas In a gas, particles will follow a straight line trajectory for much of the time suffering occasional collisions with surrounding particles, thus causing a change in energy and direction of motion For this situation to exist in plasma requires the kinetic energy of a particle in the gas to significantly exceed the mean interaction potential between itself and the surrounding particles [1] A plasma with these characteristics is termed an ideal plasma

The Coulombic potential between any two charged particles is expressed as e^2/R_I, where e is the electron charge and R_I is the distance between the particles Hence, the mean interaction distance between particles is proportional to the reciprocal of the electron density, N_e, $R_I \sim N_e^{-1/3}$ Since the plasma thermal energy is of the order of the plasma temperature, T, the condition for an ideal plasma may be written as [1]

$$\gamma = \frac{N_e e^6}{(4\pi\epsilon_0 k_B T)^3} \ll 1 \tag{1 1}$$

where γ is called the plasma parameter and ϵ_0 is the permittivity of free space Figure 1 1 shows the variation of γ for different temperatures over a wide range of electron densities, N_e

If a gas, containing no charged particles, is exposed to an electric field, the field is uniform across the gas If the gas contains charged particles, then the

2
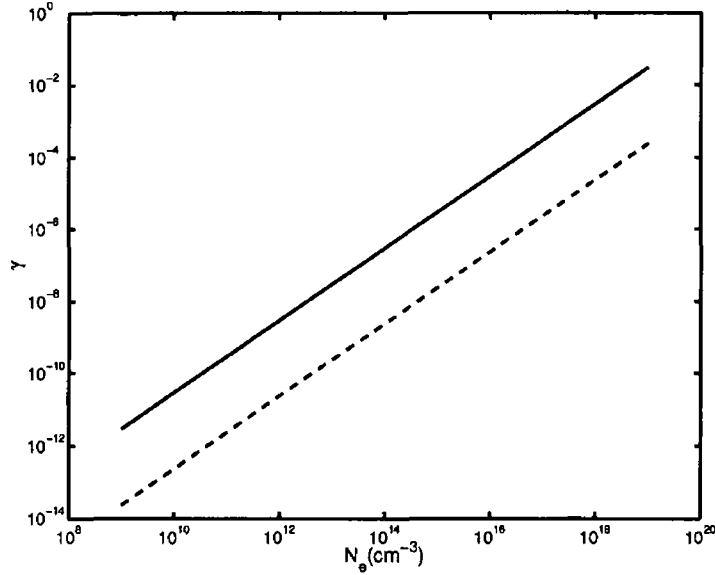
Figure 1 1   Plasma parameter as a function of N_e for $T = 1$ eV (–), $T = 3$ eV ( ) and $T = 5$ eV (– –)

electric field is shielded surrounding one ion over a distance known as the Debye Length The Debye length, R_D, may be written as [2]

$$R_D = \left(\frac{kT\epsilon_0}{2N_e e^2} \right)^{1/2}$$ (1 2)

The definition of the Debye length leads directly to the second criteria for a plasma to exist A plasma must be quasineutral up to its boundaries and shield an external electric field up to the plasma boundary Therefore, to maintain plasma conditions, the Debye length must be at least an order of magnitude smaller than the plasma length, L, so that [1]

$$10R_D < L$$ (1 3)

Figure 1 2 shows the Debye length for different plasma temperatures as a function of electron density over a wide range of densities In the following section, the creation of plasma via laser-material interaction is described

3
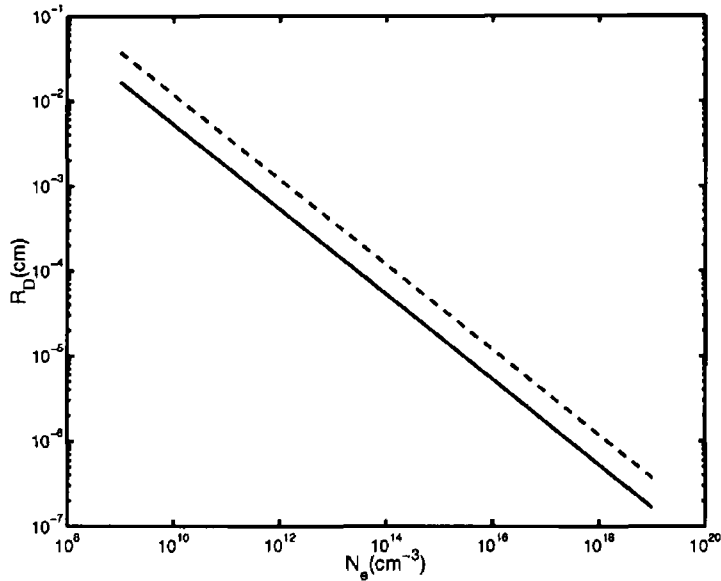
Figure 1 2 Debye length, R_D, as a function of N_e for $T = 1$ eV (–), $T = 3$ eV ( ) and $T = 5$ eV (– –)

1.3 Plasma Initiation

When laser light from a Q-switched laser is focussed onto a planar target, some of the light is reflected and the rest is absorbed by the material constituting the target The electrons in the conduction band are heated and their energy is then redistributed to other electrons and phonons via collisions, with relaxation times of the order of 10^{-12}–10^{-13} s^{-1} [3] Hence, an equilibrium at high temperature is obtained, since the laser pulse duration is much longer than this relaxation time

As well as the pulse length, the power flux density of the laser can play a major role in the plasma creation There are three main laser irradiance regimes, low ($I < 10^6$ Wcm^{-2}), medium (10^6 Wcm$^{-2} < I < 10^{10}$ Wcm^{-2}) and high ($I > 10^{10}$ Wcm^{-2}) [4] In the low irradiance regime, the main processes are normal heating, melting and vaporization This low irradiance regime is used in medicine

4

and data storage

If the irradiance is increased to $I > 10^{12}$ Wcm^{-2}, the plasma frequency will increase with the increased electron density [5] causing more of the light radiation to become shielded from the target and employed for the further heating of the ablated material Simultaneously, there are large pressure gradients in existance in the plasma so that the plasma expands, causing a reduction in electron density and, hence, plasma frequency so that the laser radiation will again penetrate through to the target surface This cycle is repeated until laser pulse termination

In the intermediate irradiance regime, 10^6 Wcm$^{-2} < I < 10^{10}$ Wcm^{-2}, plasma effects begin to play a role in the physics of the evaporated material However, the laser radiation penetrates through to the target surface for the duration of the laser pulse This regime is used where the maximum mass of ablated material is desirable and is therefore used in applications such as pulsed laser deposition (PLD) Plasma etching is also undertaken in this intermediate irradiance regime

This initial heat absorption takes place over a very thin surface layer known as the skin depth or absorption length, $\alpha(\lambda)^{-1}$, where α is the absorption coefficient and λ is the wavelength If the laser light absorption takes place over a significantly shorter time scale than the ablated material expansion, the process may be described in two distinct parts, the interaction of the beam with the target and initial plume formation followed by the plume expansion into vacuum/background gas In the case of plasma creation using femto- or picosecond lasers, thermal conduction may be neglected since there is insufficient time for the diffusion of heat and further melting and evaporation to take place so that the laser absorption depth is comparable to, or greater than, the heat penetration depth For nanosecond laser pulses, the heat penetration depth, L_{th}, is usually much larger than

the laser absorption length, with L_{th} given by [6]

$$L_{th} \approx \left(\frac{2k\tau_p}{\rho c}\right)^{\frac{1}{2}}$$

(1 4)

where k, τ_p, ρ and c are the thermal conductivity, laser pulse duration, mass density and specific heat, respectively Evaporation occurs when the energy absorbed by the target material is greater than the enthalpy of vaporization In most practical cases of laser-material interaction, the transverse dimensions of the laser beam are large in comparison to the heat penetration depth and the heat flow into the target is treated as a one dimensional process, as described below

For nano-second lasers, there is enough time for the energy to diffuse into the target material so that the ablated depth can be written as,

$$Z_a \approx \frac{A(F_{th} - F_L)}{\rho L_\nu}$$

(1 5)

where A is the surface absorbance of the target material, F_L is the fluence and the fluence threshold, F_{th}, is the energy necessary to vaporize a surface layer of the order of L_{th}, at initial temperature T_0 and melting temperature T_m, and is given by,

$$F_{th} \approx \frac{\rho c (T_m - T_0) L_{th}}{A}$$

(1 6)

with the surface absorbance, $A = 1\ 0 - R$, of the target and, hence, the reflectance, R, dependent on the refractive index, n, of the target material and the absorption coefficient, κ, so that [7]

$$R = \frac{(n-1)^2 + \kappa^2}{(n+1)^2 + \kappa^2}$$

(1 7)

For example, a lithium target ($n = 0\ 302, \kappa = 0\ 906$ [5]) irradiatied with a 248 nm KrF excimer laser has an absorbance of 0 48

6

This work is concerned with laser ablation plasmas in the regime applicable to the intermediate irradiance regime for nano-second pulses. In the following sections, plasma formation and expansion will be considered in the regime applicable to the PLD process.

1.4 Laser Plasma Expansion

When a Q-switched laser is focussed onto a solid metal target, a hot, dense cloud of atoms, ions and electrons is formed, which then expands freely into vacuum. To obtain a complete description of this process, a model should describe the target evaporation and plume expansion. However, due to the complexity associated with the development of a complete model, most models published in the literature only describe certain aspects of the process.

Some models describe the laser plume expansion beginning at the termination of the laser pulse, assuming an initial plume contained within a reservoir at time $t = 0$, which is then allowed to expand freely. Early spherical expansion models of this type were used to descibe the irradiation of pellets and their subsequent expansion [8, 9]. These models were then modified to cylindrical two-dimensional models to descibe the expansion of laser ablated material from planar targets, where the dimensions of the laser spot were circular and evolve at a different rate than along the target normal dimension. This two dimensional model was to take into account conditions where the laser spot radius is significantly larger than the initial target normal dimension. Since the largest acceleration is in the direction of smallest dimension due to the larger pressure gradients [10], the expansion velocity along the target normal will be significantly larger than its perpendicular components. Therefore, the plume shape will evolve and change from an initial rounded cap to an oblong ellipsoidal plume. In the following sections, the general

7

equations used to describe hydrodynamic expansion are introduced and a model used to solve this system of equations is outlined

1.4.1 Hydrodynamic expansion

The are three main characteristic ideas used to describe hydrodynamic expansion continuity, momentum conservation and energy conservation In continuity, the total number of particles in the expanding medium remains constant The equation of continuity is expressed

$$\frac{D\rho}{Dt} + \rho \nabla \bullet v = 0 \qquad (1\ 8)$$

The equation to express the conservation of momentum is written

$$\rho \frac{Dv}{Dt} + \nabla p = 0 \qquad (1\ 9)$$

The equation of conservation of energy is written

$$\frac{DE}{Dt} + p \frac{DV}{DT} - Q = 0 \qquad (1\ 10)$$

Here, ρ, v, p, E, V and Q is the mass density, velocity, pressure, energy, volume and external power source per unit mass of the material The stream derivative, $\frac{D}{Dt}$, describes the change in any parameter with respect to time as it follows a moving fluid particle It may be related to the partial derivative at a point in space and time by

$$\frac{D}{Dt} = \frac{\partial}{\partial t} + v \bullet \nabla \qquad (1\ 11)$$

A particular type of solution to this set of equations is outlined in the following section

8

1.4.2 Self-Similar expansion model

The mathematical simplicity of the self-similar solution to the general hydrodynamic equations, 1 8, 1 9 and 1 10, has enabled its wide use in gas dynamics [11–13] A self-similar flow occurs when the co-ordinates of a fixed fluid element, x_i, remain in fixed proportion to the characteristic dimension, X_i, independent of time [14]

$$\frac{x_i}{X_i} = \zeta_i \qquad (1\ 12)$$

The main characteristic of the self-similar model to describe plasma expansions is the use of a linear velocity profile

$$v_i = \left.\frac{\delta x_i}{\delta t}\right|_{\zeta_i} = \zeta_i \frac{dX_i}{dt} \qquad (1\ 13)$$

The linear velocity dependence in equation 1 13 is a condition for the use of the self-similar model since, if equation 1 13 is valid then equation 1 12 follows The self-similar solution is derived from the original hydrodynamic equations to describe the plasma evolution, allowing the computation of the velocity, density and pressure as a function of space and time

The initial conditions are usually defined, when using the self-similar model, so that a specified state variable takes a uniform distribution, for example, temperature (isothermal), density (isostatic) or entropy (isentropic) A constant pressure (isobaric) solution does not exist [14]

An adiabatic flow without external heat sources is such that the entropy is spatially variable in the plume but constant in time [14] If the gas is ideal, the spatial pressure and density distributions must satisfy the equation of state

$$p = N k_B T \qquad (1\ 14)$$

where p is the pressure, N is the number density of particles and T is the temperature

The general equation to describe self-similar expansion may be written

$$X\frac{\partial^2 X}{\partial t^2} = Y\frac{\partial^2 Y}{\partial t^2} = Z\frac{\partial^2 Z}{\partial t^2} = \beta\left(\frac{X_0 Y_0 Z_0}{XYZ}\right)^{\gamma-1} \tag{1 15}$$

where X_0, Y_0 and Z_0 are initial values of X, Y and Z, which are the plume dimensions at time t

In the case of the isentropic model β is given by

$$\beta = (5\gamma - 3)\frac{E}{M} \tag{1 16}$$

where the initial energy, E, and mass, M, are integrals over the plume volume, given by

$$E = \frac{1}{\gamma - 1}\int_V P(x, y, z, 0)dV \tag{1 17}$$

and

$$M = \int_V \rho(x, y, z, t)dV \tag{1 18}$$

In the isentropic model, the pressure and number density profiles have sharp external edges resulting from ellipsoidal profiles which may be written [15]

$$P(x, y, z, t) = \frac{E}{I_2(\gamma)XYZ}\left[\frac{X_0 Y_0 Z_0}{XYZ}\right]^{\gamma-1}\left[1 - \frac{x^2}{X^2} - \frac{y^2}{Y^2} - \frac{z^2}{Z^2}\right]^{\gamma/(\gamma-1)} \tag{1 19}$$

$$N(x, y, z, t) = \frac{N_T}{I_1(\gamma)XYZ}\left[1 - \frac{x^2}{X^2} - \frac{y^2}{Y^2} - \frac{z^2}{Z^2}\right]^{\gamma/(\gamma-1)} \tag{1 20}$$

where N_T is the total number of particles in the plume, and $I_1(\gamma)$ and $I_2(\gamma)$ are functions of the ratio of specific heats γ From their definition it follows that

$$\frac{I_1}{I_2} = (5\gamma - 3)\frac{\gamma - 1}{2\gamma} \tag{1 21}$$

The functions $I_1(\gamma)$ and $I_2(\gamma)$ are displayed in figure 1 3 From the ideal gas equation 1 14 and equation 1 21, it is possible to write the temperature profile as

$$k_B T = E\frac{(5\gamma - 3)(\gamma - 1)}{2\gamma}\left[\frac{X_0 Y_0 Z_0}{XYZ}\right]^{1/(\gamma-1)}\left[1 - \frac{x^2}{X^2} - \frac{y^2}{Y^2} - \frac{z^2}{Z^2}\right] \tag{1 22}$$

10
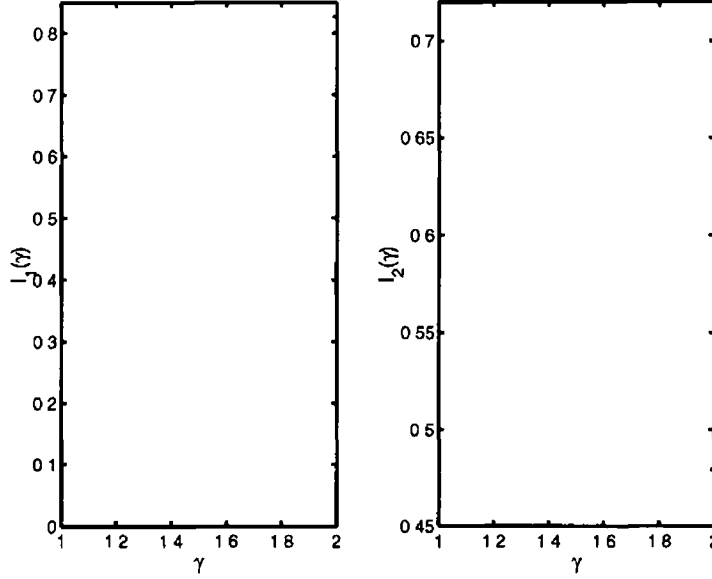
Figure 1 3 Graph of functions $I_1(\gamma)$ and $I_2(\gamma)$

In contrast to the isentropic solution, the isothermal solution implies a spatially constant temperature, which is variable in time In the solution for this type of self-similar model, β in equation 1 15 becomes

$$\beta = (1 - \gamma)\frac{E}{M} \qquad (1\ 23)$$

In this case the pressure and density profiles are represented by Gaussian profiles [16] These may be expressed [17]

$$P(x, y, z, t) = \frac{N_T k_B T_0}{2^{1/2}\pi^{3/2}(\gamma)XYZ}exp\left[-\frac{x^2}{2X^2} - \frac{y^2}{2Y^2} - \frac{z^2}{2Z^2}\right] \qquad (1\ 24)$$

$$N(x, y, z, t) = \frac{N_T}{2^{1/2}\pi^{3/2}(\gamma)XYZ}exp\left[-\frac{x^2}{2X^2} - \frac{y^2}{2Y^2} - \frac{z^2}{2Z^2}\right] \qquad (1\ 25)$$

Here N_T again corresponds to the total number of particles and is replaced by $N_T t/\tau$ during the laser pulse to take into account the injection of particles into the plasma The next section discusses the implications of the resulting density profiles from self-similar expansions

11

1.4.3 Density profiles and velocity gradients in self-similar expansions

When a surface is ablated, many particles are vaporised to form a dense mixture of atoms, ions and electrons very close to the target surface In gases, the mean free path of particles is often much shorter than the length scale and the time between collisions much shorter than the relaxation time In these conditions, the system is averaged on a finer scale compared to the macroscopic quantities so that kinetic theory may be used to establish quantities, such as pressure and temperature, under the assumption of a Maxwellian velocity distribution This allows the approximation of a gas as a fluid and the use of continuum models to describe the gas dynamics If the mean free path becomes comparable to the length scale or the relaxation time becomes comparable to the time separating collisions, kinetic theory is essential and molecular models must be employed

The Knudsen number, K_n, represents the degree of rarefaction of a gas and is given by [18],

$$K_n = \frac{D_{mfp}}{L} \qquad (1\ 26)$$

where D_{mfp} is the mean free path, average distance between collisions, and L is the scale length of macroscopic gradients, for example

$$L = \frac{\rho}{\left(\frac{\delta \rho}{\delta x}\right)} \qquad (1\ 27)$$

where ρ is the density As $K_n \rightarrow 0$, the viscous Navier-Stokes equations may be reduced to the inviscid Euler equations and the flow considered as isentropic A significant error in the Navier-Stokes result becomes apparent for $K_n > 0\ 1$ and the continuum model must be replaced by the molecular model for $K_n > 0\ 2$ [18] Figure 1 4 indicates the applicability of different types of model depending on the value of the Knudsen number

Discrete Particle or Molecular Model	Boltzmann Equation			Collisionless Boltzmann Equation
Continuum Model	Euler Eqns	Navier-Stokes Equation	Conservation Equations Do Not Form A Closed Set	

    → 0   0.01   0 1   1   10   100   → ∞

Inviscid Limit   Local Knudsen Number   Free-Molecule Limit
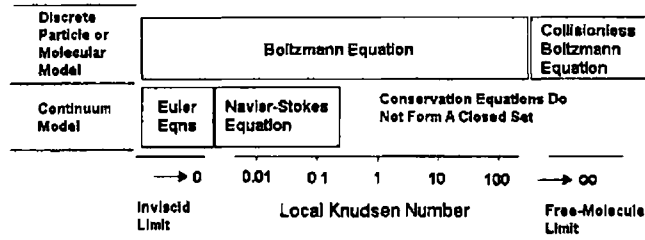
Figure 1 4   The dependence of Knudsen number on mathematical models

During the initial expansion, there is a region in the front portion where the Knudsen number is sufficiently small so that free expansion may be assumed and a continuum model may be used If the density remains low enough, the evaporated cloud will disperse in a collisionless fashion In this case, the velocity distribution function takes a "half-range" Maxwellian form, since the velocities normal to the surface have only positive values, and the exponential part of the velocity component normal to the surface, v_x, has the form

$$exp\left(-\frac{mv_x^2}{2k_BT}\right), v_x \geq 0 \tag{1 28}$$

However, as more particles are ejected from the target surface, there will be more collisions with the increased density For as few as $3 - 5$ collisions per particle [19], a Knudsen layer will form This region is where evaporated particles, initially having positive velocities with respect to the target develop negative velocities This Knudsen layer induces a shock wave, which travels into the target surface

Due to the conservation of momentum, the particles develop a positive centre-of-mass velocity [20] and the velocity distribution evolves from the "half-range", equation 1 28, to a "full-range" Maxwellian distribution function in a centre-of-mass coordinate system [21] with the exponential portion given by,

$$exp\left(-\frac{(mv_x - u_K)^2}{2k_BT}\right), -\infty < v_x < +\infty \tag{1 29}$$

13

where u_K is the Knudsen layer velocity [22] A fluence of $> 200 \; mJcm^{-2}$ is sufficient to initiate a Knudsen layer [23]

The problem of the centre of mass motion has been tackled by Guan [24], who included this motion using the pressure exerted by the expanding plume onto the target surface in the isothermal self-similar solution The pressure at any point on the target surface is given by $N(X_{PMD}, y, z, t)k_B T(t)$ (isothermal expansion) or $N(X_{PMD}, y, z, t)k_B T(x, y, z, t)$ (isentropic expansion), where X_{PMD} is the distance along the target normal between the target, $x, y, z = 0$, and position of maximum plume density (PMD) position

Assuming that the plasma behaves as a bulk gas, the equation of motion for the target velocity for the isothermal case is given by [24]

$$M_t \frac{dV_t}{dt} = \int_{-\infty}^{+\infty} \int_{-\infty}^{+\infty} P(X_{PMD}, y, z, t) dy dz \qquad (1\;30)$$

where M_t and V_t are the velocity and mass of the target, respectively Enforcing the conservation of momentum, M_t and V_t can be replaced by the total mass of the plasma, mN_T, m is the mass of one particle, and velocity of the PMD position, V_{PMD} so that the equation of motion becomes

$$N_T m \frac{dV_{PMD}}{dt} = \int_{-\infty}^{+\infty} \int_{-\infty}^{+\infty} P(X_{PMD}, y, z, t) dy dz \qquad (1\;31)$$

and, hence, the PMD position may be obtained from

$$\frac{dX_{PMD}}{dt} = V_{PMD} \qquad (1\;32)$$

The density profiles in the self-similar model are axially symmetric in the target normal plane The plume will always have the widest tranverse components in the dimensions parallel to the target surface Figure 1 5 shows the plume geometry with and without the inclusion of the centre-of-mass motion with respect to the target

14
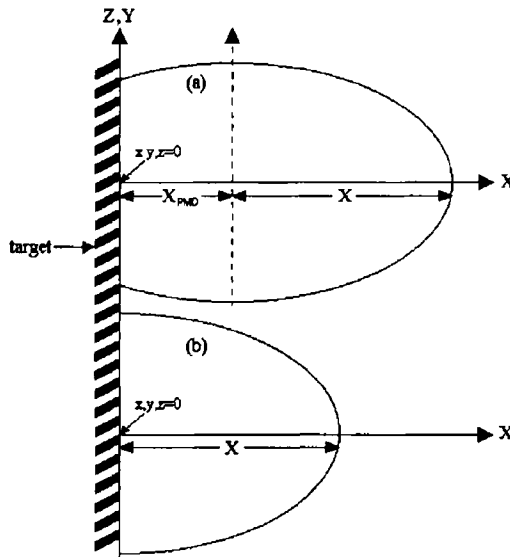
Figure 1 5 Indication of the plume coordinate system with PMD position evolution included (a) and excluded (b)

1.5   Equilibrium Models for Description of Ion Stage Populations

1.5.1   General Principles

Ionization and recombination processes dictate the relative populations of the various charge states in plasma   An ionizing plasma occurs when the total rate of ionization exceeds the rate of recombination so that ions are stripped of electrons causing their continual increase in charge   If the rate of recombination predominates over the rate of ionization, the plasma is a recombining plasma   A steady-state plasma is achieved when the rate of ionization and the rate of recombination are equal   Therefore, the ionization state is constant in a steady-state plasma

The kinetics of energy levels in a particular ionic stage may be considered in much the same way. Their relative populations are evaluated through comparison between excitation and deexcitation processes. Steady-state populations are achieved within a particular ionic stage when the excitation processes are balanced by the deexcitation processes.

Complete thermodynamic equilibrium occurs when the atoms and ions, electrons and photons are in equilibrium at the same temperature. This implies the existance of the principle of detailed balance, which states that the rate of every process is equal to the rate of its inverse. In such a case, the electron and ion velocities satisfy a Maxwell Boltzmann distribution function, the excited states have a Boltzmann distribution and the photons have a Planck distribution curve. For complete thermodynamic equilibrium to exist, the plasma must be optically thick at all frequencies. However, this situation is rarely applicable and another approximation method to describe the populations of ion and excited state densities must be applied. Many atomic processes contribute to the population/depopulation of excited levels and these include, collisional ionization, three body recombination, collisional excitation/deexcitation, radiative recombination, dielectronic recombination, photoexcitation, photoionization etc. The rate coefficient corresponding to a particular process is defined as the process cross-section times the velocity, averaged over the velocity distribution, $< \sigma v >$. In figure 1 6, the most frequent atomic processes are shown.

Simplifications arise in the overall calculations for the population of the atomic levels in specific density and temperature regimes. In the corresponding conditions, particular populating/depopulating processes dominate. In the following sections, the corresponding models and their validity criteria are outlined.

16
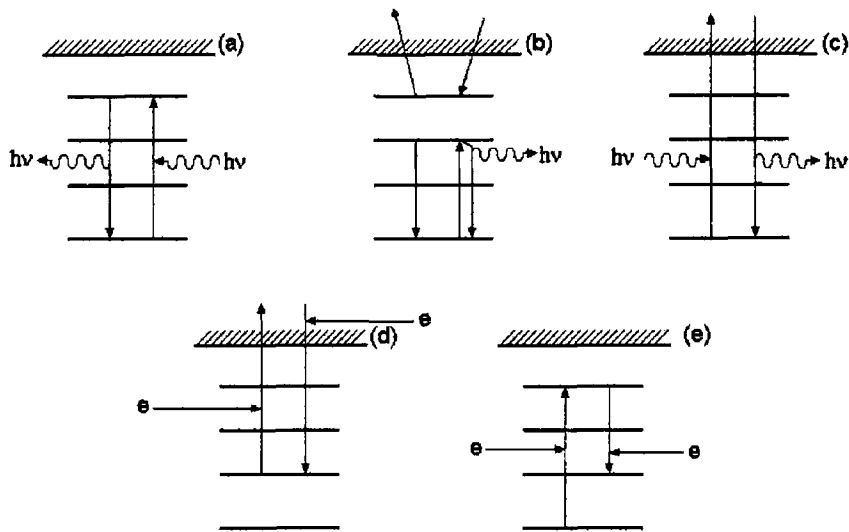
Figure 1 6 Schematic diagrams of the most frequent processes in hot plasmas (a) Spontaneous decay (l) and resonant photoabsorption (r), (b) Autoionization (l) and dielectronic recombination (r) (c) Photoionization (l) and radiative recombination (r) (d) Electron impact ionization (l) and three-body recombination (r) and (e) Electron impact excitation (l) and deexcitation (r), where l and r correspond to left and right-hand parts of the diagram, respectively

1.5.2 Collisional Radiative (CR) Equilibrium

The CR model must be employed in the region of medium density plasma conditions where neither high density, Local Thermodynamic Equilibrium (LTE), or low density, Coronal Equilibrium (CE), approximations are appropriate to calculate the plasma ionization balance

Converse to the approximate models, such as LTE and CE, for the calculation of excited states, the density of a given species is calculated by solving the complete set of rate equations that take into account all processes that increases or decreases an atomic level population There are seven processes that can influence

17

the population of an atomic level in this regime electron impact ionization, three body-recombination, two-body (radiative+dielectronic) recombination, electron impact excitation and deexcitation and spontaneous emission The rate equation for an ith atomic level is given by

$$\frac{\partial N_i}{\partial t} = \sum_{j<i} N_e N_j C_{ji} + \sum_{j>i} N_e N_j D_{ji} + \sum_{j>i} N_j A_{ji} \kappa_{ji}$$

$$+ N_e n_1 (\alpha_{3B,k+1,i} \kappa_{ci} + N_e \alpha_{2B,k+1,i}) - N_i \left(\sum_{j>i} N_e C_{ij} \right.$$

$$\left. + \sum_{j<i} N_e D_{ij} + \sum_{j<i} A_{ij} \kappa_{ij} + N_e S_{k,i} \right) \qquad (1\ 33)$$

where N_e is the electron density, C_{ij} and D_{ij} are the electron impact excitation and deexcitation rate coefficients for transitions from level i to j $S_{k,i}$, $\alpha_{3B,k+1,i}$ and $\alpha_{2B,k+1,i}$ are the electron impact ionization, three-body recombination and two-body recombination rate coefficients of level i in ionization stage k, respectively κ_{ij} and κ_{ci} are the radiation escape factors for radiation emitted in bound-bound and free-free transitions, respectively

The radiation escape factors, κ vary from 1, when the radiation is completely emitted and the plasma is optically thin for the particular transition to 0, when the radiation is completely absorbed and the plasma is optically thick for the transition in question The escape factor may be defined in terms of photon escape or photon capture In terms of photon escape, the escape factor may be defined, generally, as [25]

$$\kappa_{esc} = \frac{E}{MA} \qquad (1\ 34)$$

where κ_{esc} denotes the mean probability that a photon emitted anywhere in the source travels directly to the surface and escapes, E is the rate of emergence of the photons from the source, M is the total number of emitting atoms in the source and A is the spontaneous transition probability The escape factor may also be defined

18

in terms of photon capture The net rate of radiative deexcitations summed over the whole source may be expressed as [25]

$$R = MA - R_{pe} \qquad (1\ 35)$$

where R_{pe} is the rate of photoexcitations summed over the whole source The escape factor may then be written [25]

$$\kappa_{cap} = \frac{R}{MA} \qquad (1\ 36)$$

From the conservation of photons, R is equal to E so that the escape factor defined in terms of photon escape is equal to that defined for photon capture, $\kappa_{esc} = \kappa_{cap}$

In the steady state case, $\partial N_i/\partial t = 0$, equation 1 33 reduces to

$$N_i \left(\sum_{j<i} A_{ij} + N_e \sum_{j<i} D_{ij} \right) = \sum_{j<i} N_e N_j C_{ji} + \delta \qquad (1\ 37)$$

where δ is given by

$$\delta = \sum_{j>i} N_j A_{ji} \kappa_{ji} + N_e \left(\sum_{j>i} N_j D_{ji} + N_{k+1}(\alpha_{2B,k+1,i} \kappa_{c,i} + N_e \alpha_{3B,k+1,i}) \right)$$
$$- N_e N_i \left(\sum_{j>i} C_{ij} + S_{k,i} \right)(1\ 38)$$

In many plasmas with medium and high electron densities, δ may be neglected and equation 1 37 reduced to give [26]

$$N_i = \frac{N_e \sum_{j<i} N_j C_{ji}}{\sum_{j<i} A_{ij} \kappa_{ij} + N_e \sum_{j<i} D_{ij}} \qquad (1\ 39)$$

so that only the rates for collisional excitation, deexcitation and spontaneous emission are required This approximation is valid when

$$N_e \sum_{j>i} N_j C_{ji} >> \delta \qquad (1\ 40)$$

This criterion may be simplified so that all of the rate coefficient calculations of equation 1 38 are not required If the electron density limit is approached from

19

low densities and, since the radiative terms prevail in the low density case, the condition for the neglection of δ may be written [27]

$$N_i \sum_{j<i} A_{ij} >> \sum_{j>i} N_j A_{ji} \tag{1 41}$$

Using these considerations, the population densities can be written in Boltzmann-like form

$$\frac{N_j}{N_i} = \frac{B_j}{B_i} \frac{g_j}{g_i} exp\left(-\frac{E_j - E_i}{T_e}\right) \tag{1 42}$$

where E_i and E_j are the energies of the levels with repect to the ground state and g_i and g_j are the statistical weights of the energy levels The coefficients B_i and B_j measure the deviation of the energy levels from thermodynamic equilibrium and are given by

$$B_i = \frac{\sum_{j<i} B_j \tau_{ij}}{1 + \sum_{j<i} \tau_{ij}} \tag{1 43}$$

where τ is given by

$$\tau_{ij} = \frac{N_e R_{ij}}{\sum_{j<i} A_{ij} \kappa_{ij}} \tag{1 44}$$

Using the CR model, the rate equation describing the population/depopulation of a particluar ionic state, $k + 1$, may be written

$$\frac{dN_{k+1}}{dt} = N_e N_k S_k - N_e N_{k+1}[S_{k+1} + \alpha_{2B,k+1} + N_e \alpha_{3B,k+1}]$$
$$+ N_e N_{k+2}[\alpha_{2B,k+2} + N_e \alpha_{3B,k+2}] \tag{1 45}$$

where S_k is the corresponding average electron-impact ionization, $\alpha_{2B,k+1}$ is the total radiative recombination rate coefficeint and $\alpha_{3B,k+1}$ is the average three-body recombination rate coefficient

For a steady-state plasma, $dN_k/dt = 0$, due to end conditions on the ionic chain [28] equation 1 45 reduces to

$$\frac{N_{k+1}}{N_k} = \frac{S_k}{\alpha_{2B,k+1} + \alpha_{3B,k+1}} \tag{1 46}$$

20

It is clear that when the electron density is high, and three-body recombination becomes the dominant process, LTE is approached At the other extreme, when the plasma is recombining and two-body processes become dominant, CE is approached Hence, LTE and CE are approximations of CR in the high and low density extremes, respectively

In implementing simplified equilibrium models, the calculation of the partition function is often important and a method for truncating the energy level distribution may be required This may be achieved with the consideration of continuum lowering In the following section, continuum lowering is introduced and the partition function calculation is outlined

1.5.3 The Partition Function and Continuum Lowering

The binding energy of an electron in an isolated atom/ion is the energy necessary to eject that electron from the atom/ion into the continuum However, when this atom/ion is exposed to an external field the binding energy is reduced due to the lowering of the ionization potential, the energy to ionize an electron in the ground state of the atom/ion, $E_i(\infty)$

The amount by which this ionization potential is lowered, $\Delta E(\infty)$, may be written [29]

$$\Delta E(\infty) = \frac{ke^2}{4\pi\epsilon_0 R_D} \qquad (1\ 47)$$

where k is the number of free electrons in the ion sphere, e is the charge of the electron and R_D is the Debye Length

The canonical distribution provides the formula for the distribution of a macroscopical system in a large closed system that is in equilibrium The probability, P, of this subsystem in a state i with energy E is written [30]

$$P \propto g_i e^{\frac{-E_i}{T}} \qquad (1\ 48)$$

21

where g_i is the statistical weight of this state and T is the temperature in energy units (eV) The normalization condition of the probability distribution function requires

$$P = \frac{g_i e^{-\frac{E_i}{T}}}{Z(T)}$$

(1 49)

where $Z(T)$ is the partition function and is given by

$$Z(T) = \sum_i g_i e^{\frac{E_i}{T}}$$

(1 50)

To calculate the partition function, the sum should be truncated to include only those levels lying below the lowered ionization potential $E(\infty)$ This ensures that levels are not repeatedly counted, as bound and free states At low temperatures, the exponential terms corresponding to the excited levels are negligible and, hence, the main contribution to the total partition function will be from the ground state alone If the temperature is increased, the excited levels may provide a significant contribution to $Z_k(T)$ and the calculation must be performed including all levels up to $E(\infty)$ A hydrogenic approximation may be used to calculate the maximum principal quantum number, p_{max}, for inclusion in the total sum for $Z_k(T)$ [29] This may be written

$$p_{max} \leq \left(\frac{k^2 E_H}{\Delta E(\infty)} \right)^{1/2}$$

(1 51)

where E_H is the ionization energy of hydrogen The contribution from the higher lying levels excluded from the sum may be estimated using the equation [29]

$$P_{k-1} \approx \sum_{p=1}^{p'} g_{k-1}(p) exp\left(-\frac{E_{k-1}(p)}{T_e} \right) + \frac{2}{3}(2S_1 + 1)(2L_1 + 1)$$
$$\times \left(\frac{k^2 E_H}{\Delta E_{k-1}} \right)^{3/2} exp\left(\frac{-E_{k-1}(\infty) - \Delta E_{k-1}(\infty)}{T_e} \right)$$

(1 52)

where p' is the highest principal quantum number where all levels of the configuration with angular momentum of the outer electron of $l = p - 1'$ are included in

22

the energy level tables, and S_1 and L_1 are the spin and orbital angular momentum quantum numbers of the ground state of the next highest ionization stage
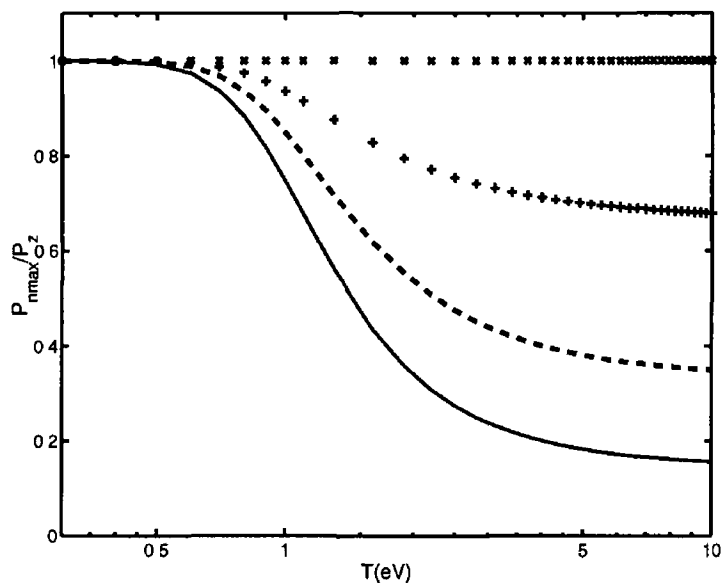
Figure 1 7 Partition function calculation for Li^0 at various maximum principal quantum numbers, $P_{n_{max}}$ normalised to the total partition function P_k, using all available energy level data $n_{max} = 2(-)$, $n_{max} = 3(- -)$, $n_{max} = 4(*)$, $n_{max=5}(\times)$

Figure 1 7 displays the partition function for Li^0 for various maximum principal quantum numbers, $P_{n_{max}}$, normalised to the total P_k calculated using all levels available from the NIST database, [31] It is clear that at temperatures below $\approx 0\ 5$ eV that the main contribution is from the ground state and, for higher temperatures, the excited states begin to significantly contribute to P_k However, for total principle quantum number, $n = 5$, all levels above $n = 5$ remain insignificant to the total calculation

23

1.5.4 Local Thermodynamic Equilibrium

The local thermodynamic equilibrium (LTE) approximation is generally used for high density plasmas and applies where the plasma characteristic dimensions are much smaller than the mean free path of the photons emitted from the plasma, but much longer than the mean free path of the ions or electrons In LTE plasmas, photons emitted in one part of the plasma may be reabsorbed elsewhere inside the plasma, but at a position where the temperature and density differ from that where the photon was emitted Therefore, LTE occurs in a plasma where the electrons and ions are in equilibrium amongst themselves while the photons are not

In LTE, the electrons obey the Maxwellian velocity distribution function [32],

$$f_v(v)dv = N_e \left(\frac{m_e}{2\pi T_e} \right)^{\frac{3}{2}} exp\left(-\frac{m_e v^2}{2T_e} \right) 4\pi v^2 dv \qquad (1\ 53)$$

where $f_v(v)dv$ is the density of electrons with velocities between v and $v + dv$, m_e is the electron mass and T_e is the electron temperature in eV The fractional ion state distributions are given by the Saha equation [30],

$$\frac{N_k N_e}{N_{k-1}} = 2 \left(\frac{mc^2 T_e}{2\pi\,(\hbar c)^2} \right)^{\frac{3}{2}} \frac{Z_k(T_e)}{Z_{k-1}(T_e)} exp\left(-\frac{E_{k-1} - \Delta E_{k-1}}{T_e} \right) \qquad (1\ 54)$$

where N is the population density and $E_{k-1} - \Delta E_{k-1}$ is the ionization energy of charge state k, with $k = 1$ for single ionization, corrected for the local continuum lowering ΔE_{k-1} In LTE, the level populations are given by a Boltzmann distribution [30]

$$\frac{N_i}{N_j} = \frac{g_i}{g_j} exp\left(-\frac{E_{ij}}{T_e} \right) \qquad (1\ 55)$$

where i and j are the lower and upper levels, respectively, g is the statistical weight and E_{ij} is the difference in energy between the two energy levels

24

Validity of LTE

LTE generally applies to high density plasmas that are in steady state. The levels of the neutral/ ion, level p and above, are in partial LTE if the Saha-Boltzmann relation, equation 1 54, applies to level p and all higher lying energy levels [33] For level p to satisfy equation 1 55, the collisional depopulation must be greater, by at least an order of magnitude, than the radiative depopulation rate, so that

$$\left[\sum_{q(>p)} C(p,q) + \sum_{q(<p)} D(p,q) + S(p) \right] N_e \geq 10 \sum_{q(<p)} A(p,q) \qquad (1\ 56)$$

Here, $A(p,q)$ is the radiative transition probability from level p to q, $C(p,q)$ is the collisional excitation rate coefficient for $q > p$, $D(p,q)$ is the collisional deexcitation rate coefficient for $q < p$, and $S(p)$ is the ionization rate coefficient For $p >> 1$ or for high temperatures, the dominant collisional processes are excitation and equation 1 56 may be reduced to [33],

$$N_e \geq 10 \frac{\sum_{q(<p)} A(p,q)}{\sum_{q(>p)} C(p,q) N_e} \qquad (1\ 57)$$

Complete LTE occurs when all of the collisional depopulating rates predominate over all the competing radiative transition rates so that the Boltzmann population distribution, equation 1 55, applies to all levels inclusive of the ground state, $p = 1$ The criterion for this realisation is given by [34],

$$D(2,1) N_e \geq 10 A(2,1) \qquad (1\ 58)$$

This condition is sufficient for the Saha-Boltzmann equation to apply and the achievement of ionization balance [33] H R Griem has derived a formula using hydrogenic approximations for the cross-sections for validity of complete LTE, which may be written as

$$N_e \geq 9 \times 10^{17} \left(\frac{E_2}{\chi} \right)^3 \left(\frac{T_e}{\chi} \right)^{1/2} [cm^{-3}] \qquad (1\ 59)$$

25

where χ is the ionization energy, $\approx 5\ 4eV$ for Li neutral, E_2 is the energy of the first excited level and T is the temperature in eV

However, equation 1 58 is insufficient to ensure complete LTE in any plasma It must also be ensured that the plasma is steady-state and locally homogeneous The plasma must be sufficiently homogeneous so that the mean free path of particles, λ_{mfp}, involved in the most frequent collisional process is at least an order of magnitude lower than the scale length for electron density and temperature in the plume [33] This may be written as

$$10\lambda_{mfp} < \frac{N_e}{|\nabla N_e|}, \frac{T}{|\nabla T|} \qquad (1\ 60)$$

where λ_{mfp} is given by

$$\lambda_{mfp} = \frac{v}{\tau} \qquad (1\ 61)$$

where v is the electron velocity and τ_p is the time between collisions and may be written

$$\tau = \frac{1}{N_e <\sigma v>} \qquad (1\ 62)$$

The angle parenthesis indicate averaging over the velocity distribution of electrons, see section 1 6

If the plasma parameters, N_e and T_e are evolving in time, then sufficient time independence must also be established to allow the computation of instantaneous populations The assumption of time independence is valid when the time, τ, between collisions for the most frequent atomic process in the plasma is at least an order of magnitude lower than the characteristic time in the plasma- the time required for the macroscopic variables, N_e and T to change appreciably This condition may be written [33]

$$10\tau < \frac{N_e}{\left|\frac{\delta N_e}{\delta t}\right|}, \frac{T}{\left|\frac{\delta T}{\delta t}\right|} \qquad (1\ 63)$$

26

For the remainder of this work, when referring to LTE validity, this will signify complete LTE validity This section considered a high density limit to the collisional radiative model and the next section considers the low density limit, namely, the coronal model

1.5.5 Coronal Equilibrium (CE)

For a low density optically thin plasma, such as the solar corona, the radiative decay processes predominate over collisional decay processes and photoexcitation processes are negligible In low ion/electron density plasmas, since the rate of upward transitions due to collisions is so low relative to the rate of spontaneous decay, atoms excited to an upper level are more likely to decay to their ground state before further excitation can take place Therefore, in CE, most of the ions are in their ground state

Since most of the atoms/ions in CE are in their ground state, only collisional excitation from the ground state requires consideration and the population density of level p, $N(p)$, is given by [29]

$$N(p) = \frac{N(1)N_e C(1,p)}{A(p)} \tag{1 64}$$

In CE, the dominant population/ depopulation processes are collisional ionization and the two body processes, radiative recombination, α_R, and dielectronic recombination, α_D The fractional ion state distributions are then given by [30]

$$\frac{N_k}{N_{k-1}} = \frac{S(k-1,k)}{\alpha_D(k,k-1) + \alpha_R(k,k-1)} \tag{1 65}$$

Since the collisional ionization and 2-body recombination rates have the same dependence, the population densities of the ionic states have no dependence on electron density, but only on the temperature

For radiative processes to prevail, the three-body recombination rate, α_{3B}, must have a neglibible effect on the ion population densities, at least an order

of magnitude lower, in comparison to the two body processes, α_{2B} Hence, the condition for CE to apply for the ion population calculation is given by

$$10N_e\alpha_{3B} \leq \alpha_{2B} \tag{1 66}$$

In the following section the important atomic processes in plasma will be outlined

1.6 Atomic Processes in Plasmas

To use a collisional radiative model to evaluate various atomic populations in plasmas requires information regarding the various processes that can populate/ depopulate atoms, ions and energy levels within the overall atom or ion

To evaluate the rates of a populating/ depopulating process, where no fitting formula or other simplified method is used, requires the cross-section for the process of interest The cross-section, σ, provides the probability of an ionic process and is defined as the effective area of the interacting process for a collision to occur If $n_{k,i}$ is the density of ions with charge k in the initial state, i, in a cylinder of thickness l, then the fraction of the area occupied by the ions, the number of collisions in a cylinder of cross-sectional area, σ, and length, l, according to an incoming particle is given by

$$n_{coll} = n_{k,i}\sigma l \tag{1 67}$$

If l is equivalent to the mean free path, λ_{mfp} then the number of collisions in a cylinder of length λ and cross-sectional area is 1 Also, a particle with velocity, v, traverses λ_{mfp} in a time λ_{mfp}/v, so that the average number of collisions per unit time is v/λ_{mfp} Hence, the relationship between the transition rate and the cross-section is written

$$\frac{v}{\lambda_{mfp}} = n_{k,i}v\sigma \tag{1 68}$$

However, this relationship corresponds to a stationary target approached by a particle with a single velocity In a real plasma there is a distribution of velocities, each group of particles with velocities between v and $v + dv$ generating collisions at a rate given by equation 1 68 In a plasma these particles, usually electrons, are assumed to have a Maxwell-Boltzmann distribution of velocities, so that the total rate of the reactions per unit volume for electrons of density n_e is

$$n_{coll} = n_{k,i} \int f_v v \sigma dv \qquad (1\ 69)$$

where $f_E(E)dE$ is written [30]

$$f_E(E)dE = \frac{2}{\sqrt{\pi}} n_e \left(\frac{E}{T_e}\right)^{1/2} exp\left(-\frac{E}{T_e}\right) \frac{dE}{T_e} \qquad (1\ 70)$$

Hence, to evaluate the rate coefficient of a process requires the cross-section of the process averaged over an appropriate velocity distribution In this section, the important rates that affect the population densities in a plasma are described

1.6.1 Electron Impact Ionization and Three Body Recombination

There are two main collisional processes that contribute to the population and depopulation of ions in plasma and are known as the electron impact ionization and three body recombination processes

Electron impact ionization occurs when an electron travelling in the plasma moves within close proximity to an ion such that a collision occurs and the colliding electron reduces in energy but remains in the continuum Meanwhile, a bound electron in the ion gains sufficient energy to escape from the ion and is ejected to the continuum increasing the charge of the ion

Three-body recombination is the inverse process, whereby, two electrons enter the volume of an ion simultaneously and one of the electrons is reduced in energy

29

and decays to a bound state of the ion The other electron accepts the extra energy and remains in the continuum so that one electron has recombined and the ion is reduced in charge This may be represented by

$$A_i^k + e \Longleftrightarrow A_j^{k+1} + e + e \qquad (1\ 71)$$
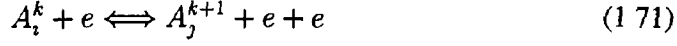
where A denotes an ion at energy level, i or j corresponding to the charge state k or $k+1$, respectively

The total number of electron impact ionization processes for an ion of charge state k per unit time per unit volume, n_s, may be written as

$$n_s = \sum_{i,j} P_i n_i n_e S(k, i \to k + 1, j) \qquad (1\ 72)$$

where $S(k, i \to k + 1, j)$ indicates the electron impact ionization rate coefficient for an ion initially in level i of charge state k, n_k is the number of particles of charge state k, P_i is the population probability of level i, and n_e is the electron density

The three-body recombination rate coefficient, α_{3B}, is higher in high density plasma since there are two electrons required per interaction The total number of three-body recombinations per unit time per unit volume, n_{3B}, is proportional to the square of n_e due to the requirement for two electrons and is written as

$$n_{3B} = \sum_{j,i} P_j n_j n_e^2 \alpha(k + 1, j \to k, i) \qquad (1\ 73)$$

where $\alpha(k + 1, i \to k, j)$ is the three-body recombination rate coefficient for an ion initially in level i of charge state $k + 1$ Assuming that the detailed balance principle holds the electron impact ionization and three-body recombination rate coefficients may be related using the formula [30]

$$\frac{S(k, i \to k + 1, j, T_e)}{\alpha(k + 1, i \to k, j), T_e} = 2 \left(\frac{mc^2 T_e}{2\pi(\hbar c)^2} \right)^{3/2} \frac{g(k + 1, j)}{g(k, i)}$$
$$\times exp\left(-\frac{E_{k+1,j} - E_{k,i}}{T_e} \right) \qquad (1\ 74)$$

30

where the first factor on the right hand side corresponds to the final state density of the free electron, the factor 2 accounts for its two possible spin states with the final factor, including the statistical weight ratio, is the final ionic state density

There have been many proposed methods for the electron impact ionization rate coefficient They consider the final state as the ground state of the ionized ion The Lotz formula remains a widely used formula for the calculation of this rate coefficient and is expressed

$$S(k, i \rightarrow k+1, j) = 3 \times 10^{-6} \left(\frac{cm^3}{eV^{3/2}s} \right) \eta_{k,nl} T^{-3/2} \frac{1}{y} E_1(y) \qquad (1\ 75)$$

where $E_1(y)$ is the exponential integral, $\eta_{k,nl}$ is the number of electrons in the ionizing shell and y is given by

$$y' = \frac{|E_{k,nl} - \chi_k|}{T_e} \qquad (1\ 76)$$

1.6.2   Electron Impact Excitation and Deexcitation

Electron impact excitation occurs when an ion interacts with an electron via a collision The ion gains energy causing an electron in the ionic ground state or an excited level to become excited to a higher bound energy level The energy gained by the ion is equivalent to the energy lost by the electron in the collision Electron impact deexcitation corresponds to the inverse process where the electron in the collision gains energy from the ion, whose energy lost is manifested through the drop of an electron in an ionic bound state to a lower or ground state In these processes, the charge of the ion remains unchanged and the process may be represented as,

$$A_j^k + e \Leftrightarrow A_i^k + e \qquad (1\ 77)$$

where i and j corresponds to the upper and lower levels, respectively The electron and deexcitation rate coefficients may be related through the detailed balance

31

principle, so that

$$\frac{C_{ji}}{D_{ij}} = \frac{g_{k,j}}{g_{k,i}} exp\left(-\frac{\Delta E}{T_e}\right)$$ (1 78)

where g_i and g_j are the statistical weights of the upper and lower levels, respectively, ΔE is the energy difference between the levels and T_e is the temperature in eV

1.6.3 Photoionization and Radiative Recombination

Photoionization is a radiative process where an electron in a bound state absorbs a photon of sufficient energy so that it is ejected into the continuum This process is important in plasma that contains a high enough radiation field to induce a significant rate of photoionization processes in comparison to the rate of electron impact ionization This occurs only in optically thick plasma where the mean free path of a photon is much less than the plume characteristic dimension increasing the probability of photon reabsorption in the plasma

The inverse process is radiative recombination, where an incident electron is captured into an ionic bound state and a photon is released with energy equal to the energy lost by the electron These processes may be represented by

$$A_i^k + e \Longleftrightarrow A_j^{k+1} + h\nu$$ (1 79)

The total radiative recombination rate coefficient for an ion is the sum of all of the recombination coefficients to the ground level and all of the excited levels This means that the cross-sections are required for all possible transitions In [35] and others at the time, due to a shortage of experimental data, the cross-sections along isoelectronic sequences were extrapolated Hydrogenic approximations were used for all excited levels To calculate the ground level recombination coefficient the photoionization cross-section was used with the Milne relation, which is a formula

relating the photoionization and radiative recombination rate coefficients via the detailed balance principle and may be written [30]

$$\frac{\sigma_\phi(k, \imath \rightarrow k + 1, \jmath)}{\sigma_{rr}(k + 1, \jmath \rightarrow k, \imath)} = \frac{2mc^2 E_e}{h\nu} \frac{g_{k+1}}{g_k} \tag{1 80}$$

where $k, \imath$ is the bound electron state, $k + 1, \jmath$ is the ionized state σ_ϕ and σ_{rr} are the cross-sections for photoionization and radiative recombination, respectively, and $E_e = h\nu - |E_{k,\imath}|$ is the energy of the ejected electron

1.6.4 Autoionization and Dielectronic Recombination

Autoionization and dielectronic recombination are processes involving two electrons Autoionization occurs in a doubly excited ion when the electron in the higher bound state is spontaneously excited from its energy level The energy gained has been accepted from the other electron, in the lower state, which has decayed from its own level into a lower state If the energy gain by the excited electron is sufficient, the electron may be ejected into the continuum and autoionization has occured

Dielectronic recombination is a two stage process and is not the exact inverse of auto-ionization In the first stage, an electron in the continuum recombines with an ionic bound state The extra energy is accepted by an electron in another bound state of the ion, which is then excited to a higher bound state Hence, a doubly excited state is created, so that the first step is the inverse of autoionization

In the second step, this doubly excited ion may decay, either via autoionization or through radiative decay of one of the bound levels If autoionization follows the recombination, there is no change in the state of excitation or ionization due to the reaction Dielectronic recombination only occurs when radiative decay follows the recombination since there is a change in the state of the ion in this case

33

1.7 The Emission and Absorption of Light Radiation in a Plasma

Emission spectroscopy is a very important diagnostic tool for hot plasmas For plasmas with short lifetimes, like laser produced plasmas, this may be the only reliable means of plasma evolution study The emission spectrum may carry information regarding, electron densities, temperatures and velocities Light radiation in plasma may be split into continuous, free-free and free-bound, and discrete, bound-bound, radiation Figure 1 8 shows these radiative, free-free, free-bound and bound-bound, processes within an ionization stage of ionization energy χ and containing levels of energy, E_i and E_j that induce light emission of frequency, ν, and energy, $h\nu$, where h is Planck'c constant

In the following sections, the various types of radiation in plasmas are described There is a description of the possible processes leading to an emission spectrum of light radiation and, in terms of line radiation, the possible line profiles and broadening mechanisms possible in laser produced plasma

1.7.1 Continuous Radiation

Continuous radiation may be split into two distinct parts, free-free and free-bound radiation Free-free radiation constitutes electron-photon processes having relatively high rates and there are two possible free-free processes, Bremsstrahlung (German for "braking radiation") and inverse Bremsstrahlung

In the Bremsstrahlung process, an electron travelling close to an ion is accelerated by the ion's Coulombic field and emits a photon Inverse bremsstrahlung is the inverse process and occurs when an electron, travelling close to an ion, absorbs a photon from the radiation field The emission spectrum for this radiation is obtained by averaging the cross-section of the process over the Maxwellian dis-
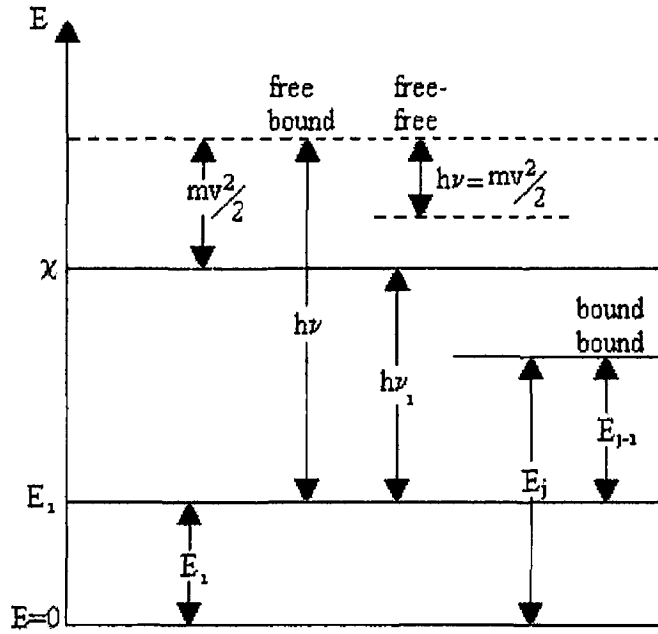
Figure 1 8 Transitions within an ionic stage

tribution of velocities The total free-free rate coefficients must be expressed as a sum over the ionization stages, k The emission coefficient for free-free radiation, ϵ_ν^{ff}, may be written, from the formalism in [36] as, [37],

$$\epsilon_\nu^{ff} = \sum_k \frac{16\pi e^6}{3c^3(4\pi\epsilon_0)^3(6\pi m^3 k_B)^{\frac{1}{2}}} k^2 \frac{N_e N_k}{T_e^{\frac{1}{2}}} exp\left(-\frac{h\nu}{k_B T_e}\right) \tag{1 81}$$

The absorption coefficient for free-free radiation, κ_ν^{ff}, may be written as the sum over the ionization stages in an atom of charge k, so that

$$\sum_k \kappa_\nu^{ff} = \frac{8\pi e^6}{3mhc(4\pi\epsilon_0)^3(6\pi m k_B)^{\frac{1}{2}}} N_e N_k \frac{k^2}{\nu^3 T_e^{\frac{1}{2}}} \tag{1 82}$$

Free-bound radiation is defined as either photoionization or radiative recombination Photoionization occurs when a bound electron absorbs a photon of suf-

35

ficient energy to eject the electron into the continuum and ionize the atom or ion The conservation of energy for this process gives

$$h\nu = \frac{1}{2}mv^2 + \chi_k - E_\imath = \frac{1}{2}mv^2 + h\nu_\imath \qquad (1\ 83)$$

The photoionization cross section, $\sigma_{k-1}(\nu)$, is the atomic cross section for this process and exists when the photon energy exceeds the ionization energy of level $\imath$ This process is only important in optically thick plasmas since the electron density must be sufficient to induce a significant photoionization rate relative to electron impact ionization This will occur when the mean free path of a photon is less than the plasma dimensions so that the probability of photon reabsorption is high The bound-free absorption coefficient per cm path for the process $(k-1, \imath) \rightarrow (k, 1)$ may be written [37]

$$\kappa_{\nu,\imath}^{bf} = N_{k-1}\sigma_{k-1,\imath}(\nu) \qquad (1\ 84)$$

so that the total absorption coefficient for an ionization stage is

$$\kappa_{\nu}^{bf} = \sum_\imath N_{k-1,\imath}\sigma_{k-1,\imath}(\nu) \qquad (1\ 85)$$

Photorecombination is the inverse process and the capture cross section, $\sigma_{k,1}$, may be related to photoionization through detailed balance [37]

$$\frac{\sigma(k, \imath \rightarrow k + 1, \hbar\omega)}{\sigma(k + 1 \rightarrow k, \imath, E_e)} = \frac{2mc^2 E_e g_{k+1,0}}{(\hbar\omega)^2 g_{k,\imath}} \qquad (1\ 86)$$

where $g_{k+1,0}$ and $g_{k,\imath}$ are the statistical weights of the ground state, 0, of the parent ion and the energy level, $\imath$, of the lower ionization stage, k, respectively The emission coefficient for free-bound radiation depends on the velocity distribution, $f(v)$, of the free electrons and, for the process $(k-1, \imath) \rightarrow (k-1, 1)$, may be written

$$\epsilon_{\nu,\imath}^{bf} = N_e N_{k,1} f(v)\sigma_{k,1}(\nu) \qquad (1\ 87)$$

36

Using a Maxwell-Boltzmann distribution and considering equation 1 83, the emission coefficient for an ionization stage may be written

$$\epsilon_\nu^{bf} = \frac{2h^4}{c^2(2\pi mkT_e)^{\frac{3}{2}}} exp\left(\frac{\chi_{k-1} - h\nu}{kT_e}\right) \sum_i \frac{g_{k-1,i}}{2g_{k,1}}\sigma_{k-1,i}(\nu)exp\left(-\frac{E_i}{T_e}\right) \quad (1\ 88)$$

Although there is a Boltzmann factor present in this equation, thermodynamic equilibrium applicability is not imperative for its validity [37]

The bound-bound transition causing line radiation is outlined in the following section

1.7.2 Line Radiation

Spectral line emission is the most important radiation process in hot plasmas that are not fully ionized, since the less ionized the plasma, the more discrete light radiation there will be Line emission corresponds to a bound-bound transition in a particular ion of charge k In the following sections the contributing factors to the emission and absorption coefficients are introduced and the equation of radiative transfer is derived

The emission rate, $I_{k,j\to k,i}$, of a spectral line per unit volume, per 4π steraradians in an optically thin medium may be written

$$I_{k,j\to k,i} = N_{k,j}\hbar\omega A(k,j \to k,i) \quad (1\ 89)$$

where k is the charge, $A(k,j \to k,i)$ and $N_{k,j}$ are the transition probability and population density of level i in ion of charge k, respectively, and $\hbar\omega = E_{upper} - E_{lower}$ is the transition energy between levels i and j Assuming detailed balance, the transition probability, or Einstein coefficient for spontaneous emission, $A_{j\to i}$, and the Einstein B coefficients for stimulated emission, $B_{j\to i}$, and absorption, $B_{i\to j}$, can be expressed [38]

$$A_{j\to i} = \frac{2\pi e^2\nu^2}{\epsilon_0 m_e c^3}\frac{g_i}{g_j}f_{ij} \quad (1\ 90)$$

and

$$g_i B_{i \to j} = g_j B_{j \to i} \qquad (1\ 91)$$

where m_e is the electron mass, g_i and g_j are the statistical weights of the lower and upper levels, respectively The Einstein A and B coefficients may be expressed in terms of one another using the following expression for the oscillator strength, which is the effective number of classical electron simple harmonic oscillators that would absorb radiation of energy $h\nu$ as strongly as the atom [39],

$$f_{ij} = \frac{4\epsilon_0 m_e h\nu}{e^2} B_{i \to j} \qquad (1\ 92)$$

The Einstein B coefficients correspond to atoms interacting with a radiation field whose energy density per unit frequency varies slowly with frequency, effectively averaging the spectral line profiles over the spectral line profile of the transition $j \to i$ However, in many cases, transition rates induced via a monochromatic wave of frequency, ν, are obtainable by multiplying these frequency averaged B coefficients by a normalised line shape function, ϕ_ν This line shape function must be normalised to unity as it represents the probability per unit frequency to observe a photon emitted in the vicinity of the line centre, ν_0, in the frequency range ν and $\nu + d\nu$ so that

$$\int_{line} \phi_\nu d\nu = 1 \qquad (1\ 93)$$

The different possibilities for the spectral line profile are outlined in the following subsection

1.7.3 Line Profiles

There are three main line profiles, ϕ_ν, used to represent spectral lines There is the Lorentzian profile, which is used in natural and stark/pressure line broadening,

38

(see section 1 7 5) The normalised Lorentzian AFR may be written as

$$\mathcal{L}(\delta\nu) = \frac{2}{\pi\Delta_{\mathcal{L}}} \frac{1}{(\delta\nu)^2 + \left(\frac{\Delta_{\mathcal{L}}}{2}\right)^2}$$ (1 94)

where $\delta\nu = \nu - \nu_0$ and ν_0 is the resonant frequency of the transition $\Delta_{\mathcal{L}}$ is the full width at half maximum (FWHM), see equation 1 111

Doppler shifts are dependent on the Maxwellian (thermal) velocity distribution of particles in the medium of interest and leads to a normalised Gaussian line profile written as

$$\mathcal{G}(\delta\nu) = \left(\frac{ln2}{\pi}\right)^{\frac{1}{2}} \frac{2}{\Delta_{\mathcal{G}}} exp \left[-4ln2 \left(\frac{\delta\nu}{\Delta_{\mathcal{G}}}^2 \right) \right]$$ (1 95)

where $\Delta_{\mathcal{G}}$ is the half-width (FWHM) is related to the temperature of the emitting particles

Both the Lorentzian and Gaussian line profiles are likely to contribute to the true line profile It is for this reason that the Voigt line profile was developed A Voigt profile is the result of a convolution of Lorentian and Gaussian profiles,

$$\mathcal{V}(\nu_0 - \nu) = (\mathcal{L}(\nu_0 - \nu) \otimes \mathcal{G}(\nu_0 - \nu)) = N \int_0^\infty \mathcal{L}(\nu - \nu')\mathcal{G}(\nu' - \nu_0)d\nu'$$ (1 96)

where N is a normalisation constant and $\otimes$ indicates convolution The Voigt shape is approximately Gaussian close to the line centre and exhibits a $1/(\nu - \nu_0)^2$ decrease in the line wings as in the Lorentzian profile

The Voigt function cannot be expressed analytically However, analytical approximations, relieving the computational expense, have been developed, such as the work of [40] This approximation uses four generalized Lorentzians in two variables and gives a numerical function for the Voigt profile evaluation

1.7.4 The Equation of Radiative Transfer

The equation of radiative transfer describes the change in intensity of a beam of radiation, I_ν, as it passes through a medium of excited ions confined to a solid
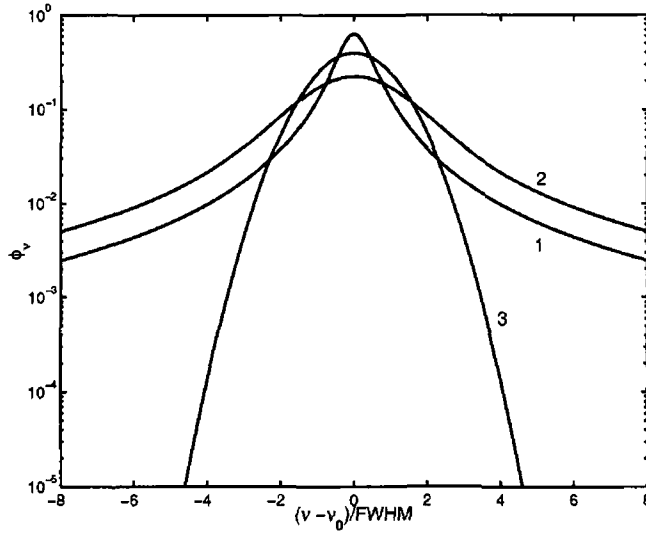
Figure 1 9 Comparison of the possible line profiles of bound-bound emission lines, 1, 2 and 3 correspond to Lorentzian, Voigt and Gaussian profiles, respectively

angle, $d\Omega$ The plasma may be observed along a z-axis of a coordinate system, see figure 1 10 This change depends on the value of the coefficients describing the emission and absorption of radiation

The emission coefficient, ϵ_ν, is heavily dependent on the Einstein coefficients for spontaneous emission so that

$$\epsilon_\nu = \frac{h\nu}{4\pi} A_{ji} N_j(r) \phi_\nu \qquad (1\ 97)$$

while the absorption coefficient, κ_ν, depends on the Einstein B coefficients for stimulated emission, B_{ji}, and absorption, B_{ij}, and is expressed as

$$\kappa_\nu = \frac{h\nu}{4\pi} (B_{ij} N_i - B_{ji} N_j) \phi_\nu \qquad (1\ 98)$$

Since the change in intensity per unit length along this beam is the difference between the radiation emitted and absorbed, the general equation of radiative trans-

40
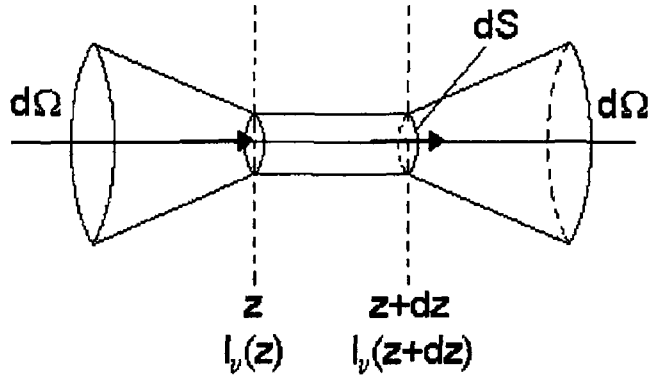
Figure 1 10   Diagram indicating the transport of light radiation in plasma

fer may be written

$$\frac{1}{c}\frac{dI_\nu}{dt} + \frac{dI_\nu}{dz} = \frac{h\nu}{4\pi}\left(A_{ji}N_j + B_{ji}N_jI_\nu - B_{ij}N_iI_\nu\right)\phi_\nu \qquad (1\ 99)$$

This may be reduced to a simpler form if the plasma is in steady state so that conditions do not change too rapidly in time and the first factor on the left hand side can be neglected   Using equations 1 97 and 1 98 this may be written in the reduced form

$$\frac{dI_\nu}{dz} = \epsilon_\nu - \kappa_\nu I_\nu \qquad (1\ 100)$$

With the emission and absorption coefficients resolved in terms of frequency and position, the equation of radiative transfer may be solved and the intensity obtained at any point

Equation 1 100 may be solved if it is multiplied by the integration factor $exp(\int \kappa_\nu dz)$ and rearranged to give

$$\frac{d}{dz}\left(I_\nu(z)exp\left(\int_0^{z_0} \kappa_\nu dz\right)\right) = \epsilon_\nu exp\left(\int_0^{z_0} \kappa_\nu dz\right) \qquad (1\ 101)$$

41

Upon integrating 1 101, the solution becomes

$$I_{\nu,z} = I_{\nu,0} exp\left(-\int_0^{z_0} \kappa_{\nu,z} dz\right) + \int_0^{z_0} \epsilon_{\nu,z} exp\left(-\int_z^{z_0} \kappa_{\nu,z} dz\right) dz \quad (1\ 102)$$

where ϵ_ν and κ_ν are given in equations 1 97 and 1 98, respectively I_ν is the external radiation incident on the plasma, with $I_\nu = 0$ corresponding to no external radiation incident on the plasma The optical depth of the plasma, τ_ν, determines the amount of attenuation experienced by a collimated beam of light as it passes through the medium and is given by

$$\tau_\nu = \int_z^{z_0} \kappa_\nu dz \quad (1\ 103)$$

and if $\tau_\nu \ll 1$, so that the plasma is optically thin, equation 1 102 reduces to

$$I_\nu = \int_0^{z_0} \epsilon_\nu dz \quad (1\ 104)$$

1.7.5 Line Broadening

Line Broadening is an important factor in the analysis of spectral line emission The line width is an important diagnostic tool due to its sensitivity to the local microfields and can, thus, provide information regarding the temperature and densities in the plasma unavailable using other diagnostic means Atomic lifetimes, velocity distributions, collisions and local electrostatic fields may all contribute to spectral line broadening In the following subsections, the three main broadening mechanisms of importance to the plasmas of interest are outlined

Natural Line Broadening

Natural line broadening depends on the finite lifetime of atomic excited states The probability of finding an ion at a particular energy, $E = h\nu$, at time, t, in the upper state can be expressed as an exponentially decreasing function, which leads

42

to a Lorentzian line profile This type of broadening sets a theoretical limit on the resolution possible for any spectral line with the full width at half maximum intensity given by [38]

$$\delta \nu_{\frac{1}{2}} = \frac{1}{\tau_j} \qquad (1\ 105)$$

which is the width of the level predicted by the uncertainty principle

$$\delta E \delta t = h \delta \nu \, \tau_j = h \qquad (1\ 106)$$

The total radiative lifetime, τ, is related to the sum of the transition probabilities of the electric dipole transitions from upper level, j, to all lower levels, i, so that [38]

$$\tau_j = \frac{1}{\sum_i A_{ji}} \qquad (1\ 107)$$

Pressure Broadening

This type of broadening is also known as collisional or Stark broadening and is caused by the emitting atom colliding/interacting with nearby particles There are two main approaches used in the study of pressure broadening The first, known as the impact approximation, was devoloped by Lorentz and is based on the assumption that the time taken for a collision, τ_c, is much less than the time between collisions, τ_{bc} and that each collision involves one perturber [41] From the properties of Fourier transforms, a sinusoidal wave of duration, τ, has a frequency width of order

$$\delta \nu \approx \frac{1}{\tau_{bc}} \qquad (1\ 108)$$

Considering the statistical nature of τ_{bc} it is possible to show that the wave decreases exponentially according to $exp\left(-\frac{t}{\tau_{bc}}\right)$ Applying a Fourier Transform leads to a Lorentzian line shape

43

The other approach, known as the quasistatic approach, was developed by Holtzmark The energy levels, E_t and E_k are perturbed by the interations V_t and V_k, respectively Implementing the Frank Condon principle that the transition takes place at constant perturber distance, R, the change in instantaneous frequency of the transition may be written

$$\delta\nu_{kt} = \frac{V_k(r) - V_t(r)}{h}$$ (1 109)

This line broadening may be calculated by averaging over R The shifted frequency peaks at the distance of closest approach

$$R_c = \tau_{bc}\bar{v}$$ (1 110)

with $\bar{v}$ being the mean perturber speed

For neutral atoms and singly ionized, non-hydrogenic, ions, Stark broadening is caused mainly by electrons and the FWHM of these lines may be calculated using the electron impact approximation and corrected for the relatively insignificant quasistatic broadening This leads to a symmetical, but shifted, line profile whose FWHM and shift may be written as [42, 43]

$$\delta\nu_{\frac{1}{2}} = 2W\left(\frac{N_e}{10^{16}}\right) + 3\,5A\left(\frac{N_e}{10^{16}}\right)^{\frac{1}{4}}\left(1 - \frac{3}{4}N_D^{-\frac{1}{3}}\right)W\left(\frac{N_e}{10^{16}}\right)$$ (1 111)

$$\delta\nu_{shift} = D\left(\frac{N_e}{10^{16}}\right) \pm 2A\left(\frac{N_e}{10^{16}}\right)^{\frac{1}{4}}\left(1 - \frac{3}{4}N_D^{-\frac{1}{3}}\right)W\left(\frac{N_e}{10^{16}}\right)$$ (1 112)

In the above formulae, the electron density is in cm^{-3} with the FWHM, $\delta\nu_{\frac{1}{2}}$, and line shift, $\delta\nu_{shift}$, both in angstroms N_D corresponds to the total number of particles within the Debye sphere These formulae are applicable to neutrals only and may be made applicable to single ions by changing the value $\frac{3}{4}$ to 1 2 [42] Their range of applicability is where $N_D \geq 2$ and $0\,05 < A\left(\frac{N_e}{10^{16}}\right) < 0\,5$ [42] The parameters W, D and A are slowly varying functions of temperature and are

available in extensive tables in [44] In table [45], these parameters are listed for the lithium transitions used in the radiation model

To calculate densities of an accuracy of better than $30-40\%$, a convolution of the electron and ion profiles is necessary so that the entire profile is calculated and the total linewidth extracted from it [42]

Doppler Broadening

Doppler broadening results from atoms/ions radiating while moving at a certain velocity with respect to a fixed observer It is assumed that the velocity distribution at any point in the plasma is composed of a streaming component, causing a frequency shift, and a thermal component, which contributes to the line profile

The frequency shift, $\delta\nu = \nu' - \nu_0$ may be represented as

$$\nu' = \nu_0 \left(1 \pm \frac{v}{c}\right) \tag{1 113}$$

The positive sign corresponds to velocity components, v, towards the observer and the frequency will increase, blue shift, while the velocity component travelling away from the observer will decrease the frequency of emitted light, red shift [46] In the case of expanding laser produced plasma the plasma expands radially outward from the target normal axis In equation 1 113, v represents either $v(r)$, if the line of sight is along the plume diameter, or $v_y = v(r)cos\theta$, if the line of sight is along a chord, see figure 1 11

If a Maxwell velocity distribution is present, a Gaussian line profile results with a FWHM, $\delta\lambda_{\frac{1}{2}}$, given by

$$\delta\lambda_{\frac{1}{2}} = \sqrt{\frac{8ln2k_BT\omega_0^2}{mc^2}} \tag{1 114}$$

where m is the particle mass, T is the plasma temperature and ω_0 is the central wavelength In non-thermal plasmas, it is possible for the induction of further

doppler broadening If the velocity distribution is not Maxwellian, altering the intensity profile There may be non-negligible turbulent velocities present, contributing to the overall velocity Also, there may be mass motion of the entire plasma, or clumps of it

Consider an observer situated at a fixed position and looking in a direction parallel to the [Z] axis, see figure 1 11 A fixed observer will see doppler shifted light proportional to the magnitude and direction of the expansion velocity along the plume chord
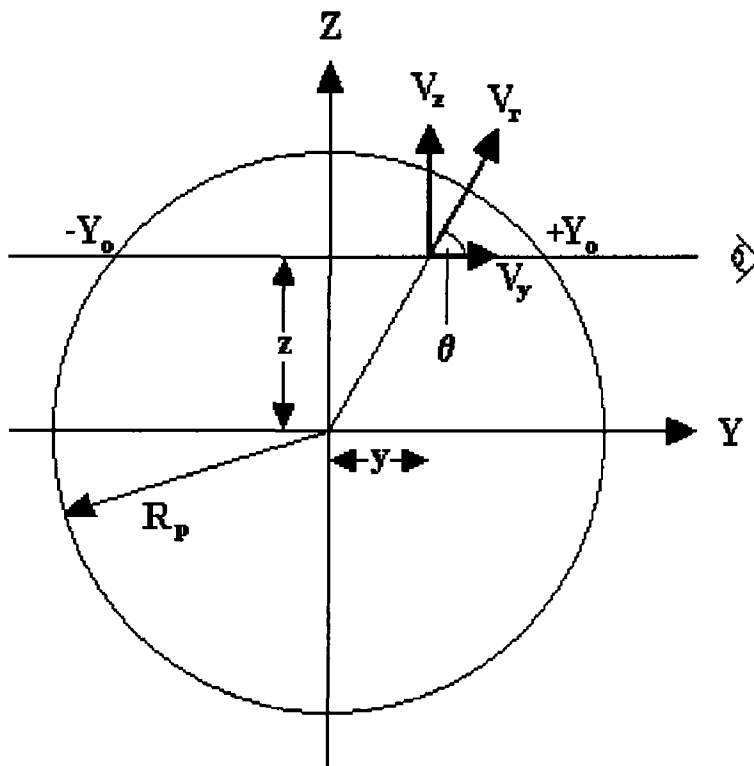
Figure 1 11 Position of observer relative to cross-section through plasma plume
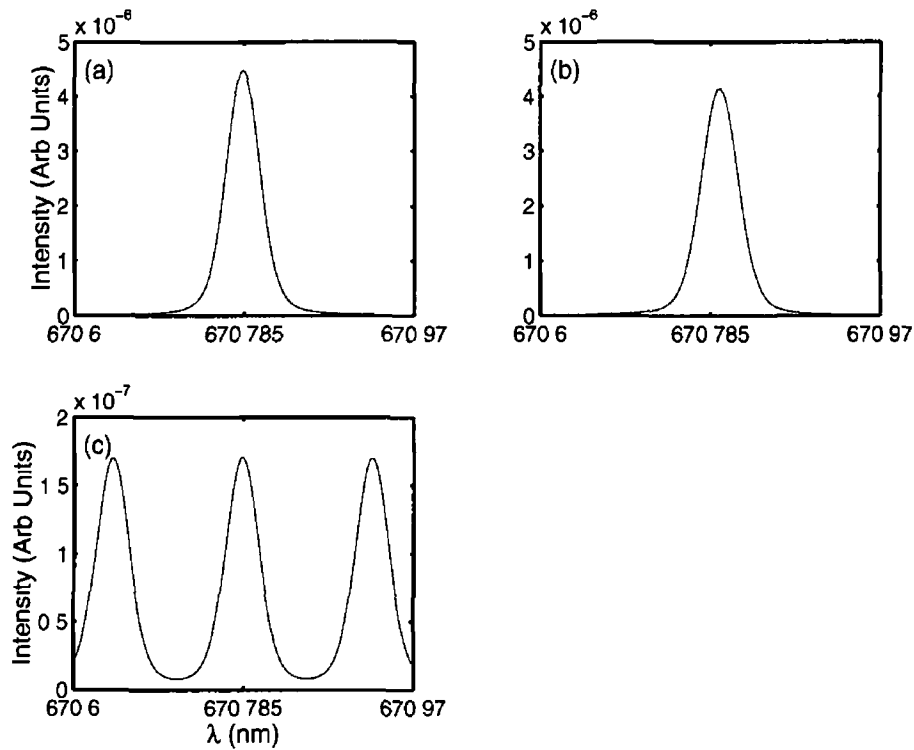
Figure 1 12 Display of the influence of the various velocity profiles from 1 14 on the 2^2p-2^2s emission line in Li^0 (a) No velocity distribution, (b) and (c) correspond to the velocity profiles in figure 1 14 (a) and (b), respectively

Figure 1 12 shows the Doppler shifted spectra for three typical velocity distributions from this work for a line of sight across the plume diameter The population distributions used were gaussian, as in the isothermal self-similar model The increased frequency, blue-shift, corresponding to velocities towards the observer and decreased frequency, red-shift, corresponding to velocities away from the observer are clearly visible and become more pronounced with increased velocity However, there is also a third peak in the centre of the profile This is caused by the central peak of the population distributions of both levels as predicted by the density profile, see figure 1 13 This third peak was not observed in [46, 47] since

at least one of the population density profiles were depressed at the centre and, hence, reduced the intensity at the centre
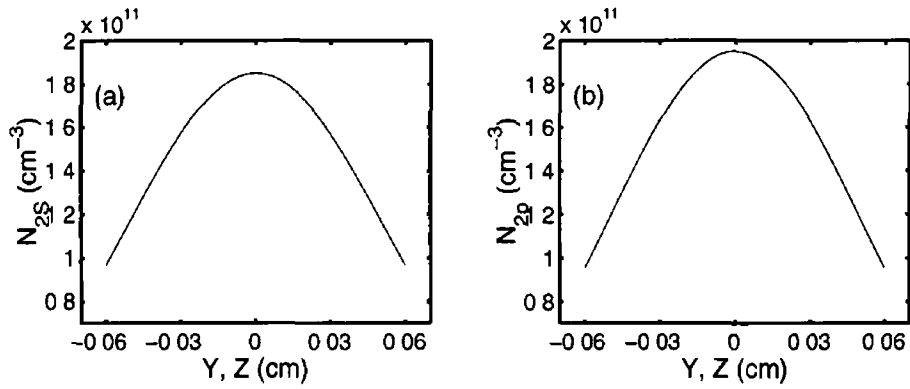
Figure 1 13 Distribution of population densities for the levels in the 2^2p-2^2s transition used in the Doppler shifted spectra generation (a) Population density of the 2^2s energy level and (b) Population density of the 2^2p energy level
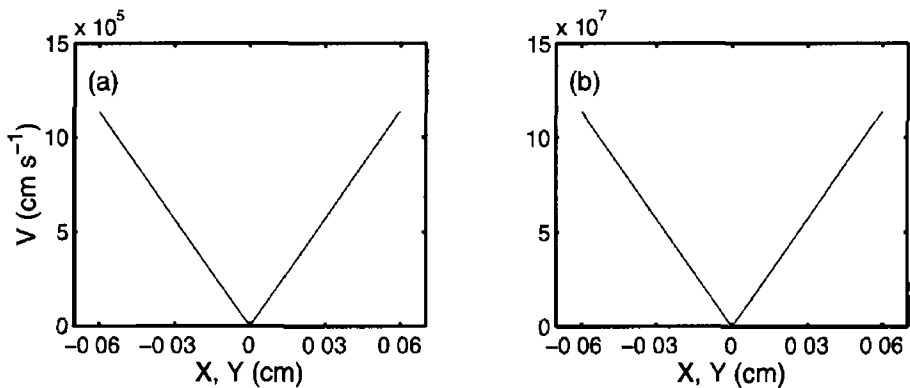

Figure 1 14 Velocity distribution of particles used in generation of Doppler shifted spectra across plasma cross-section as in figure 1 11

In figure 1 12, it may be seen that for the velocity to induce significant line splitting requires a velocity of $> 10^8$ cms^{-1} However, typically, laser produced

48

plasma velocities rarely exceed 10^6 cms^{-1} and the severity of the line splitting in 1 12 (a) will be very difficult to observe experimentally

1.7.6   The Influence of Light Radiation on Plasma Expansion

To develop a theoretical model for the analysis of laser plasma expansion including both expansion and radiation dynamics may be achieved by treating these model components separately or calculating them simultaneously and self consistently The correct approach may be found by consideration of the effect of light radiation on plume expansion

In high temperature laser plasma, radiation energy may be comparable to expansion energy and affect the expansion dynamics significantly, so that the radiation and expansion properties must be calculated self-consistently [48] Recent studies have been performed on laser induced plasma regarding the influence of radiant energy on the expansion dynamics and, for temperatures above 10 eV, the radiation energy can begin to shoulder a significant contribution of the total energy in laser produced aluminium plasma[49] In [50], the influence of radiation on dynamics was considered for fluences ranging between 10 and 25Jcm^{-2} It was shown that the exclusion of radiation may reduce the total plume energy by up to 35% at early times when the laser light is absorbed by the plume However, these fluences are higher than those typical of PLD, which applies to plasma initiated with much lower fluences and having initial temperatures of just a few eV It is, hence, possible to consider a model with hydrodynamics and radiation properties treated separately in conditions applicable to PLD

In the following chapters, a model exploitable in the analysis of laser produced lithium plasma is employed This model is used in conditions consistent with the PLD process with the hydrodynamics and radiation processes decoupled, since the temperatures in the plume remain low enough to ensure that radiation processes

49

remain negligible, in comparison to hydrodynamic processes

1.8 Conclusions and Objectives of Present Work

This chapter has been devoted to outlining the theoretical ideas used in this work In the following chapter our model will be described This model was developed to provide a complete description of a lithium ablation plume expanding into vacuum

In the literature, for example [23, 51–53], intensified ICCD camera images of visible laser plasma emission clearly show the position of maximum intensity in the plume evolving in time The 'shifted', equation 1 29, Maxwellian distribution has been used in the analysis of time of flight spectra in laser ablation plasma [23, 51–53] However, the existing isothermal [17] and isentropic [54] self-similar expansion models do not include bulk motion of the plume, since the density profiles in both cases remain located on the target surface, at $x, y, z = 0$ This implies the need for the inclusion of an instantaneous velocity of the PMD, $x, y, z = 0$ with respect to the target, to the self-similar models to account for this bulk plume motion, see figure 1 5 for comparison of plume shape with and without inclusion of bulk motion

The analytic gas dynamics models outlined in section 1 4 2 have been modified to include the bulk motion of the plume and, hence, evolution of the PMD These isothermal and isentropic self-similar solutions also predict differing plasma expansion dynamics for the same set of initial conditions To test this difference and to try and determine the better model for describing laser plasma expansion, these models will be tested over a wide range of initial parameters for comparison with experimental results obtained from ICCD camera images of expanding Li plasma plumes

These self-similar models produce density and temperature predictions during the expansion, which will be used as input parameters into an atomic kinetics model to calculate electron, neutral, ion and energy level populations This will allow the determination of plume regions in space and time where various equilibrium models and steady-state conditions apply

Finally, the full equation of radiative transfer equation in the steady-state region will be solved along chords through the target normal at various positions above target This spectra will be compared with time-integrated experimental spectra taken at these positions The model will be used to analyse and determine the cause of counter intuitive behaviour observed in these spectra In summary, a full model has been developed and utilised to analyse Li laser ablation plumes expanding into vacuum

Chapter 2

Models and Methods

This chapter describes the model and numerical methods employed to analyse the evolution of plasma parameters and coefficients in the plume The next section outlines the hydrodynamics models and the method used to simulate the plasma expansion This is followed by the link to the atomic physics and how this was implemented using atomic cross-sections with a description of their calculation This finally leads to the radiation model and how this is then tied to the atomic and, hence, hydrodynamic model

2.1 Hydrodynamics and the Self-Similar Model

The construction of the solution to the self-similar expansion model has been approached from isentropic and isothermal viewpoints Here, the general equation describing self-similar expansion is recalled

$$X\frac{\partial^2 X}{\partial t^2} = Y\frac{\partial^2 Y}{\partial t^2} = Z\frac{\partial^2 Z}{\partial t^2} = \beta \left(\frac{X_0 Y_0 Z_0}{XYZ}\right)^{\gamma-1} \tag{2 1}$$

where X_0, Y_0 and Z_0 are the initial dimensions of the plume and X, Y and Z are the plume dimensions at time t and γ is the ratio of specific heats

52

In the case of the isentropic model β is given by

$$\beta = (5\gamma - 3)\frac{E}{M} \tag{2 2}$$

where the energy, E, and mass, M, are integrals over the plume volume
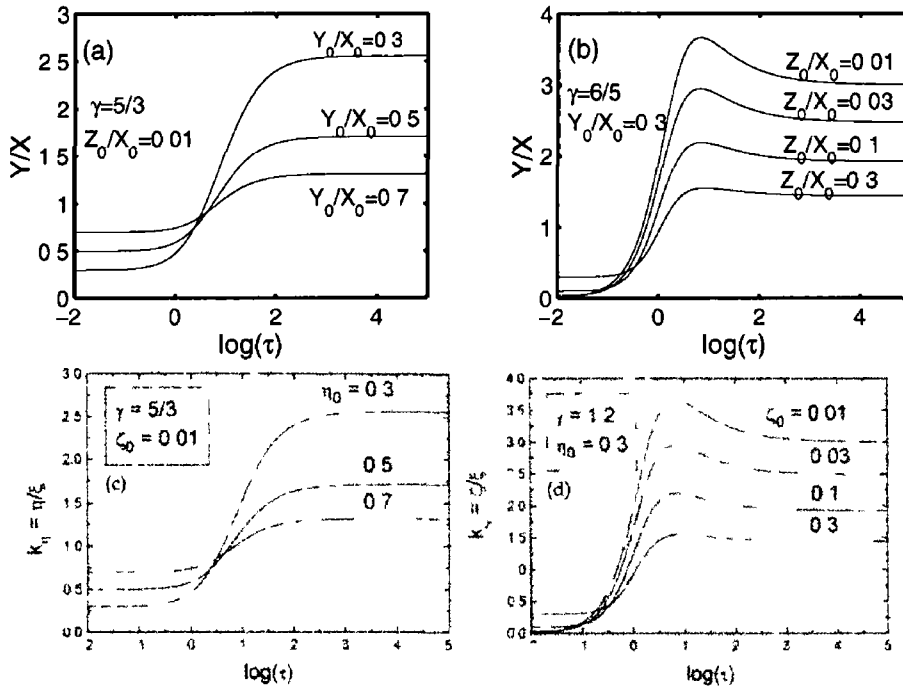
Figure 2 1 Evolution of the ratio of dimensions (a) Y/X for various sets of initial ratio Y_0/X_0 with the other ratio $Z_0/X_0 = 0\ 01$ and (b) Y/X for various sets of initial ratio Z_0/X_0 with the other ratio $Y_0/X_0 = 0\ 3$ Both cases are plotted as a function of the logarithm of time $log(\tau)$ (c) and (d) Same as for (a) and (b) reproduced from [54] with kind permission of the journal editor

The isentropic model was established analytically in [15, 54] to display the effect of the variation of γ and ratios of X, Y and Z In figures 2 1, this variation is reproduced, calculated from the solution to equation 2 1   The Runge-Kutta method is a very practical numerical method for solving initial value problems and has been used to solve the self-similar solution, equation 2 1 Figures 2 2 and

53

2 1 were produced as a result of the fifth order Runge-Kutta method, see Appendix A 1 These indicate its accuracy through the reproduction of published results and that this method has been implemented correctly in this work

In the isothermal solution for this type of self-similar model, β in equation 2 1 becomes

$$\beta = (1 - \gamma)\frac{E}{M} \qquad (2\ 3)$$

This isothermal self-similar model was adopted in [17] for the analysis of Yttrium, atomic weight of 89 0, ablation with a YAG laser Figure 2 2 displays these results from [17] reproduced, again, using the fifth-order Runge-Kutta solution
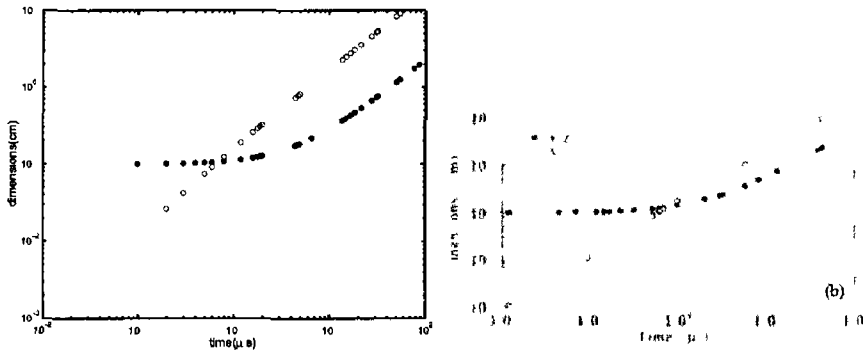
Figure 2 2 (a)Time history of (Y,Z) and perpendicular (X) dimensions in the plasma (b) Same as for (a) reproduced from [17] with kind permission of the journal editor

2.1.1 Plume Geometry Evolution

As described in section 1 4 3, if sufficient collisions occur, particles may attain velocities in the negative direction allowing the formation of a Knudsen layer and may induce a change in the Maxwellian distribution used for the analysis of time of flight spectra This 'shifted' Maxwellian distribution, equation 1 29, has been used in the analysis of time of flight spectra in laser ablation plasma

[23, 51–53] However, this type of distribution only deals with average, rather than instantaneous, centre-of-mass velocities, v_c

Another approach to include the plume's bulk motion in the expansion dynamics may come through a dynamic source effect During the laser pulse, the continuous vaporization of target material will induce a pressure on the target, which will only drop after the pulse The plume may experience increased velocity due to this effect through the conservation of momentum This dynamical source effect has been used by Chen [11, 55] to explain the increased velocity of the expanding plume seen experimentally compared to the models that do not include this effect

In the self-similar models for isothermal [17] or isentropic [54] expansions, the position of maximum density (PMD) remains at the centre of the target spot and on the target surface Inclusion of the plume's bulk motion, superimposed onto the self-similar expansion, would allow the movement of the PMD and, hence, closer agreement with experimental density profiles

To include the bulk motion in the model used here, the pressure profile from the self-similar model was integrated over the target surface and using conservation of momentum, the velocity of the PMD, V_{PMD}, may be calculated This velocity away from the target is described using equation 1 31, with the pressure profile depending on the model used This velocity must be solved consistently and concurrently with the equation of motion, equation 2 1 The Runge-Kutta fifth-order algorithm was implemented to solve these equations simultaneously To calculate the integral of the plasma pressure on the target, the Romberg integration method was used, see Appendix A 2 This method for calculating V_{PMD} was used by [24] for the isothermal solution for Calcium, Strontium and Barium

55

2.2 Atomic Population Calculations

With the full hydrodynamics models implemented, the plume spatial and temporally resolved density and temperature (spatially resolved in the isentropic solution) are available These provide the link between the hydrodynamics and atomic physics, and may yield electron, ion and neutral populations In the following sections, a method used to calculate these densities in a plasma containing up to, and including, doubly ionized ions is described Cross-sections that were used are displayed The electron density is then used in the calculation of energy level populations for lithium neutral Finally, the various cross-sections used in the energy level populations are displayed

2.2.1 Electron Density Calculation

The scope of the gas dynamic models of [15, 17] has been extended by explicitly calculating the ionization balance throughout the plume as a function of time For this purpose, the densities and temperatures yielded by these models, from equations 1 20 and 1 25, are used as input parameters to the steady state model in the electron, atom and ion population densities calculations We establish the following closed-set of equations, that represent electrical neutrality, particle conservation and two collisional radiative steady state (CRSS) equations for the charge state distribution of Li, Li$^+$ and Li^{2+}, respectively These are

$$n_e = n_1 + 2n_2 \qquad (2\ 4)$$

$$n = n_0 + n_1 + n_2 \qquad (2\ 5)$$

$$\frac{n_1}{n_0} = \frac{S_0}{R_1 + \alpha_1 n_e} \qquad (2\ 6)$$

$$\frac{n_2}{n_1} = \frac{S_1}{R_2 + \alpha_2 n_e} \qquad (2\ 7)$$

56

where $n_k(k = 0, 1, 2)$ are the densities of neutral, singly-ionized and doubly-ionized lithium, respectively S_k is the corresponding average electron-impact ionization rate coefficient (see e g [30]), α_{k+1} is the average three-body recombination rate coefficient and R_{k+1} is the average radiative recombination rate coefficient Dielectronic recombination has been neglected since its influence is negligible in the temperature range of interest in this work, see section 2 3 3 Triply-ionized lithium was not considered in our model in view of the high value of the ionization potential of Li^{2+} (122 4 eV) This system can be reduced to form a single cubic equation whose solution yields the electron and, hence, ionic population densities,

$$\alpha_1\alpha_2 n_e^3 + (R_2\alpha_1 + R_1\alpha_2 + S_0\alpha_2)n_e^2 + (S_0S_1 + R_1R_2 + S_0R_2 -$$

$$nS_0\alpha_2)n_e - S_0R_2n - 2S_0S_1n = 0 \qquad (2\ 8)$$

With the electron, atom and ion populations now available, the procedure for the calculation of energy level populations will be described, including a host of levels of Li^0

2.2.2 Level Population Calculations

A Collisional Radiative Steady State (CRSS) model was utilised to calculate the level populations by solving the following system of ζ coupled rate equations

$$M \bullet N = 0 \qquad (2\ 9)$$

where N_ζ is the vector of the level populations and M is the matrix of the rate coefficients connecting them The general term of M is given by

57

$$0 = \sum_{i<j} n_e N_j C_{ji} + \sum_{j>i} n_e N_j D_{ji} + \sum_{j>i} N_j A_{ji} \kappa_{ji}$$

$$+ n_e n_1 (\alpha_{k+1,i} \kappa_{ci} + n_e R_{k+1,i}) - N_i \left(\sum_{j>i} n_e C_{ij} \right.$$

$$\left. + \sum_{j<i} n_e D_{ij} + \sum_{j<i} A_{ij} \kappa_{ij} + n_e S_{k,i} \right) \qquad (2.10)$$

where C_{ij} and D_{ij} are the electron impact excitation and deexcitation rate coefficients for transitions from level i to j. $S_{k,i}$, $\alpha_{k+1,i}$ and $R_{k+1,i}$ are the electron impact ionization, three body recombination and radiative recombination rate coefficients of level i in ionization stage k.
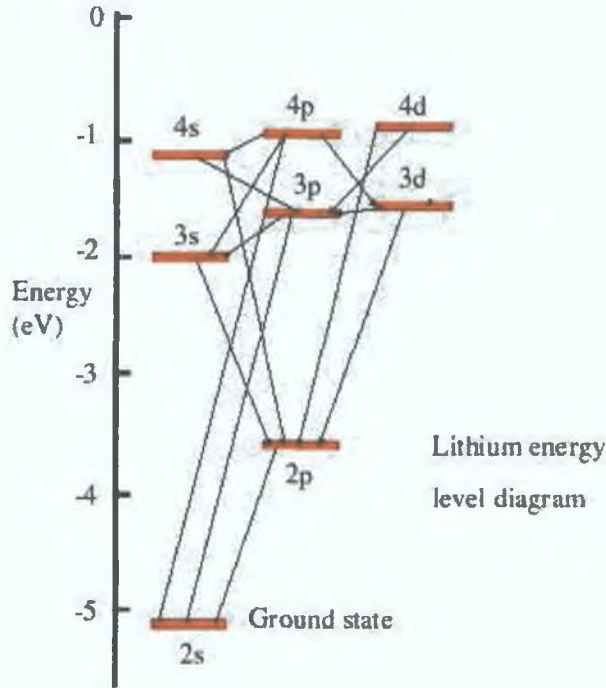
Figure 2.3: Energy Level Diagram for Li neutral indicating the transitions included

Figure 2.3 shows the energy level diagram for Li neutral and the transitions between the levels that were included in solving equation 2.9. The fractional

58

population of all levels up to the 4d state have been included, see table 2 2 2 The transition probabilities, A_{ji}, oscillator strengths, f_{ij}, electron configurations and transition wavelengths, λ, were taken from [31]

$j \to i$	Transition	A_{ji}, 10^7s^{-1}	f_{ij}	λ, nm
$2 \to 1$	$2^2p \to 2^2s$	3 72	0 753	670 8
$3 \to 2$	$3^2s \to 2^2p$	3 49	0 115	812 6
$4 \to 1$	$3^2p \to 2^2s$	0 117	0 006	323 2
$4 \to 3$	$3^2p \to 3^2s$	0 337	1 226	2687 7
$5 \to 2$	$3^2d \to 2^2p$	7 16	0 666	610 3
$5 \to 4$	$3^2d \to 3^2p$	$3\,81 \times 10^{-5}$	0 074	27949 0
$6 \to 2$	$4^2s \to 2^2p$	0 101	0 013	497 2
$6 \to 4$	$4^2s \to 3^2p$	0 746	0 223	2446 5
$7 \to 1$	$4^2p \to 2^2s$	0 142	0 005	274 1
$7 \to 3$	$4^2p \to 3^2s$	$3\,69 \times 10^{-4}$	$1\,935 \times 10^{-4}$	1079 2
$7 \to 5$	$3^2d \to 4^2p$	$5\,41 \times 10^{-3}$	0 0185	1927 5
$7 \to 6$	$4^2p \to 4^2s$	$7\,72 \times 10^{-3}$	1 635	6861 1
$8 \to 2$	$4^2d \to 2^2p$	0 230	0 118	460 3
$8 \to 4$	$4^2d \to 3^2p$	0 0685	0 527	1754 6
$8 \to 7$	$4^2d \to 4^2p$	1 28e-5	0 136	65006

Table 2 1 All of the discrete transitions used in the energy level population calculations of Li^0 with the energy levels numbered from $i=1$ to 8

We discuss now the procedure used to solve the above equations numerically Equation 2 8 is solved first, assuming initially the average collisional ionization rate coefficient S_0 to be equal to $S_{0,1}$ The electron density, n_e, is calculated assuming no continuum lowering

The electron density n_e thus obtained is now used as an input parameter into the system of equations 2 9, which is then solved using Gauss-Jordan elimination The ground state population was set at 1 0 and all other fractions calculated and added to give the total populations

The value of n_e obtained is now used to calculate the Debye length and, hence, the value by which the ionization potential must be lowered, see equation 1 47 A new value for S_0 is then generated using the new population probabilities of the energy levels The new ionization potential and new S_0 are now used to calculate a new value of n_e This procedure is repeated until the value of n_e changed by less than one part in 10^5 between iterations

2.3 Rate Coefficients

In this section all of the rate coefficients used in the calculation of atom, ion and energy level populations are displayed

2.3.1 Electron Impact Ionization and Three-Body Recombination Rate Coefficients

The average electron impact ionization rate coefficient, S_k, was evaluated assuming that the average collisional ionization rate coefficient S_0 to be equal to $S_{k,1}$, since the main contribution comes from the ground state Figure 2 4 shows the average electron impact ionization rate coefficient that was used in the calculation of the electron density, see equation 2 8

Figure 2 5 and 2 6 shows the electron impact ionization rate coefficient for the various energy levels that were included in the set of rate equations, equation 2 10 for the calculation of energy level populations All of the three-body rate coefficients were calculated assuming detailed balance
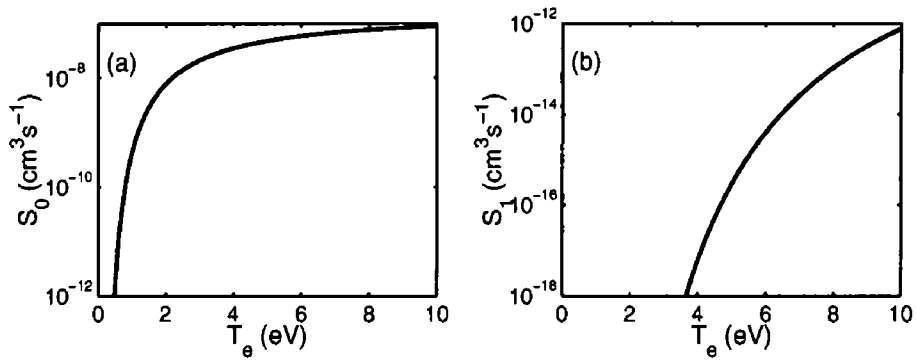
Figure 2 4   Electron impact ionization rate coefficient evaluated for Li^0 (a) and Li^+ (b) as a function of electron temperature
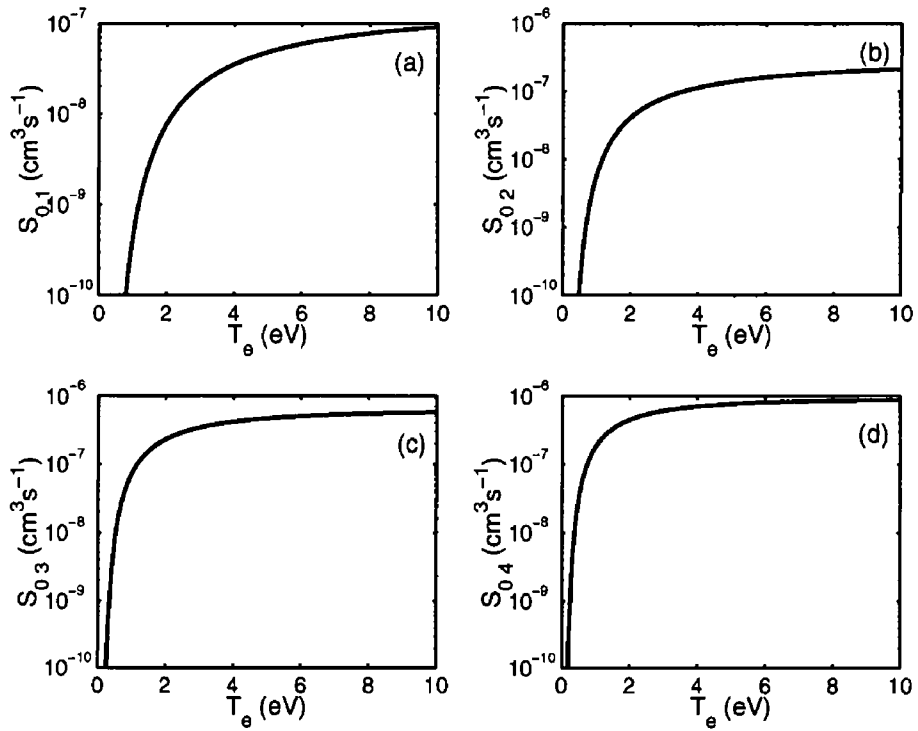
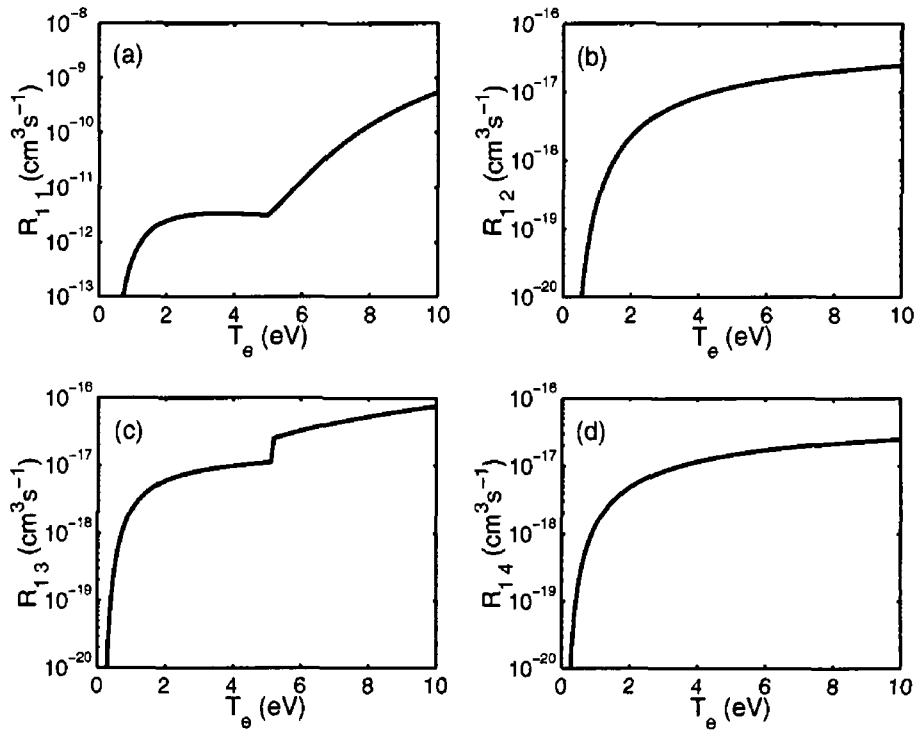Figure 2 5   Electron impact ionization rate coefficient evaluated for energy levels in Li^0 for (a) 2^2s , (b) 2^2p, (c) 3^2s and (d) 3^2p, as a function of electron temperature
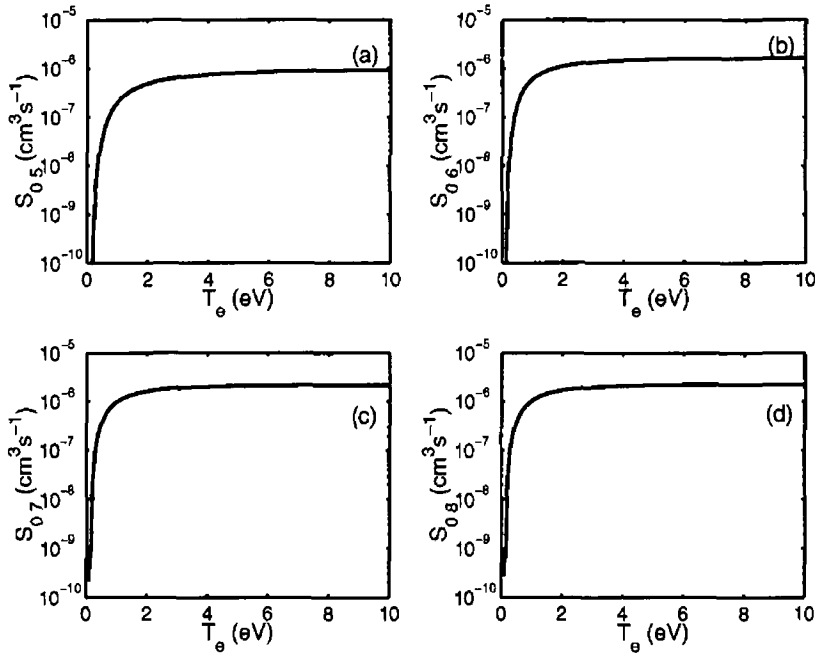
Figure 2 6   Electron impact ionization rate coefficient evaluated for energy levels in Li^p for (a) 3^2d, (b) 4^2s, (c) 4^2p and (d) 4^2d, as a function of electron temperature

2.3.2 Photoionization and Radiative Recombination

In [56] a simple analytical formula was proposed to calculate the average radiative recombination rate coefficients for H-like, He-like, Li-like and Na-like ions of all elements from H to Zn ($Z = 30$) and is given by

$$R_r(t) = a \left[\sqrt{\frac{T}{T_0}} \left(1 + \sqrt{\frac{T}{T_0}}\right)^{1-b} \left(1 + \sqrt{\frac{T}{T_1}}\right)^{1+b} \right]^{-1} \qquad (2\ 11)$$

where a, b, T_0 and T_1 are the fitting parameters   The accuracy of this formula is better than 4% with a maximum error of 6% for all Li-like and Na-like species Figure 2 7 displays radiative recombination rate coefficients calculated using the fitting formula 2 11 using fitting parameters given in [56]
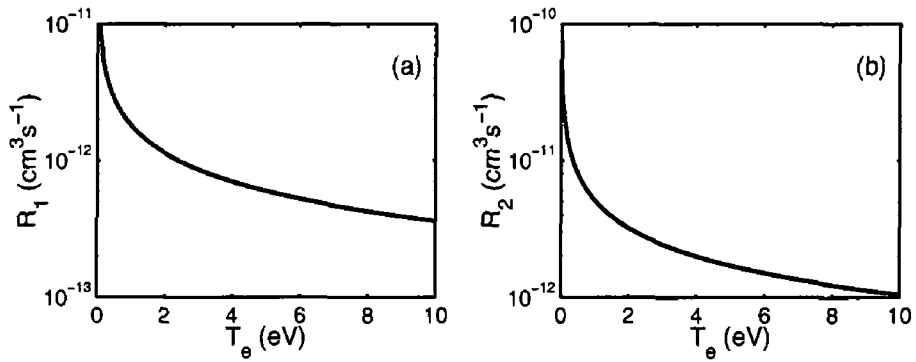
Figure 2 7 Average radiative recombination rate coefficient evaluated for Li^0 (a) and Li^+ (b) as a function of electron temperature

Figure 2 8 Radiative recombination rate coefficient evaluated for energy levels in Li^0 for (a) 2^2s, (b) 2^2p, (c) 3^2s and (d) 3^2p, as a function of electron temperature

To calculate the radiative recombination rate coefficient for the levels of Li⁰,
the exact photoionization cross-sections were used and are available from the
TOPBASE database, [45] The Milne relation, equation 1 80, was used to cal-
culate the radiative recombination cross-sections and these were then averaged
over a Maxwellian distribution to calculate the radiative recombination rate coef-
ficients
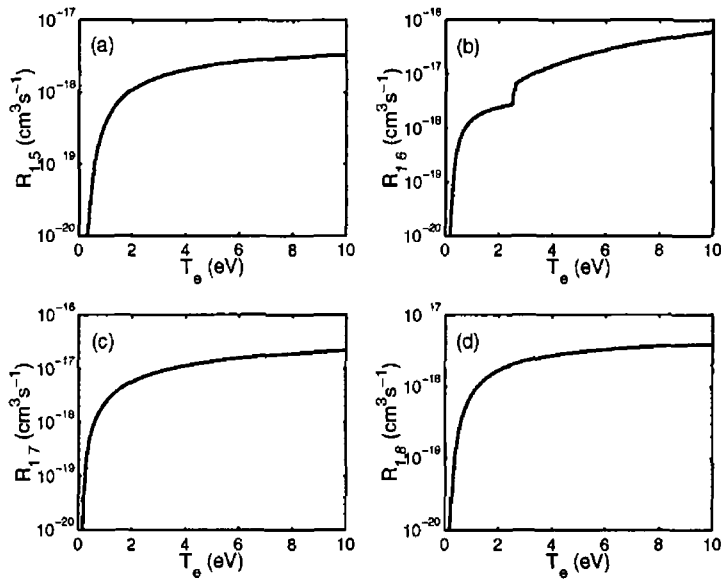
Figure 2 9 Radiative recombination rate coefficient evaluated for energy levels in Li⁰ for (a) 3^2d,
(b) 4^2s, (c) 4^2p and (d) 4^2d, as a function of electron temperature

2.3.3   Dielectronic Recombination

To calculate the total dielectronic rate coefficient, the sum over all of the electrons
in ion $\zeta + 1$ must be made In [57], all of the available dielectronic recombination
data was compiled and assessed Formulae to calculate this rate coefficient were
introduced with an estimated reliability of $\geq 50\%$

In [58] new and updated calculations were performed and a single formula for the calculation of the total dielectronic recombination rate coefficient was introduced for elements H to Ni This formula is written

$$\alpha_d = \frac{1}{T^{3/2}} \sum_{j=1}^{4} c_j exp \left(-\frac{E_t}{T} \right)$$ (2 12)

where E_t and T are in eV and c_t is in $cm^3 s^{-1}$ c_t and E_t are tabulated and are available in electronic form from [59]   The results yielded from this formula were found to be within 10% of previous calculations   Figure 2 10 shows the
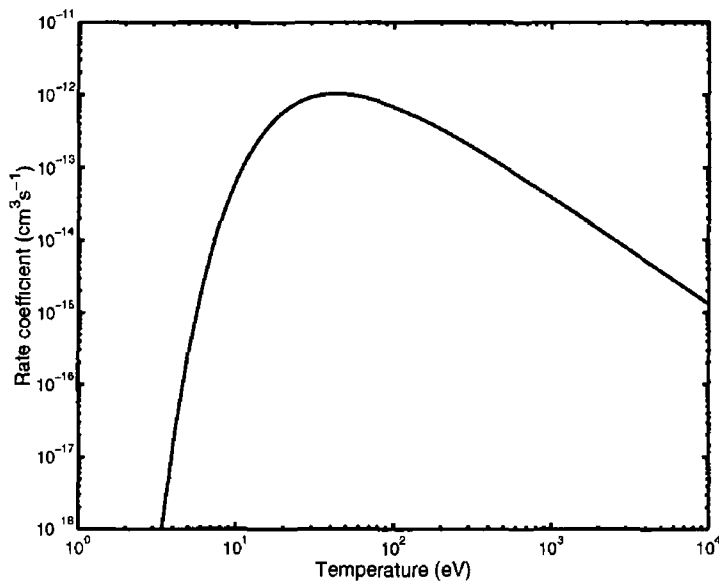
Figure 2 10   Dielectronic recombination rate coefficient to Li⁰ as a function of temperature

dielectronic rate coefficient calculated using the fitting formula, equation 2 12, for recombination to Li^0 In light of the high threshold, dielectronic recombination will never have a significant effect on the total two body rate coefficient in this work, since the temperatures never exceed a few eV in the expanding plume Hence, this coefficient has not been included in the calculations outlined in section 2 2 2

65

2.3.4 Excitation and Deexcitation Rate Coefficients

In [60], close coupling calculations were used to improve the quality of data for use in the calculation of the electron impact excitation cross-section for Li^0 The recommended cross-sections for the process were fitted to simple analytical expressions with the coefficients tabulated for the various transitions, which is given by

$$\sigma(E/eV)[cm^{-3}] = \frac{5\ 984 \times 10^{-16}}{E} \left[\frac{E - \Delta E}{E}\right]^{A_6}$$
$$\times \left[\sum_{j=1}^{4} \frac{A_j}{(E/\Delta E)^{j-1}} + A_5 ln\left(\frac{E}{\Delta E}\right)\right] \qquad (2\ 13)$$

where A_j are coefficients tabulated in [60] The calculations were performed for
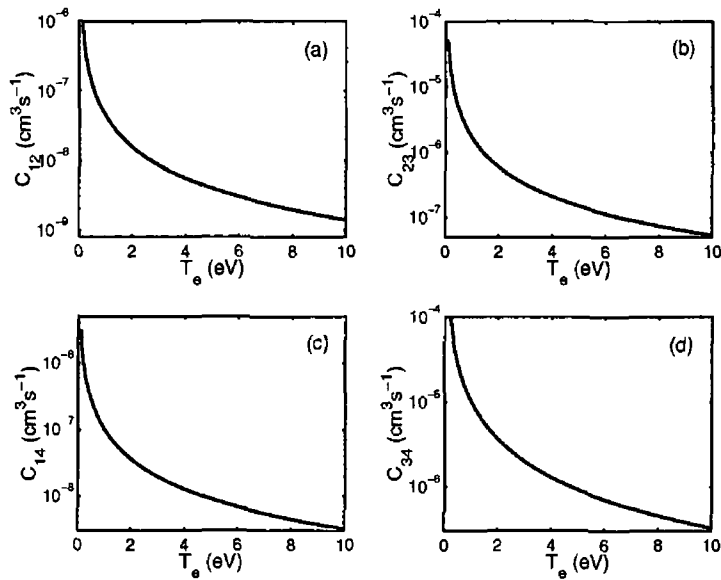
Figure 2 11 Electron impact excitation rate coefficient calculated using the fitting formula, equation 2 13 for the transitions (a) $2^2s \rightarrow 2^2p$, (b) $2^2p \rightarrow 3^2s$, (c) $2^2s \rightarrow 3^2p$ and (d) $3^2s \rightarrow 3^2p$, in Li^0 as a function of electron impact energy

impact energies from the excitation threshold up to $10keV$ In the $2s \rightarrow 2p$ case,

the calculations agree to within 10% of experimental values Larger errors existed in the 2s → 3d case with good agreement, in general, with experimentally measured cross-sections A review of the various methods for the electron impact excitation cross-section calculations showed excellent agreement between calculations based on equation 2 13 and other, more complex, calculations [61]

Figures 2 11 to 2 14 display the electron impact excitation rate coefficients for all of the transitions of interest, see table 2 2 2 These were calculated by averaging the electron impact excitation cross-section over a Maxwellian distribution The cross-sections were calculated using the method applied in [60] and outlined above All of the deexcitation rate coefficients were calculated using the principle of detailed balance
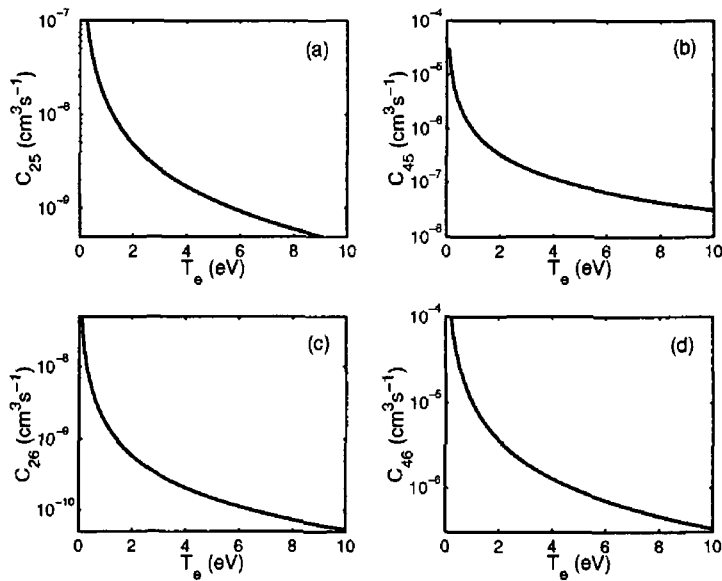
Figure 2 12 Same as figure 2 11 for the transitions (a) $2^2p \to 3^2d$, (b) $3^2p \to 3^2d$, (c) $2^2p \to 4^2s$ and (d) $3^2p \to 4^2s$
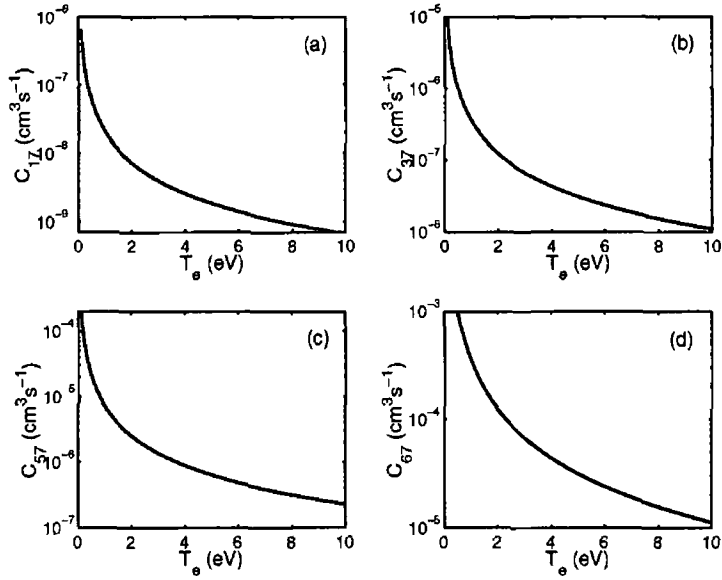
Figure 2 13 Same as figure 2 11 for the transitions (a) $2^2s \rightarrow 4^2p$, (b) $3^2s \rightarrow 4^2p$, (c) $3^2d \rightarrow 4^2p$ and (d) $4^2s \rightarrow 4^2p$
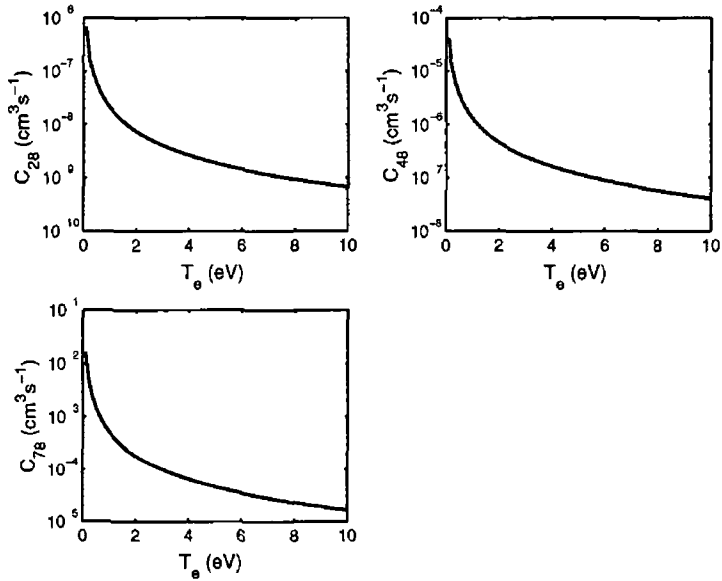
Figure 2 14 Same as figure 2 11 for the transitions (a) $2^2p \rightarrow 4^2d$, (b) $3^2p \rightarrow 4^2d$ and (c) $4^2p \rightarrow 4^2d$

68

2.3.5 Transition Probabilities and Oscillator Strengths

Transition probabilities, also known as the Einstein-A coefficients, play an important role in the distribution of population densities of bound energy levels They correspond to the rate of spontaneous decay of an atom or ion from an excited state into a lower state The values of the transition probabilities are used directly in the rate equations, see equation 1 33, where the number of transitions from the upper to lower state per second per cm^{-3} is

$$transitions(cm^{-3}s^{-1}) = -\frac{dN_j}{dt} = N_j A_{ji} \qquad (2\ 14)$$

where i and j correspond to the lower and upper levels, respectively

The oscillator strengths for their corresponding transitions are input parameters for the radiative transfer equation, see equation 1 89, and have a close relationship with the transition probability, see equation 1 90

For many transitions of interest, the energy levels may have multiple configurations When either the upper or lower level is split in this way, the relevant oscillator strength sum rules for the computation of the total transition probabilities and oscillator strengths must be employed These procedures are outlined by Cowan [39] and have been implemented in this work for all transitions included The full set of transitions used, with oscillator strength and transition probabilities are shown in table 2 2 2

With all of the available atomic data now in place and the population densities acquired, with space and time resolution, it is possible to calculate the emission and absorption coefficients in the plume With this achievement, the full radiative transfer equation may be evaluated along chords in the plasma plume In the following chapter, the full model will be employed with a full analysis of a lithium ablation plume expanding into vacuum

Chapter 3

Analysis and Discussion

In this chapter, the main results of this work are presented and discussed It begins with a discussion of the initial conditions used, keeping in mind that these are remaining within the PLD domain The chapter is split into three main parts, beginning with the initial conditions and ablation plume expansion This provides the input parameters to the atomic physics model leading, finally, to the radiation transport analysis

3.1 Plume Initiation and Expansion

3.1.1 Initial Conditions

When describing a plasma plume expanding into vacuum using hydrodynamics, or any other method, the importance of initial conditions cannot be overstated The fundamental process of laser ablation begins when a laser, operating at a particular wavelength, fluence and pulse duration, is focussed onto a small spot on the chosen target material In the following, the important initial conditions are outlined with a focus on the impact of their variation on the resultant expansion

dynamics

The experimental results used in the rest of this chapter were measured by Alan McKiernan at Dublin City University In the following, a brief account of the experimental conditions will be given A pulsed Nd-YAG laser, pulse duration 6 ns, equipped with the appropriate frequency-multiplying optics which generated the first four harmonics at the wavelengths of 1,064 nm, 532 nm, 355 nm and 266 nm, respectively, was used to create the plasma plume The laser light was focussed via a plano-convex converging lens normal to the surface of a pure (99 99%) lithium target in a vacuum chamber evacuated to a base pressure of 10^{-7} mbar or better The fluence on target was evaluated after detailed measurements of the unfocused laser power at the target position and the Gaussian spot size for various amounts of defocussing of the lens Digital frame photography was used to record the expansion of the luminous lithium ablation plume using a gated ICCD camera equipped with a zoom lens of variable aperture The exposure time of each frame was 3 ns The f-number and object distance were selected to ensure that all of the recorded light rays were paraxial The measured plume luminous edge and the plume's position of maximum intensity were recorded from ICCD photographs of the expanding plume

As outlined in section 1 3, the optical constants of the material, namely, the refractive index and absorption coefficient may be used to determine the absorbance of the material The absorbance refers to the fraction of the laser energy absorbed by the material at a given wavelength

As the wavelength of light incident on the material is varied, there may be a significant change in the efficiency of light absorption by the material The effect of wavelength variation on the material absorbance is shown in figure 3 1 for lithium The absorbance is quite high at lower wavelength, about 55% at 266 nm, drops dramatically until 500 nm, reaching about 10%, and continues dropping, but

much more gradually, as the wavelength is further increased and reaching about 5% at 1064 nm The effect of these variations in absorbance on the ablation depth, d_a is also apparent It decreases by an order of magnitude between a laser operating at 266 nm and 1064 nm for the range of fluences shown This, consequently, affects the amount of ablated material created during the pulse, and number of particles in the plume, indicating the strong dependence on laser wavelength of the initial plume formation, leading to the expansion
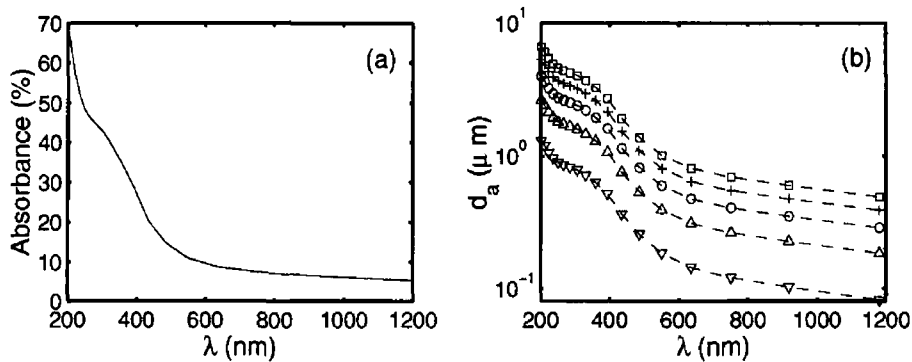
Figure 3 1   (a) The absorbance of a Li target as a function of wavelength, λ, and (b) the variation of ablation depth, d_a, as a function of wavelengths for fluences of 2 J cm^{-2} (– $\triangledown$ –), 4 J cm^{-2} (– $\triangle$ –), 6 J cm^{-2} (– $\bigcirc$ –), 8 J cm^{-2} (– + –) and 10 J cm^{-2} (–$\square$–)

To calculate the total number of particles in the plasma plume requires knowledge of the spot dimensions together with the ablation depth The spot size may be obtained experimentally With this information available, knowledge of the number of particles and, hence, total mass of the plume is possible To initialise the hydrodynamics model also requires an estimation of the initial plume height, X_0 This height does not correspond to the ablation depth, since the plume is not created instantaneously The laser strips off layers of the target providing energy to the vaporizing particles during the laser pulse By the end of the pulse, the initial layer evaporated will be displaced from the target as the final layer is va-

72

porized and the true plume dimension in the target normal direction, X_0, will be greater than the ablation depth This initial plume dimension may be estimated from [62]

$$X_0 = v_s \tau \tag{3 1}$$

where τ is the pulse duration and v_s is the sound speed, which is given by [48]

$$v_s = \sqrt{\frac{\gamma kT}{m}} \tag{3 2}$$

where γ, m, k and T are the ratio of specific heats, mass of one atom, Boltzmann's constant and temperature, respectively

The set of initial parameters required for the model is still incomplete The initial energy in the plume, provided by the laser, is still required The laser energy absorbed by the target material, is used to heat, melt and vaporize this material, with the remainder stored as internal energy and used to drive the plume expansion Therefore, one may not simply use the absorbed laser energy as the total energy available for plume expansion The total initial plume internal energy may be written

$$E = \frac{1}{\gamma - 1} NkT \tag{3 3}$$

so that the average energy per particle, ϵ, is given by

$$\epsilon = \frac{E}{N} \tag{3 4}$$

Equation 3 3 indicates the close correlation between the initial energy and temperature of the plume This initial temperature is the average initial plasma temperature and is used as the initial temperature in the isothermal self-similar solution so that the temperature at any time t is given by [17]

$$T(t) = T_0 \left(\frac{X_0 Y_0 Z_0}{X(t)Y(t)Z(t)} \right)^{\gamma - 1} \tag{3 5}$$

73

where T_0 is the initial temperature (same as T in equation 3 3) In the isentropic case, this initial temperature is not used, but, rather, the temperature distribution is obtained from the ideal gas equation, see equation 1 22 The initial average energy per particle, hence, average temperature, is used to calculate the initial plume height, X_0, in equation 3 2, leading to equation 3 1 for both models

In the following sections, the formalism outlined above will be implemented to initiate the lithium plume for direct comparison with experimental observations The full set of conditions employed for this comparative study is shown in table 3 1

3.1.2 Plume Dimensions

In this section, the results of the expansion phase will be analysed At this stage in the simulation, the initial parameters are available with the exception of the total energy available for the expansion This requires the adiabatic index and the initial energy per particle, see equation 3 4 The adiabatic index is assumed to remain constant throughout the expansion and has been assigned a value of 1 24 [48] in view of the increased number of degrees of freedom than just translational in plasma [17, 62] The energy per particle in the plasma plume varies, depending on the other initial conditions

To estimate ϵ, a trial and error procedure to analyse the various predictions of the expansion models compared to the experimental observations was applied A simultaneous "best-fit" procedure was applied comparing the experimentally observed plume luminous edge position and maximum luminosity, see section 3 1 1 to those predicted by the expansion models Both of the expansion models are then engaged and the value of ϵ that best predicts the experimental plume expansion is employed Figures 3 2 to 3 7 show examples of this procedure for the three cases of variable wavelength with constant laser spot radius, S_{1a}, S_{1b} and

74

label	wavelength	laser spot radius	height	ablation depth
	λ, nm	$Y_0, Z_0, \mu m$	$X_0, \mu m$	d_a, nm
S_{1a}	266	50	66	902
S_{1b}	532	50	43	413
S_{1c}	1064	50	56	303
S_2	1064	150	56	309
S_3	1064	280	43	315
S_4	1064	500	43	316
S_5	1064	1000	35	316

label	fluence	energy per particle	Initial temperature	number of atoms in plume
	F, Jcm^{-2}	ϵ, eV	T_0, eV	$\times 10^{14}$
S_{1a}	2 10	29 2	7	3 3
S_{1b}	4 20	12 5	3	1 5
S_{1c}	6 3	20 8	5	1 1
S_2	6 4	20 8	5	10 0
S_3	6 5	12 5	3	36 0
S_4	6 5	12 5	3	114 8
S_5	6 5	8 3	2	459 4

Table 3 1 Initial conditions used in this work for comparison to experiment

S_{1c} from table 3 1

Figures 3 2 to 3 4 show the predictions of the isothermal model, for various values of ϵ in comparison with experimental data acquired from broadband ICCD camera images of the expanding lithium plume in vacuum Although the fluence
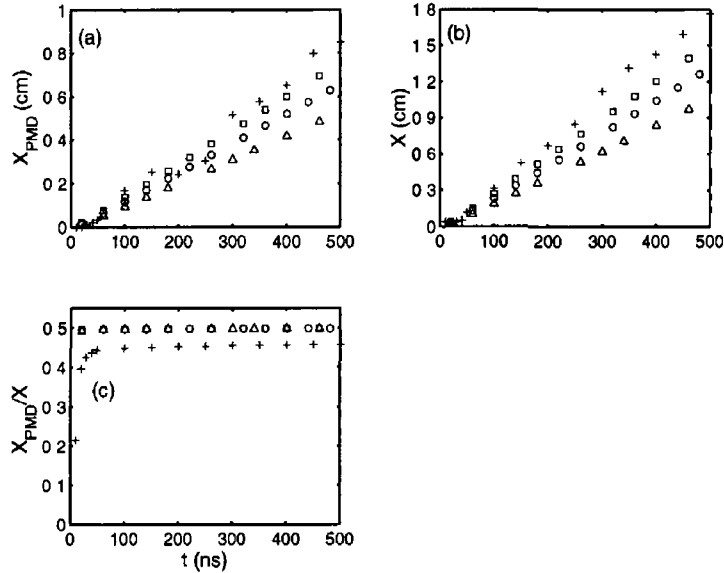
Figure 3 2   Predicted expansion dynamics of isothermal model for set of initial conditions S_{1a} at various values of ϵ compared to experiment $\epsilon=12\,5$ eV ($\triangle$), $\epsilon=20\,8$ eV (o), $\epsilon=29\,2$ eV ($\square$), experiment (+)   (a) Position of maximum density as a function of time   (b) Plume dimension along target normal axis as a function of time   (c) Ratio of position of maximum density to the plume edge along the target normal axis as a function of time

at 266 nm is lowest at $2\,1$ Jcm^{-2}, the best fit value of ϵ is highest, at $29\,2$ eV As the fluence is increased to $4\,1$ Jcm^{-2} at 532 nm, ϵ drops to $12\,5$ eV However, if the fluence increases further to $6\,3$ Jcm^{-2}, ϵ increases to $20\,8$ eV This is counter-intuitive behaviour, but under consideration of the initial conditions, the reason appears to become clear We discuss this point now

As the wavelength of the laser radiation increases, the inverse bremsstrahlung
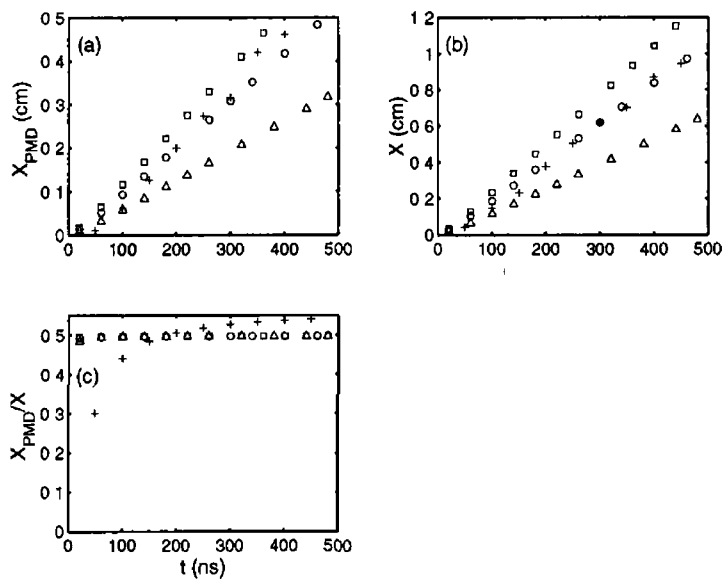
Figure 3 3 Same as figure 3 2 for set of initial conditions S_{1b} with $\epsilon=4\,2$ eV ($\triangle$), $\epsilon=12\,5$ eV (o), $\epsilon=20\,8$ eV ($\square$) and experiment (+)
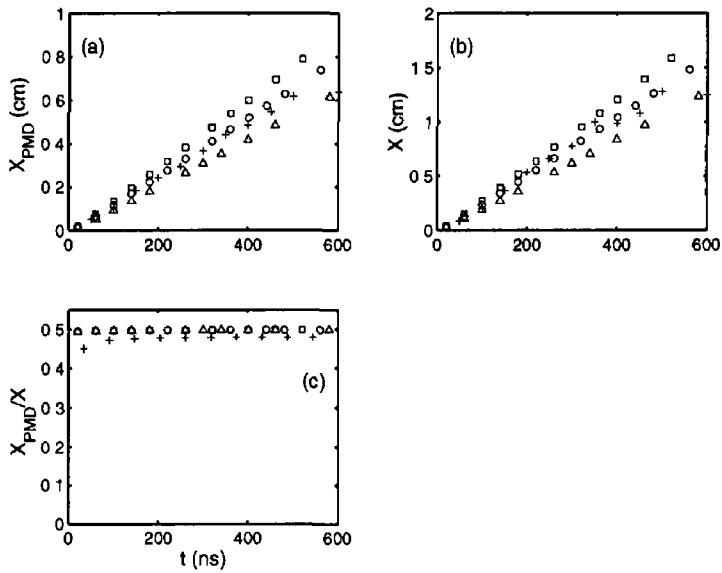
Figure 3 4 Same as figure 3 2 for set of initial conditions S_{1c} with $\epsilon=12\,5$ eV ($\triangle$), $\epsilon=20\,8$ eV (o), $\epsilon=29\,2$ eV ($\square$) and experiment (+)
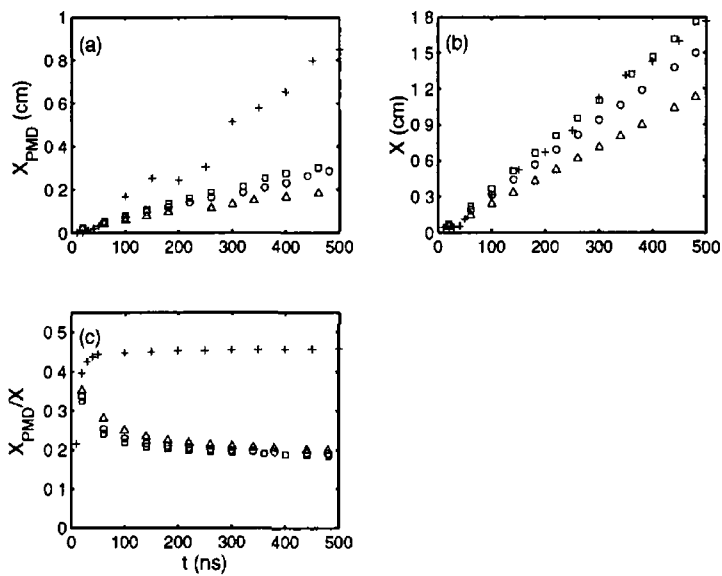
Figure 3 5 Same as figure 3 2 for isentropic model for set of initial conditions S_{1a} with $\epsilon=2$ 1 eV ($\triangle$), $\epsilon=4$ 2 eV (o), $\epsilon=6$ 3 eV ($\square$) and experiment (+)
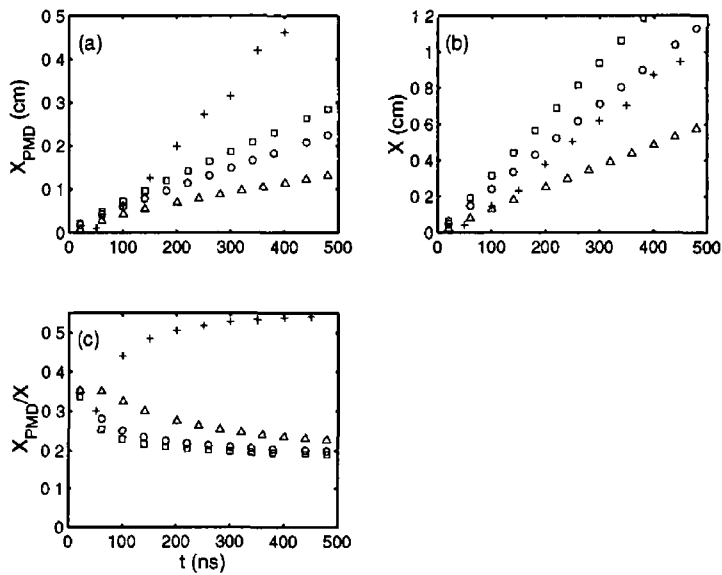
Figure 3 6 Same as figure 3 2 for isentropic model for set of initial conditions S_{1b} with $\epsilon=0$ 4 eV ($\triangle$), $\epsilon=2$ 1 eV (o), $\epsilon=4$ 2 eV ($\square$) and experiment (+)

78
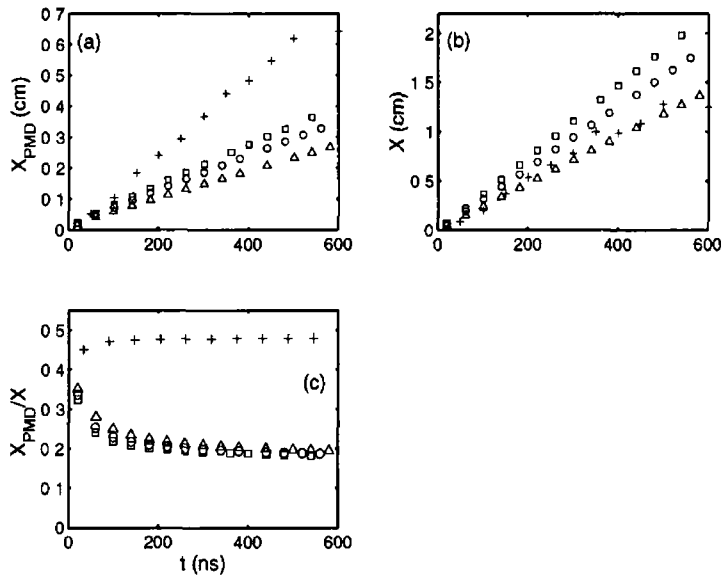
Figure 3 7   Same as figure 3 2 for isentropic model for set of initial conditions S_{1c} with $\epsilon=2$ 1 eV ($\triangle$), $\epsilon=4$ 2 eV (o), $\epsilon=6$ 3 eV ($\square$) and experiment (+)

(IB) absorption of the laser light by the plasma increases also, so that less energy reaches the target and the mass of ablated material decreases   Since the model in use does not include absorption of the laser light by the plasma, a smaller amount of laser energy goes into the plume creation   The effect of laser wavelength variation on ablated mass was carried out in [63]   These authors showed that the ablation rate rose steadily until reaching a peak at around 12 Jcm^{-2} for an alumina target ablated with a CO_2 laser   As the fluence is further increased, the absorption of the laser radiation by the plasma via IB becomes significant   In the case of an excimer laser, there was no observed peak, since the absorption of laser radiation in the plasma state is negligible at this short wavelength

In the case presented here, the fluence is low at the 266 nm wavelength so that no significant IB absorption by the plasma will occur   As the wavelength increases to 532 nm the absorption of laser radiation by the plasma will increase

79

and further again at 1064 nm However, as the fluence remains at 4 1 Jcm^{-2} value at 532 nm and increases to 6 3 Jcm^{-2} at 1064 nm, it is more likely that this ϵ variation may be attributed to the significantly higher target absorbance at 266 nm than in either the 532 nm or 1064 nm cases (see figure 3 1) At 266 nm the absorbance is high at around 55% and drops to about 10% at 532 nm The effect of this high decrease in absorption is mirrored both in the ablation depth and the total energy in the plume (see table 3 1) However, this trend does not continue as the wavelength is increased The situation is reversed when the 532 nm case is compared to the 1064 nm case in the sense that the wavelength increases but the best fit ϵ is lower in the case of higher absorbance Since the absorbance differs by only 5% between these sets of initial conditions, the effect of increased absorbance at 532 nm appears to be too low to counter the effect of the higher fluence and higher plasma absorption at 1064 nm

Figures 3 5 to 3 7 show the expansion predictions for different values of ϵ in the isentropic case Here, it is clear that for the values of ϵ that most accurately predict the plume edge position, the position of maximum density, X_{PMD}, is not accurately predicted This is in contrast to the isothermal model, where there is a close correlation between the plume dimension and position of maximum density for a particular value of ϵ

There is also a marked difference between the predicted 'best-fit' ϵ of the two expansion models For example, in the 1064 nm case, S_{1c}, the isentropic model accurately predicts X for ϵ of 2 1 eV However, of the three cases shown, this is the least accurate prediction of the position of maximum density Also, with the plume expansion velocities of the order of 10^6 cms^{-1}, the plume temperature would drop very rapidly to values below 0 2 eV in tens of ns Hence, an energy per particle of 2 1 eV would be too low in this case The 'best-fit' ϵ for the isothermal model in the S_{1c} case is 20 8 eV, and appears to be a much more realistic value,

since typical initial plasma temperatures in these conditions are a few eV From these considerations, we conclude that the isothermal model is a better model for the analysis of plasma plume expansions for the sets of initial conditions at the smallest spot size in our experiments

Figures 3 8 to 3 11 show the best fit descriptions from both models for the four cases of increased spot size, S_{2-5}, all ablated at a laser wavelength of 1064 nm As
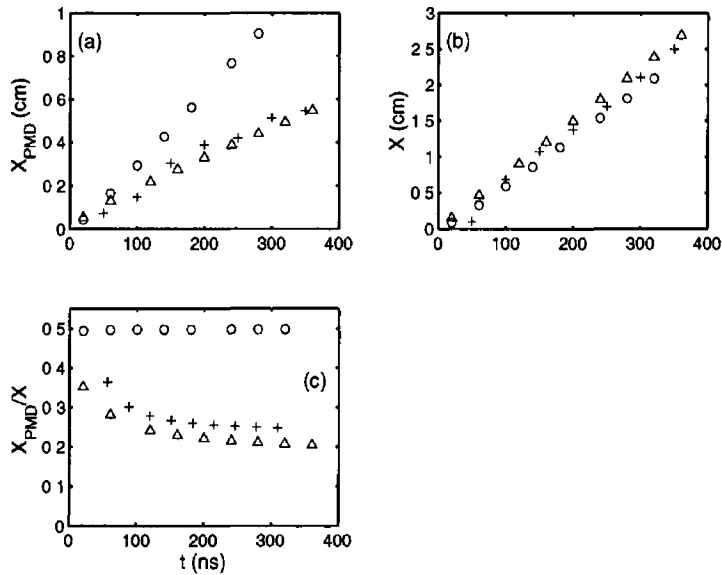

Figure 3 8 Predicted expansion dynamics for set of initial conditions S 2 compared to experiment at 'best-fit' values of ϵ for both self-similar models Isothermal (ϵ=125 0 eV (o)), Isentropic (ϵ=20 8 eV ($\triangle$)), experiment (+) (a) Position of maximum density as a function of time (b) Plume dimension along target normal axis as a function of time (c) Ratio of position of maximum density to the plume edge along the target normal axis as a function of time

the spot size is increased, keeping the fluence, 6 5 Jcm^{-2}, and laser wavelength, 1064 nm, constant, the isentropic solution begins to describe the dynamics more accurately The position of maximum density, X_{PMD}, is overestimated by the isothermal solution, see, in particular, figures 3 8 and 3 9

81
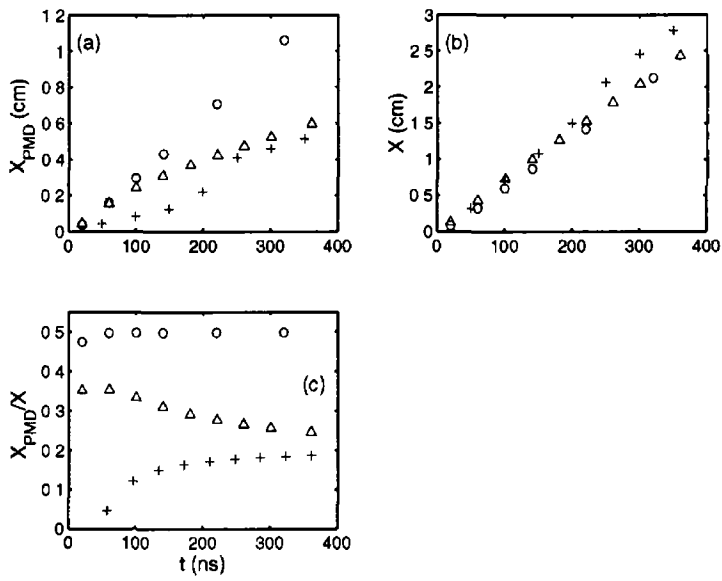
Figure 3 9   Same as figure 3 8 for set of initial conditions S$_3$ Isothermal (ϵ=104 2 eV (o)), Isentropic (ϵ=12 5 eV (Δ)), experiment (+)
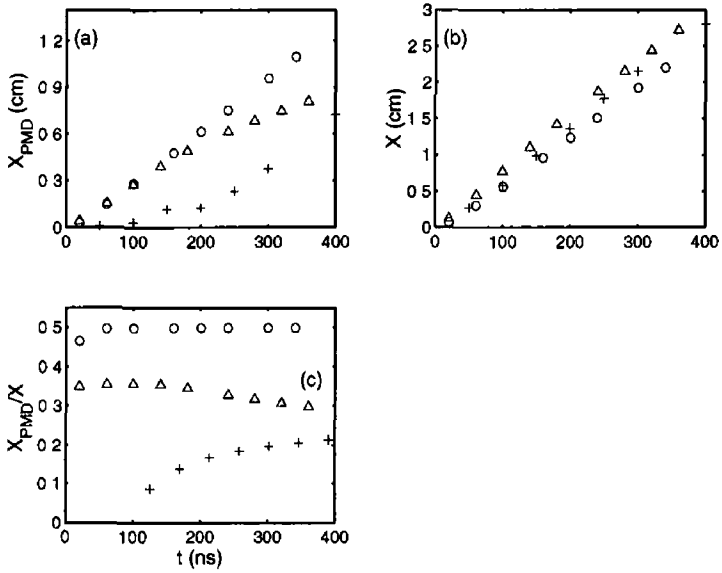
Figure 3 10   Same as figure 3 8 for set of initial conditions S$_4$ Isothermal (ϵ=83 3 eV (o)), Isentropic (ϵ=12 5 eV (Δ)), experiment (+)
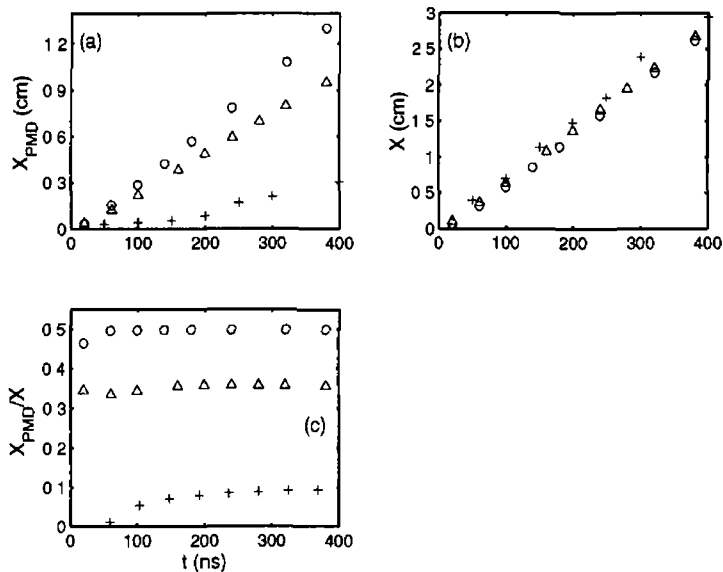
82

Figure 3 11   Same as figure 3 8 for set of initial conditions S_5 Isothermal (ϵ=83 3 eV (o)), Isentropic (ϵ=8 3 eV ($\triangle$)), experiment (+)

In the S_1 (X_0=50 μm) case, the plume radius to plume height ratio is close to unity   As the total plume energy is distributed to a small volume, one can readily assume that equilibrium is readily obtained [64], and the temperature across the plume is roughly equal   As this ratio increases the pressure along the target normal direction will increase   This is due to a heightened pressure in the direction of smaller dimension, [65]   The plume volume also increases since the ablation depth remains constant while the target spot radius increases   Hence, the likelihood of temperature gradients increase in the initial plume and, thus, an isentropic solution may become more appropriate to analyse expansion dynamics

In figures 3 2 to 3 11, the ratio of the position of maximum density, X_{PMD} to the plume leading edge X has been displayed   It is clear from these figures that in all of the cases of smallest spot size, S_{1a-1c}, that the plume breaks almost completely free from the target rapidly   However, as the spot size is increased and

83

the fluence kept approximately constant, this ratio diminishes rapidly until in the S_5 case where the position of maximum density remains close to the target surface and only moves to a maximum position of 20% of the leading edge distance from target This may be explained through the analysis of the surface pressure applied to the target by the expanding plume, see section 1 4 3 In the sets of initial conditions S_{2-5}, the initial number of particles in the plume will increase as the spot size increases, see table 3 1, with the ablation depth remaining approximately constant, so that the total plume mass increases However, the resultant affect on the plume dynamics will be diminished since the value of the spot size increases with the increased mass Hence, the ratio of pressure exerted onto the target to the total mass of the plume may not vary appreciably, even with increased spot size Also, the velocity of the leading edge continues to increase with increased spot size, thus, reducing the ratio of X_{PMD}/X

Figure 3 12 shows the plasma plume pressure exerted on the centre of the target as a function of time for the 'best-fit' initial energy per particle in each case of initial conditions S_{1a-1c} and S_{2-5}, from table 3 1 In all three cases of S_1, the pressure exerted on the target rises during the pulse to a peak value at the end of the pulse, t =6 ns This rise is due to increase in particles ejected from the target surface during the pulse, thus increasing the pressure The injection of particles in the plume during the pulse is included as a factor equal to t/τ_p multiplying the density profile, see equation 1 25 Immediately after the pulse the rate of particle ejection diminishes rapidly and, with the plasma expanding, the surface pressure quickly drops and the velocity of X_{PMD} will approach a constant value

The rise of the surface pressure is not seen in the isentropic model since there is no account made for the rate of change of particle number in the plume during the laser pulse (see equation 1 20) Hence, the initial pressure is greatest at the earliest time and drops very rapidly
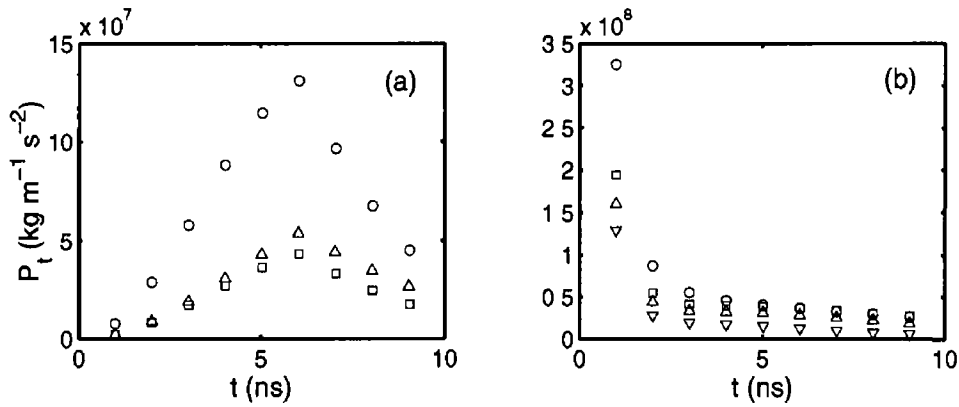
Figure 3 12   Predicted pressure exerted on centre of target surface as a function of time for sets of initial conditions initial conditions using isothermal solution ((a) $S_{1a}(\circ)$, $S_{1b}(\triangle)$ and $S_{1c}(\square)$) and isentropic solution ((b) $S_2(\triangledown)$, $S_3(\triangle)$, $S_4(\square)$ and $S_5(\circ)$) for best-fit energy per particle

As discussed in section 2 1 1, Chen et al [55], using the idea of a dynamic source, calculated surface pressures of the order of 10^7 Pa for a silicon target for typical fluences of a few Jcm^{-2}, pulse duration of 6 ns and laser spot of 1 mm radius   These surface pressures are of the same order as those calculated in the present work   The rise of surface pressure during the pulse and drop after the pulse was also observed by these authors and support the idea that a model incorporating an initial isothermal expansion during the laser pulse followed by an adiabatic expansion, as in [17], may be a more appropriate means of modeling plasma plume expansion   However, the appropriate self-similar solution for the adiabatic expansion after the pulse may be isothermal or isentropic depending on the initial conditions present, as we have just shown

3.2 Validity of Equilibrium Models

In this section, the validity criteria imposed on the current model will be analysed. Since the collisional radiative model employed in this work is assumed to be in steady state, the conditions for its existence will be analysed in the plasma conditions of interest. The effect of the radiation escape factors will be displayed. A simplified collisional radiative approach was introduced in section 1 5 2. The validity of this approach will be considered as well as validity of the LTE and Corona (CE) approaches in the plasma conditions of interest.

3.2.1 Steady State Validity

To consider the applicability of steady state conditions requires the identification of the most frequent collisional process. The rate of this process averaged over the velocity distribution of the electrons and multiplied by their number density provides the frequency of collisions of this type in a medium. Hence, the time between collisions, τ_{coll}, is the inverse of this frequency, see equation 1 62.

To achieve steady state conditions requires that τ_{coll} is much smaller than the characteristic time, τ_{char}, time it takes for the plasma temperature or density to change appreciably. Recalling equation 1 63, the condition for steady state is written

$$10\tau_{coll} < \tau_{char} \tag{3 6}$$

If we define a new variable $\phi_{t\zeta}$, such that

$$\phi_{t\zeta} = \frac{\tau_{char}}{\tau_{coll}} \tag{3 7}$$

where ζ is temperature, T, or electron density, n_e, steady state conditions require that

$$\phi_{t\zeta} > 10 \tag{3 8}$$

86

For local thermodynamic equilibrium conditions to exist in the plume requires the plasma to be locally uniform also For this criterion, τ_{coll} in equation 3 6 is replaced by the mean free path of the most frequent collision λ_{mfp}, see equation 1 61, and the characteristic time is replaced by the characteristic length λ_l for both electron density, n_e, and temperature, T, so that the plume may be considered locally homogeneous when

$$10\lambda_{mfp} < \lambda_l \qquad (3\ 9)$$

Again, we define a new variable $\phi_{l\zeta}$ such that

$$\phi_{l\zeta} = \frac{\lambda_l}{\lambda_{mfp}} \qquad (3\ 10)$$

so that sufficient local homogeneity is present if

$$\phi_{l\zeta} > 10 \qquad (3\ 11)$$

where ζ corresponds to temperature, T, or electron density, n_e

Figures 3 13-3 19 show the steady state and local homogeneity criteria for the full set of initial conditions using the 'best-fit' energy per particle to the expansion dynamics, see table 3 1 These criteria are shown as colour contour plots as a function of position along target normal and time The values of log $\phi_{t\zeta}$ and log $\phi_{l\zeta}$ vary as a function of colour as indicated on the colourbar alongside each axis

In figures 3 13-3 15, the characteristic length for temperature is excluded since these cases correspond to the isothermal self-similar solution In the isentropic cases, the spatial temperature profile allowed the computation of these values All of these figures indicate steady state and local homogeneity remaining valid assumptions throughout the plume region where $log\ \phi > 1$ For the remainder of this work, the regions where these assumptions remain valid are the regions where the atomic kinetics of the plasma is calculated
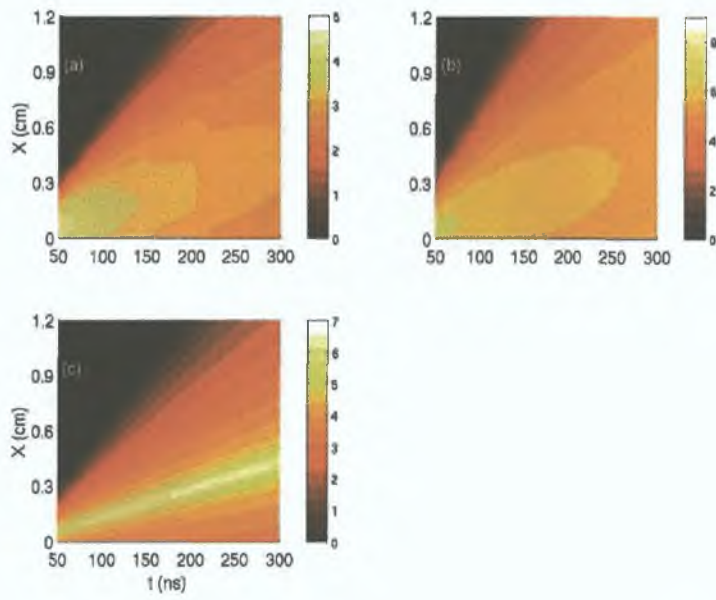
Figure 3.13: Value of (a) $|log\,\phi_{tn_e}|$, (b) $|log\,\phi_{tT}|$ and (c) $|log\,\phi_{lN}|$ in colour as a function of time and position along target normal axis for set of initial conditions S_{1a}.
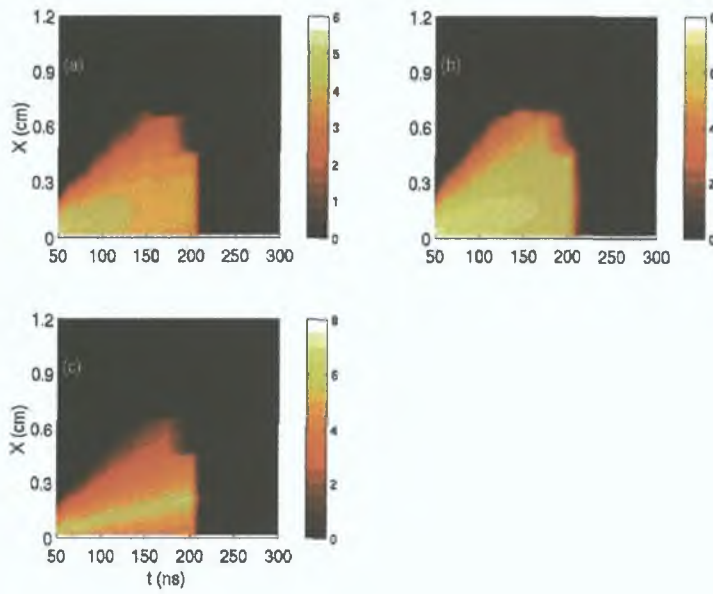

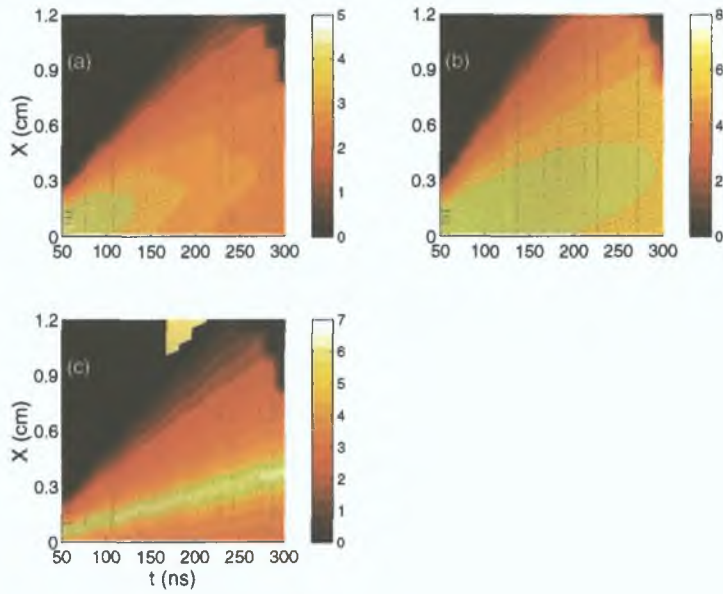Figure 3.14: Same as figure 3.13 for set of initial conditions S_{1b}.

88

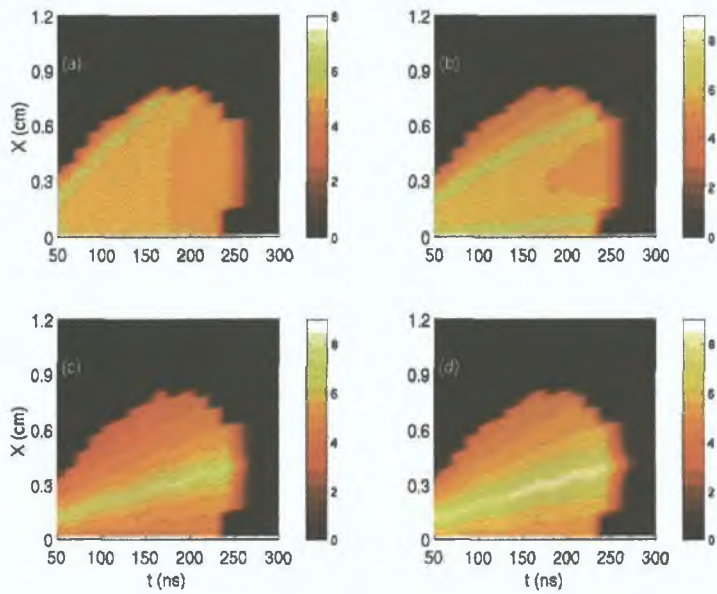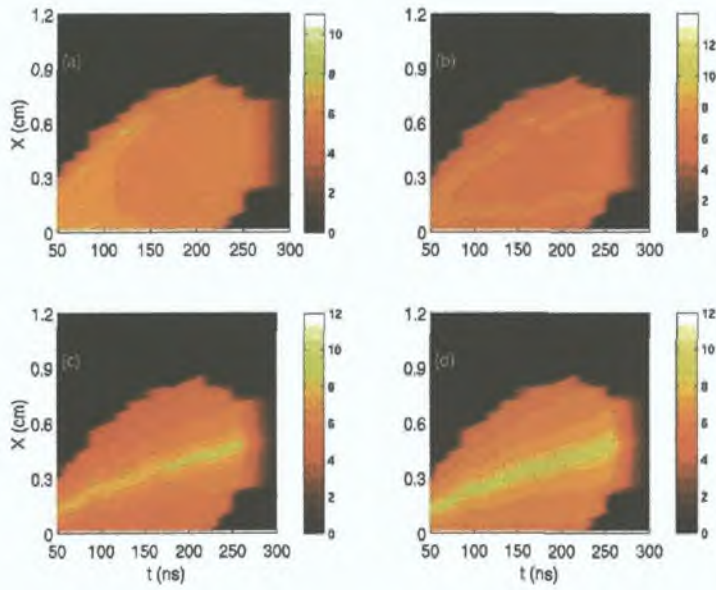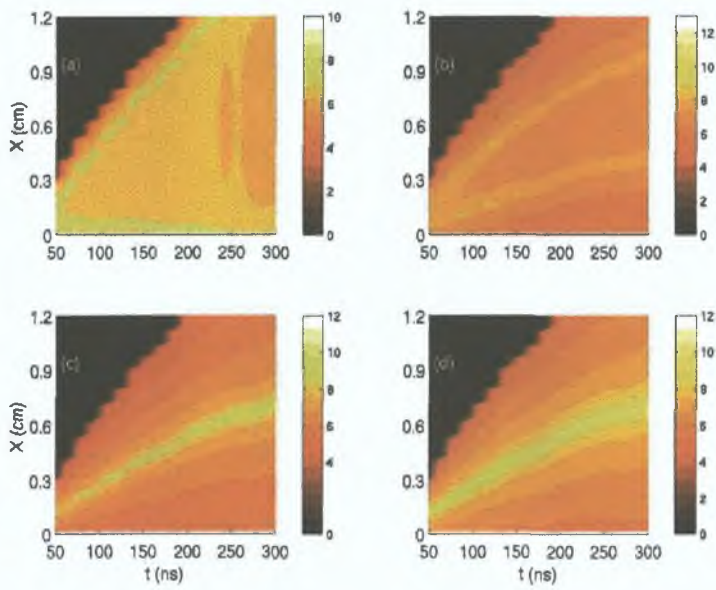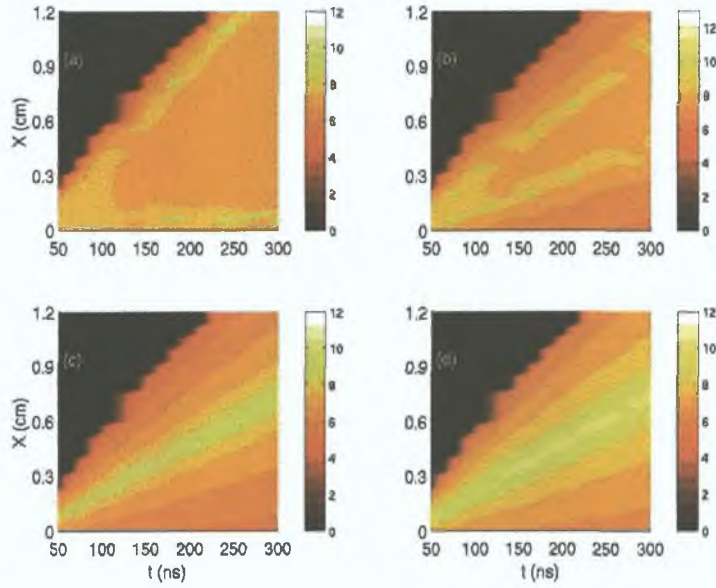Figure 3.15: Same as figure 3.13 for set of initial conditions S_{1c}.

Figure 3.16: Value of (a) $|log\,\phi_{tn_e}|$, (b) $|log\,\phi_{tT}|$, (c) $|log\,\phi_{lN}|$ and (d) $|log\,\phi_{lT}|$ in colour as a function of time and position along target normal axis for set of initial conditions S_2.

89

Figure 3.17: Same as figure 3.16 for set of initial conditions S_3.

Figure 3.18: Same as figure 3.16 for set of initial conditions S_4.

Figure 3.19: Same as figure 3.16 for set of initial conditions S_5.

3.2.2 Validity of Simplified Collisional Radiative Model

In chapter 1 a simplified Collisional Radiative model was introduced, which reduced the rate equation so that certain processes were neglected. This simplified CR model was shown to be appropriate when considered for lithiumlike ions for $n_e > \approx 10^{12} \text{cm}^{-3}$ [27]. We recall the criterion for the applicability of this model

$$N_i \sum_{j<i} A(i,j) >> \sum_{j>i} N_j A(j,i).$$

Introducing a variable, λ, such that

$$\lambda = \frac{\sum_{j>i} N_j A(j,i)}{N_i \sum_{j<i} A(i,j)} \tag{3.12}$$

then this simplified model is applicable for $10\lambda < 1$.

Figure 3.20 shows 10λ evaluated as a function of temperature for the levels 2^2p, 3^2s, 3^2p and 3^2d for the range of electron densities relevant to our conditions.

91

It is clear from this figure, that the criterion outlined is never valid for any electron density in this range or temperatures less than 10 eV, since the value of 10λ remains below 1 for the full range of densities and temperatures shown. Hence, the simplified CRSS approach of [26] is inappropriate to describe a laser ablation plume of lithium in the specified conditions. We note here that Gordillo-Vasquez [66] assumed validity of the simplified CRSS model for electron densities above 10^{12} cm^{-3}, in the case of a laser ablation plume of lithium niobate.
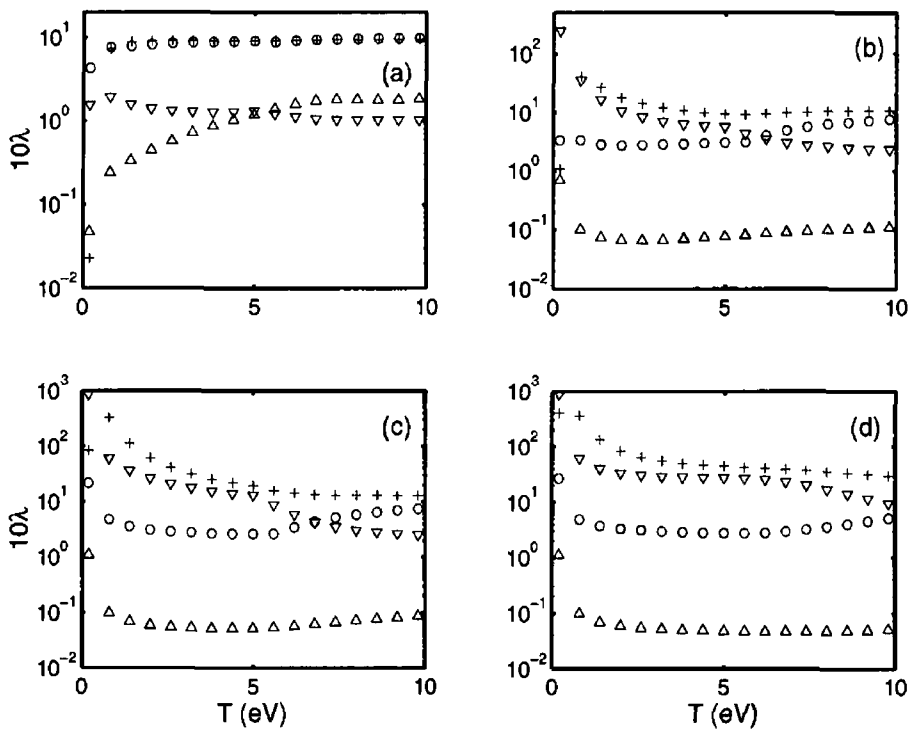
Figure 3 20 Showing the validity of the simplified CRSS model, from equation 3 12, evaluated as a function of temperatures for electron densities (a) 10^{12} cm^{-3} (b) 10^{14} cm^{-3}, (c) 10^{16} cm^{-3} and (d) 10^{18} cm^{-3} and energy levels 2^2p (+), 3^2s (o), 3^2p ($\triangledown$) and 3^2d ($\triangle$)

3.2.3 LTE Validity

Figure 3 21 shows the minimum electron density necessary for the realisation of complete LTE according to the criterion of equation 1 58 for lithium neutral Since the cross-section for the electron deexcitation of 2^2p level in neutral lithium peaks at the transition energy, 1 8485 eV [31], the electron density required for complete LTE will be minimum around this temperature value If the temperature increases, the majority of particles will become ionized and the ground state heavily depopulated so that a higher density of particles and, hence, electron density will be required for complete LTE validity The electron density required using the approximate formula 1 59 varies continuously in proportion to the square root of the temperature so that as T increases, so does the value of n_e required for complete LTE This means that the detail available from the cross-section variation with temperature is missing from the approximation formula and causes the underesimation of the n_e requirement for LTE, particularly at temperatures below the upper energy level of the resonance transition

Figure 3 22 shows the time domain of LTE existence in the full plume over the full set of initial conditions from table 3 1 for a variety of initial values of ϵ The isothermal model is used for the S_1 case while the isentropic model is used for S_{2-5} (see earlier discussion) The longest period for LTE applicability is predicted in the S_5 case Since the initial spotsize is largest here and the ablation depth varies insignificantly over S_{1-5}, this case predicts the highest amount of ablated material and, hence, greatest plume mass and density It is apparent that if the initial energy per particle is increased, a longer period of LTE applicability is not necessarily implied The thermal energy drives the expansion and is directly linked to the expansion velocity so that, if the initial temperature increases, the rate of expansion is higher and, consequently, the density begins to drop at a higher rate Therefore, the density will drop below the value necessary for LTE
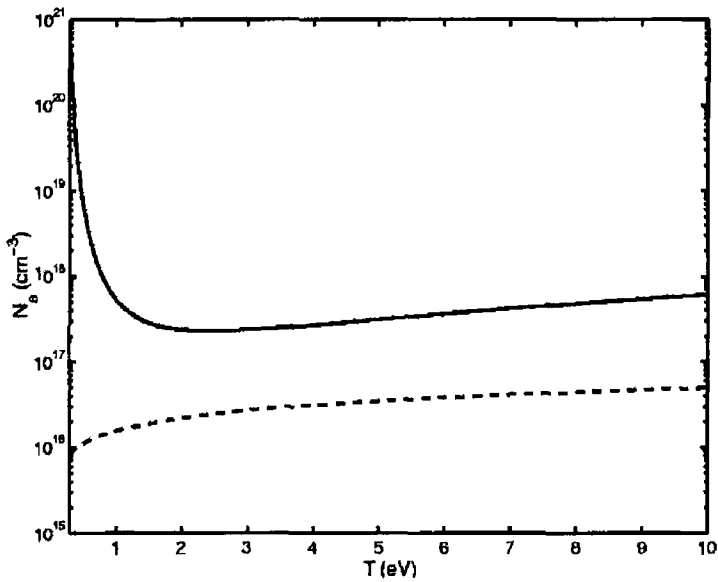
93

Figure 3 21   Calculation of n_e required for complete LTE of Li^0 using equation 1 58 using the deexcitation rate coefficient for the resonance transition in lithium neutral (–) and the hydrogenic approximation formula from [34] (– –) in the temperature range for PLD plasma
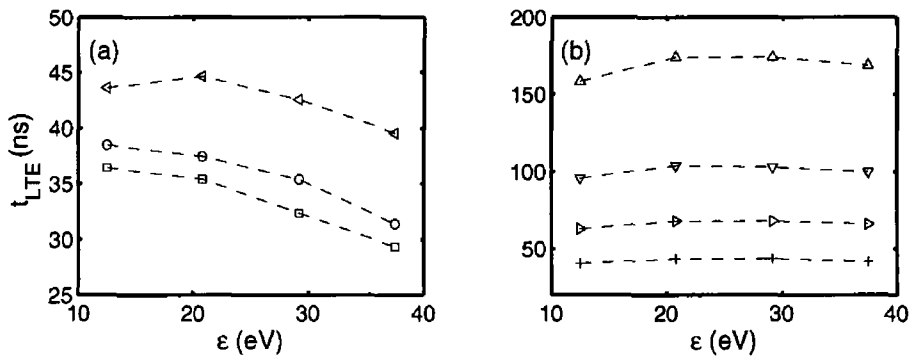

Figure 3 22   Time of LTE validity in plume for all sets of initial conditions from table 3 1 for a variety of initial energies per particle, ϵ, in each case   (a)   Isothermal model used for S_{1a-1c} with S_{1a} (– ◁ –), S_{1b} (– ○ –) and S_{1c} (–□–) and (b)   isentropic model used for S_{2-5}, S_2 (– + –), S_3 (– ▷ –), S_4 (– ▽ –) and S_5 (– △ –)
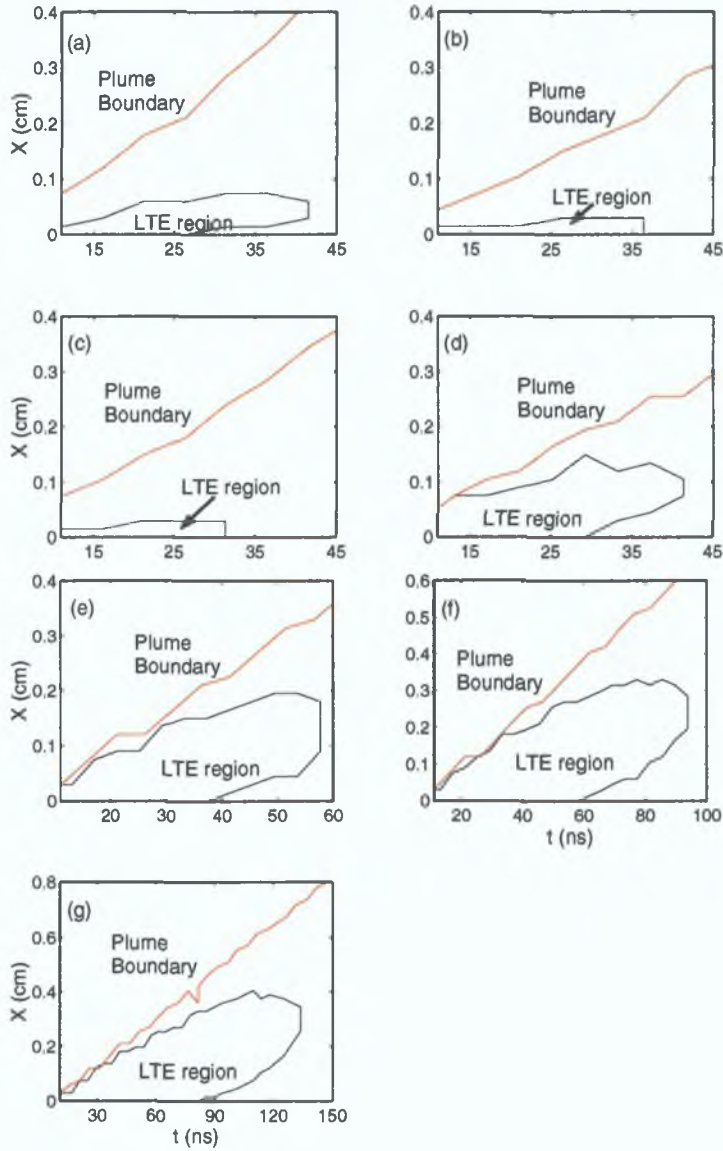
Figure 3.23: *Plume edge position compared with LTE domain along the target normal as a function of time for the full set of initial conditions from table 3.1 as a function of time. (a)* S_{1a}, *(b)* S_{1b}, *(c)* S_{1c}, *(d)* S_2, *(e)* S_3, *(f)* S_4 *and (g)* S_5

faster as the temperature is increased above about 7 eV in this case This shows that complete LTE, as a model for the plasma, is inapplicable to Li laser ablation plumes produced in conditions typical of PLD, except at very early times Even at these early times, LTE may only apply to portions of the plume and not to its entirety Figure 3 23 shows the plume edge position along the target normal compared to those of LTE validity It is clear that LTE may only be valid to portions of the plume and to early times Hence, it is only in very limited circumstances that LTE may be assumed in lithium plumes within the range of conditions used here and that, more generally, regions of LTE validity should be evaluated before this assumption is used

3.2.4   CE Validity

At the lower electron density range, collisional radiative models assuming detailed balance may not hold In these conditions, it is radiative processes that dominate deexcitation processes and in the coronal model the deexcitation processes balance the collisional excitation processes, see section 1 5 5 Figure 3 24 shows the value of N_e, below which, the coronal model may be applied according to equation 1 66 in Li^0 and Li^+ There is no explicit formula to define a validity criterion for the use of CE in the calculation of excited state densities [30]
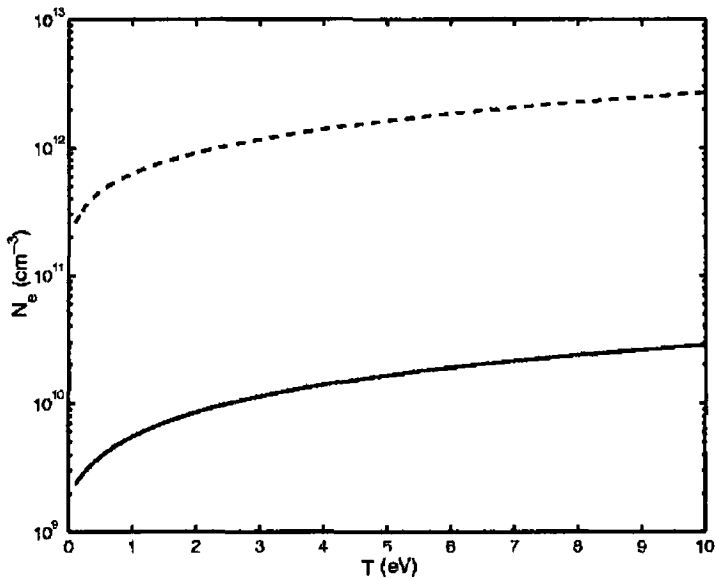
$N_e \ (cm^{-3})$

$T \ (eV)$

Figure 3 24   Calculation of upper limit for N_e required for Corona Equilibrium, using equation
1 66 for Li^0 (–) and Li^+ (– –), in the temperature range for PLD plasma

3.3   Electron and Ion Density

The electron, ion and neutral densities have been calculated as a function of space
and time using the method as indicated in chapter 2 Figures 3 25-3 31 compare
measured relative intensity contours from ICCD images with calculated electron
densities n_e, temperature T and ionization fraction I_f, respectively, along the tar-
get normal, $y, z = 0$, as a function of time   These plots are displayed as false
colour maps They are all plotted for the 'best fit' energy per particle obtained
from the hydrodynamics (see section 3 1 2)

The temperature contours for the S_{1a}, S_{1b} and S_{1c} cases all show no spatial
profile as a consequence of the isothermal self-similar solution The maximum
temperature observed in the S_{1a} case was about 2 eV early in the expansion and

dropping rapidly to a value of about 0.25 eV by 300 ns. This is in contrast with the S_{1b} case, where the temperature and density drop much more rapidly. This is reflected in the experimental colour maps also and is due to the initial condition differences in the two cases with regard to laser wavelength and fluence, see section 3.1.2.
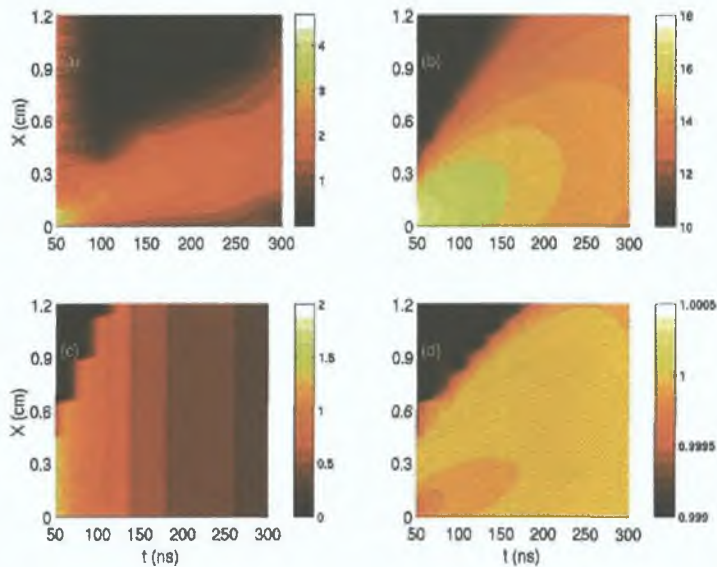

Figure 3.25: Value of (a) log of counts from experimental ICCD image, (b) $log\, n_e$ (cm^{-3}), (c) T_e (eV) and (d) I_f in colour as a function of time and position along target normal axis for set of initial conditions S_{1a}.

For the four cases of increased spot size, S_2-S_5, the effect of a spatial temperature profile becomes apparent. In this case the temperature drops as the plume edge is approached causing the truncation of the density profile much earlier than in the isothermal case, where the temperature is uniform and the plume dimensions can, theoretically, extend to infinity.

The ionization fraction in the plume is also shown in the same way as the other contours here. It is clear that the plume ionization fraction remains high for all sets
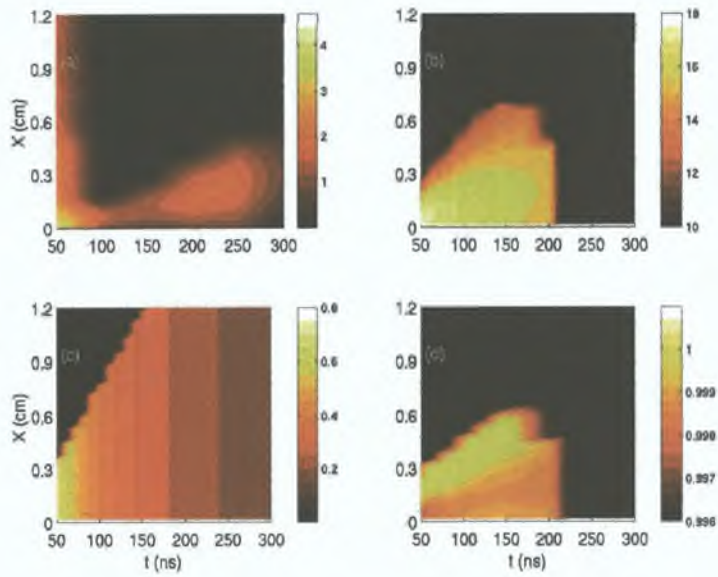
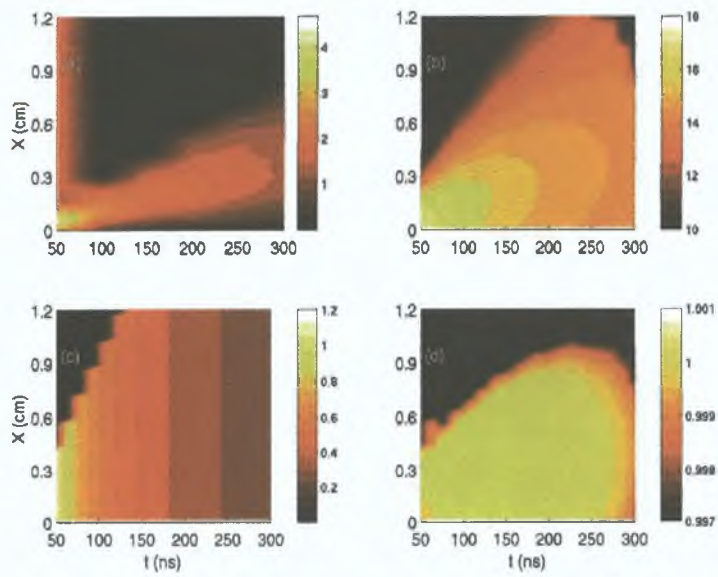Figure 3.26: Same as figure 3.25 for set of initial conditions S_{1b}.

Figure 3.27: Same as figure 3.25 for set of initial conditions S_{1c}.

99

of conditions shown and drops abruptly as the plume edge is approached. While it is not clear from these figures how the ion population is dispersed among Li^+ and Li^{2+}, it was found that, for all of the conditions shown here, no appreciable Li^{2+} population density was ever present. This is not surprising, since the ionization energy of Li^0 is 5.38 eV, but 75.64 eV for Li^+.
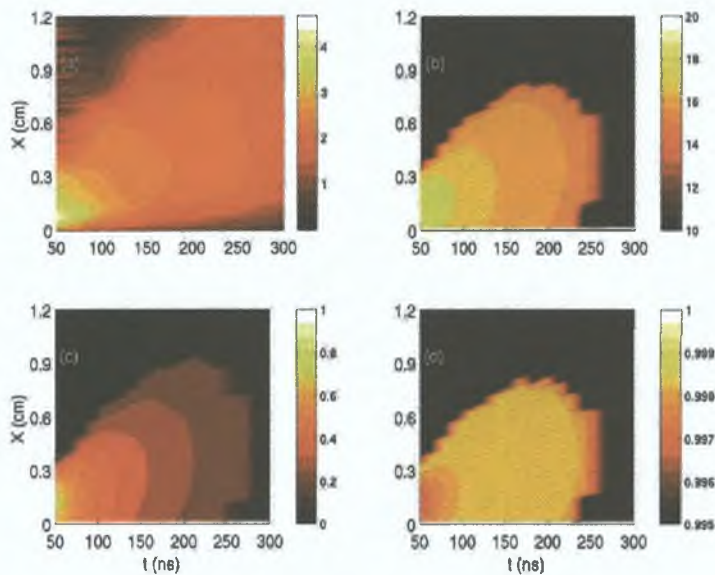

Figure 3.28: Same as figure 3.25 using isentropic model for set of initial conditions S_2.

In the following section, experimental spectra will be compared with synthetic spectra obtained using the energy level populations now available with the solution to the rate equations for Li^0, see section 2.2.2.
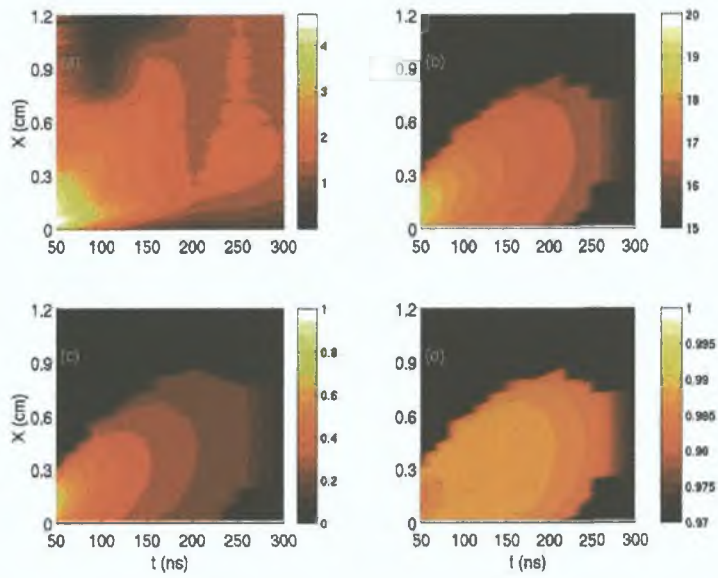
Figure 3.29: Same as figure 3.25 using isentropic model for set of initial conditions S_3.
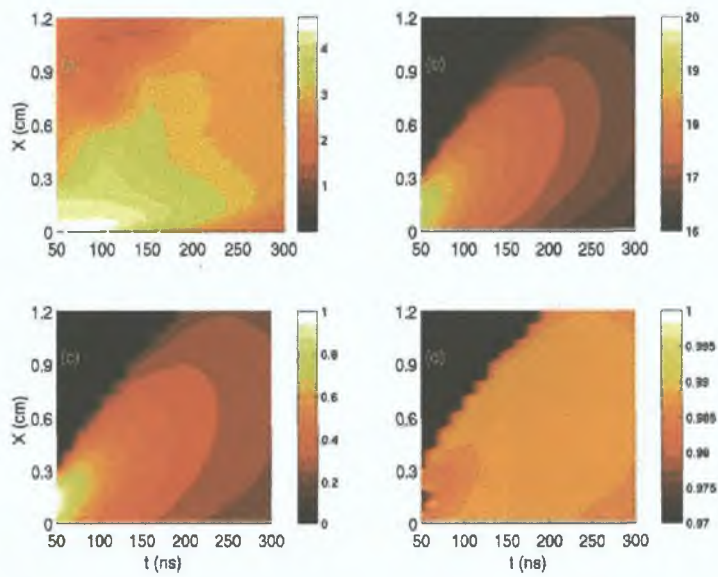

Figure 3.30: Same as figure 3.25 using isentropic model for set of initial conditions S_4
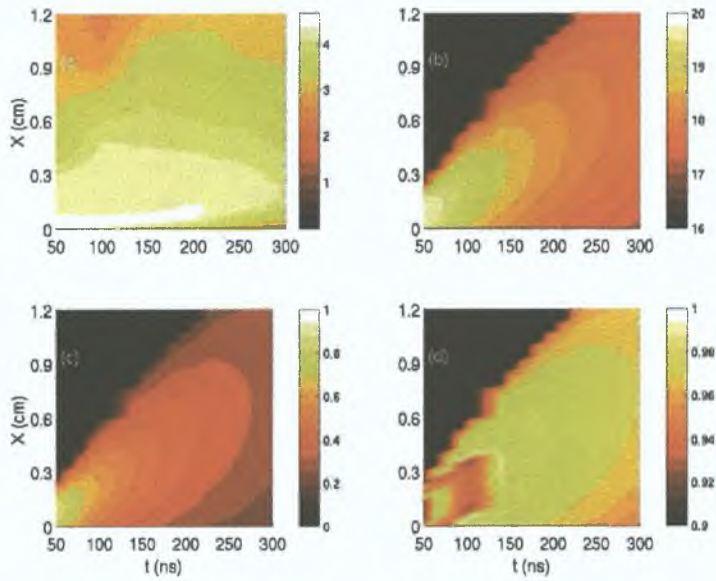
101

Figure 3.31: Same as figure 3.25 using isentropic model for set of initial conditions S_5

3.4 Radiative Properties

3.4.1 General Aspects of Radiative Transfer

In this section, the general aspects outlining the radiative transfer in the plasma will be described. The radiative transfer equation (RTE), see equation 1.102, has been solved as a post-processor to the hydrodynamics and atomic kinetics of the expanding plume.

In all of the spectra shown, the RTE has been solved one-dimensionally through the target normal axis across the plume diameter, whose magnitude is defined by the hydrodynamics, parallel to the target surface. The full emission and absorption coefficients including continuum and line radiation were employed in the RTE. Equations 1.81 and 1.82 were used to calculate the free-free coefficients for emission and absorption, respectively. Equations 1.88 and 1.84 was emloyed in

102

the case of the free-bound radiation for the emission and absorption coefficients, respectively Exact photoionization cross-sections were used and are available from the TOPBASE database, [67] In the case of the bound-bound emission, Voigt profiles were used, with the Stark parameters for the line width taken from [45]

In figures 3 32 to 3 34, an example of the simulated spectrum between 200 nm and 800 nm are shown at 200 μm above the target surface in the S_{1c} case, see table 3 1 At 20 ns, the characteristic continuum is clear and lowers very rapidly and the discrete emission begins to dominate
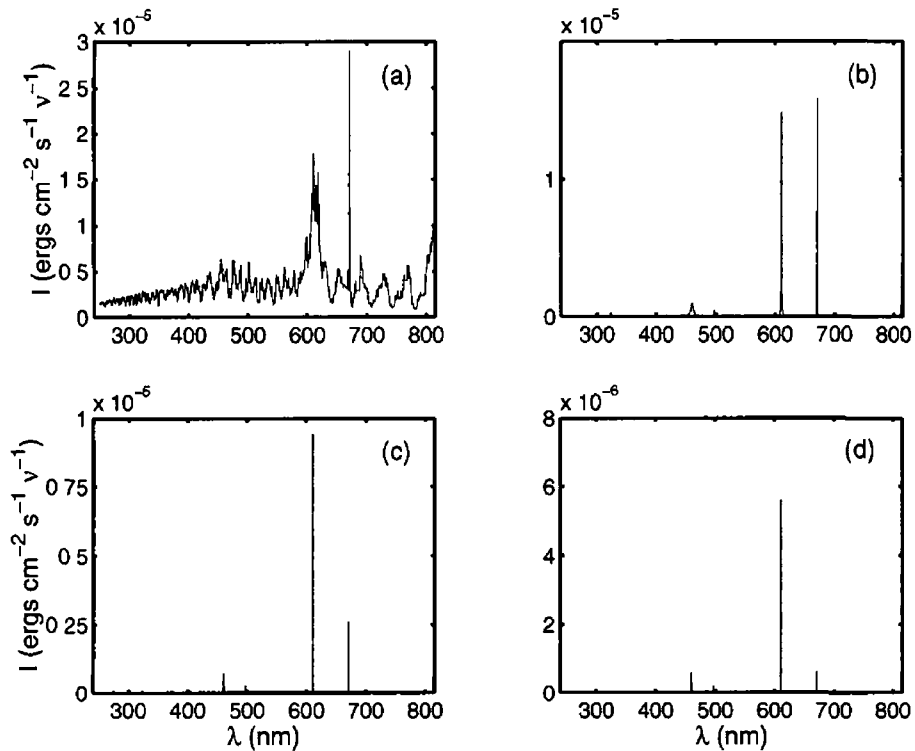

Figure 3 32 An example of the lithium spectrum (between 200 nm and 800 nm) evolving in time at a position of 200 μm above target in the set of conditions S_{1a} at times (a) 20 ns, (b) 40 ns, (c) 60 ns and (d) 80 ns
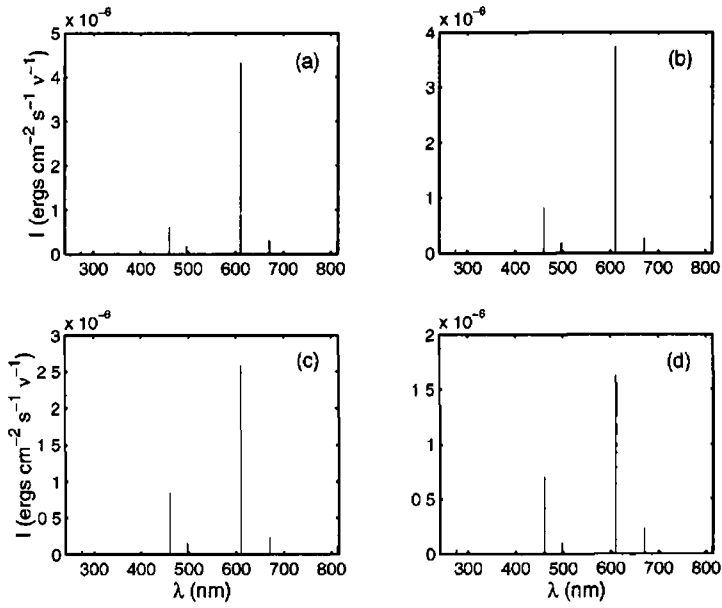
103

Figure 3 33 Same as figure at 3 32 at 2 mm above target at times (a) 100 ns, (b) 120 ns, (c) 140 ns and (d) 160 ns
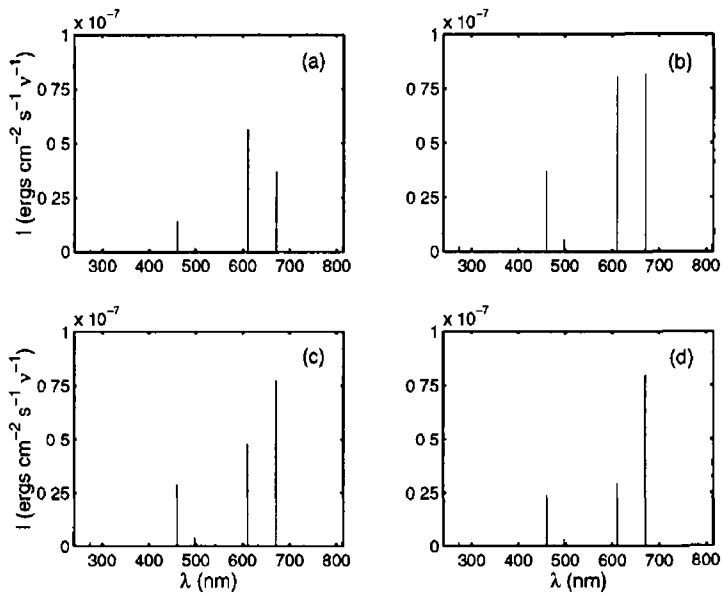

Figure 3 34 Same as figure at 3 32 at 5 mm above target at times (a) 200 ns, (b) 220 ns, (c) 240 ns and (d) 260 ns

3.4.2 Emission Spectra

In this section, experimental spectra obtained for the set of initial conditions S_{1c} will be analysed These spectra were taken at different heights above the target surface and along chords through the target normal axis These spectra concentrate on the visible region between 600 nm and 700 nm, see table 2 2 2 for the transitions of Li^0 in this wavelength region

Figure 3 35 show experimental time-integrated spectra taken at two positions, 1 mm and 6 mm, above the target surface In a typical situation of local thermal equilibrium, these spectra would be expected to indicate strong emission in the case of the 671 nm, 2p→2s line (L1) compared to the 610 nm, 3d→2p emission line (L2), since 671 nm corresponds to the wavelength of the resonance transition for Li^0 A temperature of $\approx$ 4 eV is the minimum temperature required before the 3d level population would become larger than that of 2p, for lithium neutral in local thermodynamic equilibrium conditions In the case presented here, the plasma temperatures remain well below this value, generally less than 1 eV, where synthetic spectra are generated Characteristics of the L1 and L2 transitions are shown in figure 2 2 2 However, it is clear that it is L2 that is dominant in the spectrum measured at 1 mm above target and at 6 mm L1 becomes comparable to L2 We will use our model to generate the corresponding synthetic spectra and, thus, provide an explanation for this apparent anomaly in the relative line intensities

This is not the first time that this line ratio 'anomaly' has been observed Other time-integrated experiments, carried out by Alan McKiernan (PhD student at Dublin City University) in the Institute de Optico in Madrid in Lithium Flouride (ablated with an ArF laser at 193 nm), yielded the same behaviour See figure 3 36, for an example of these results taken at 1 mm and 6 mm above target at a fluence of about 6 Jcm^{-2} on a spot of rectangular dimensions 1 5×0 5 mm This
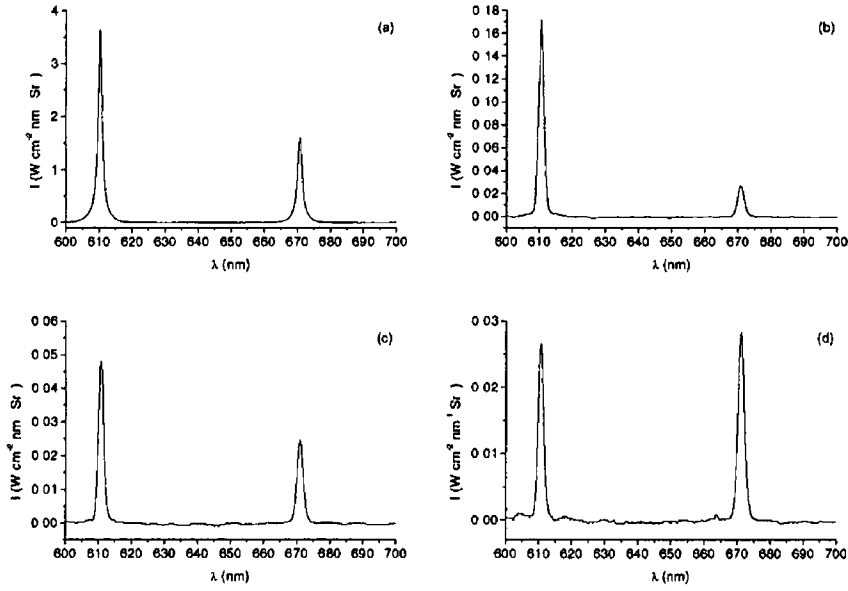
105

Figure 3 35 Time-integrated experimental spectra for Li^0 taken at (a) 1 mm, (b) 3 mm, (c) 5 mm and (d) 6 mm above the target surface in conditions S$_{1c}$
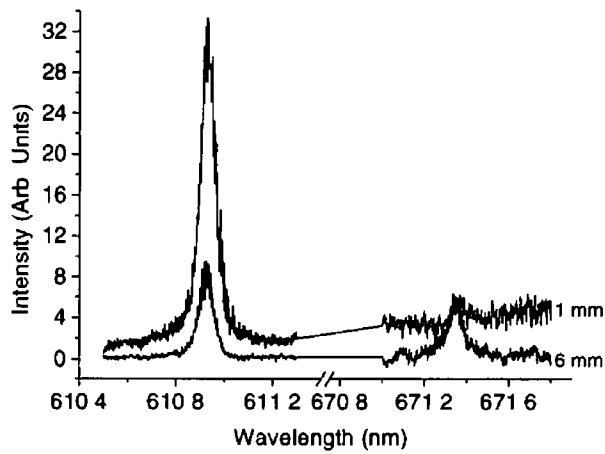
Figure 3 36 Sample time-integrated experimental spectra for LiF (laser wavelength of 193 nm) taken at 1 mm and 6 mm above the target surface

106

behaviour was also reported in [68, 69] for the case of a LiAg target, 6×6 mm spot, coated in Pt was ablated at a fluence of 0 7 Jcm^{-2} and in [70], in a Lithium Flouride plasma plume created with an excimer laser operating at 193 nm at a fluence of 6 Jcm^{-2}

The cause of this line ratio 'anomaly' seen at 1 mm above target is not immediately clear One possibility is the presence of non-steady state conditions in the plume, which was the interpretation in [68, 69] These authors interpreted that this 'anomalous' ratio was caused by time-dependent effects where a "bottle-neck level" is created in the 3^2d state, since, if steady-state is invalid, the rates do not adjust instantaneously with changes in n_e and T_e, as they would in the steady-state case Hence, if the plasma is not in steady-state the L2 (610 nm) line intensity may become larger than that of L1 (671 nm)

Another possible cause of this pattern, is that opacity effects play an important role in the emission More precisely, that L1 is more strongly absorbed than L2 by the expanding plasma, particularly at higher densities, which was the conclusion of the authors in [70] In the following these two possibilities for the cause of this anomaly in our case will be tested

To test for opacity effects, the full radiative tranfer equation was solved at 1 mm above target along the plume diameter The radiative transfer equation was also solved assuming optically thin plasma by setting the absorption coefficients to zero

Figures 3 37 to 3 41 show the time resolved numerical evaluations of these spectra using the exact solution, and with the absorption coefficients set to zero All of these spectra have been convolved with a Gaussian instrument profile of full width half maximum of 1 96 nm and 1 60 nm for L1 and L2, respectively, in line with experimental full width half maxima at 6 mm above target, see figure 3 35 These spectra indicate that opacity has a small effect on the line intensities but the

107
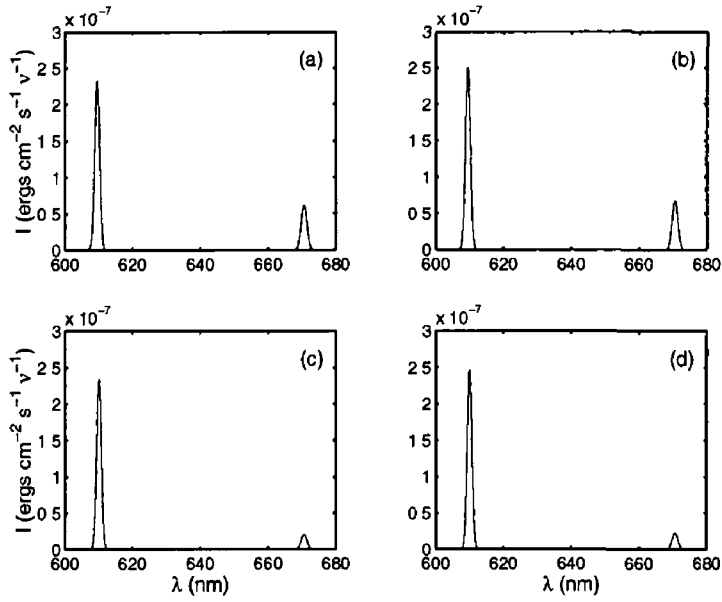
Figure 3 37 Synthetic spectra at 1mm above target surface for times 60 ns, (a) and (b), and 80 ns, (c) and (d) Solution to full radiative transfer (a) and (c), and optically thin solution (b) and (d)

Figure 3 38 Same as figure 3 37 for times 100 ns, (a) and (b), and 120 ns, (c) and (d)

Figure 3 39 Same as figure 3 37 for times 140 ns, (a) and (b), and 160 ns, (c) and (d)

Figure 3 40 Same as figure 3 37 for times 180 ns, (a) and (b), and 200 ns, (c) and (d)

Figure 3 41 Same as figure 3 37 for times 220 ns, (a) and (b), and 240 ns, (c) and (d)

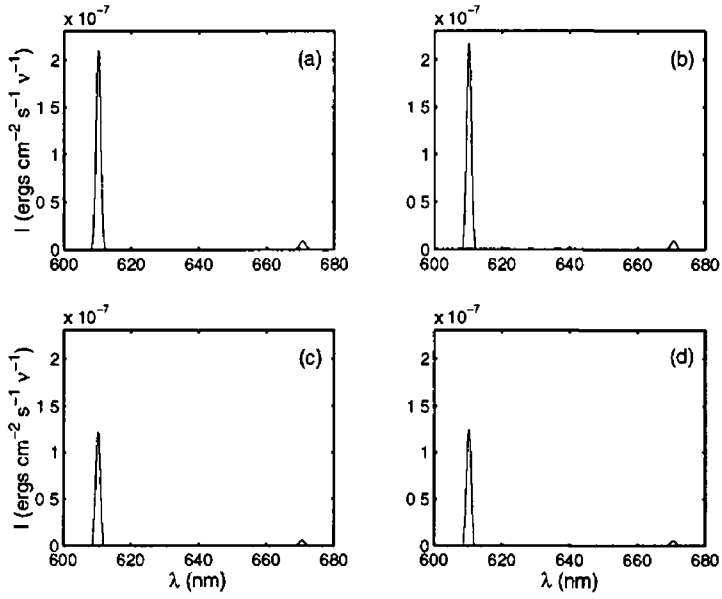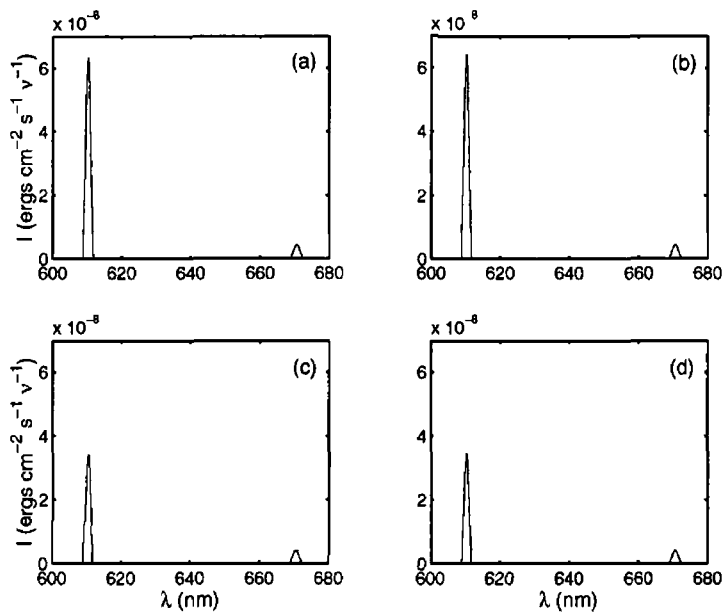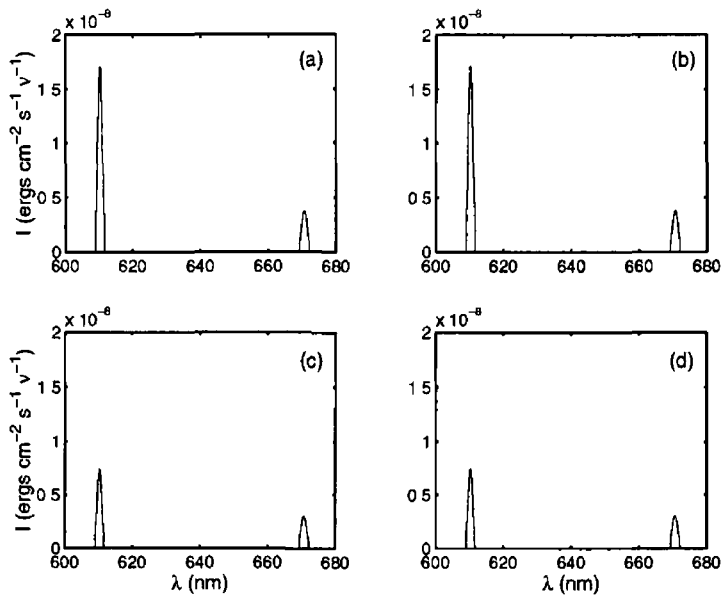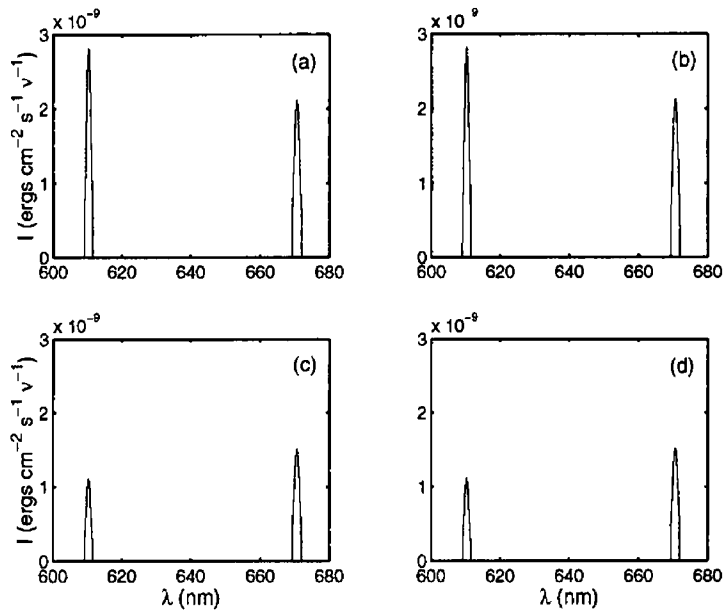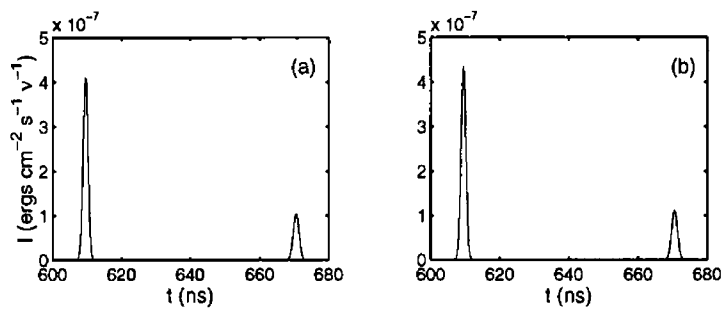Figure 3 42 Time integrated spectrum at 1 mm above target in set of initial conditions S_{1c} (a) Solution to full radiative transfer and (b) optically thin solution

110

anomalous line ratio is still predicted in both cases from which, we conclude that opacity effects alone cannot account for the overall relative line intensities

In the present conditions, time-independence was validated, see section 3 2 1 The line ratio anomaly is, thus, predicted here within the framework of a steady-state model We conclude that another factor must influence the observed line ratio, and that time-dependence effects alone appear not to be the cause of this anomaly
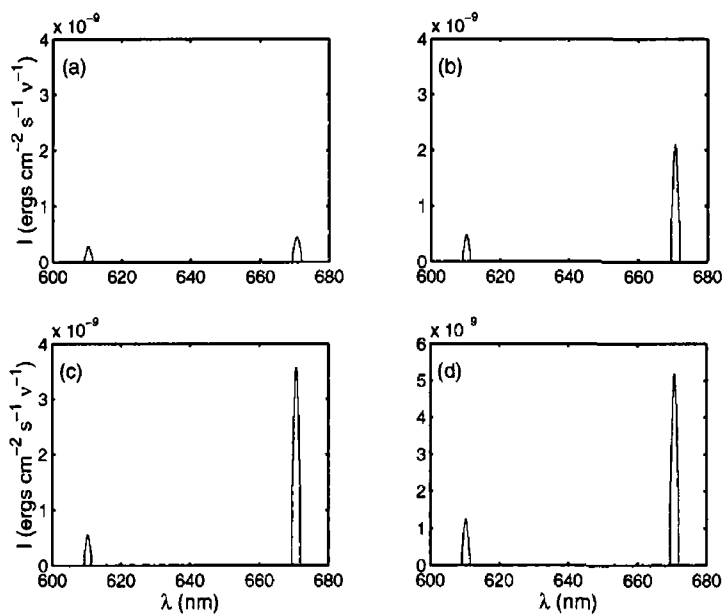
Figure 3 43   Synthetic spectra at 6 mm above target surface for times (a) 240 ns, (b) and 270 ns, (c) 300 ns and (d) Time integrated spectrum at 6 mm

As the plasma expands and the plume becomes more dilute so that the density decreases, time dependent effects should become more apparent, since τ_{coll} and λ_{mfp} become close to τ_{char} and λ_t, see section 3 2 1   Figure 3 41 shows that our model predicts the line ratio to return to the originally "expected" value at about 220 ns where the 670 nm line intensity is larger Since this is still within

111

the steady-state region applicable, see section 3 2 1, this further indicates that time dependence effects alone would be insufficient to explain the observed line intensity inversion Also, the experimental spectrum of figure 3 35 shows that L1 becomes comparable to L2 at positions, 6 mm here, much further from the target surface, where the density and temperature would be lower, on average, than at 1 mm above target Figure 3 43, shows the corresponding time resolved synthetic spectrum for comparison It is seen that the measured pattern shows the L1 intensity being close to that of L2, while the steady state model predicts that the L1 intensity is greater than that of L2 This further indicates that time dependent effects alone are insufficient to explain the observed line intensity ratio reversal

Figure 3 44 Time history of (a) Number of spontaneous emission transitions into levels 2^2p ($-\square-$) and 3^2d ($-\circ-$) per unit volume per second (b) Number of spontaneous emission transitions out of levels 2^2p ($-\square-$) and 3^2d ($-\circ-$) per unit volume per second (c) Level population densities of levels 2^2p ($-\square-$) and 3^2d ($-\circ-$) (d) Electron density All are displayed as a function of time at 1 mm above target on the target normal axis

112

Finally, it appears that the solution to this puzzle must be contained explicitly in the values of the rate coefficients, which populate and depopulate the energy levels These are strongly dependent on the results provided by the hydrodynamics Figures 3 44 to 3 46 display the electron density, level populations and rates populating and depopulating the relevant upper levels, 2^2p for L1 and 3^2d for L2, as a function of time at 1 mm above the target surface on the target normal axis
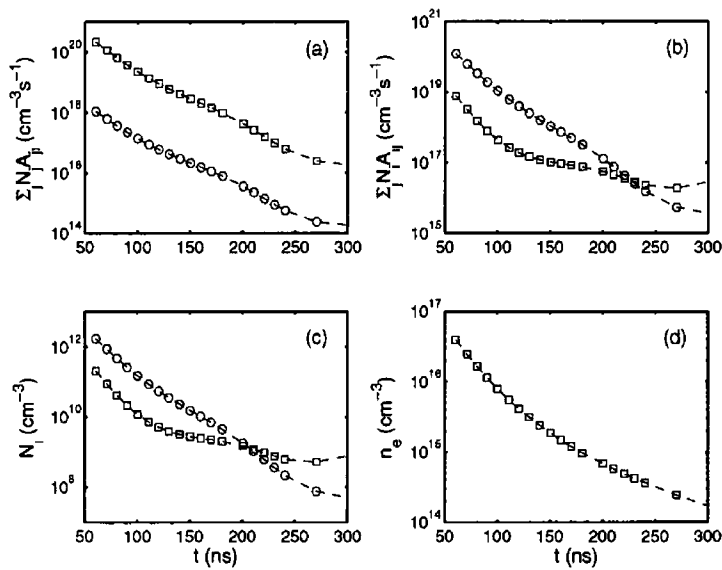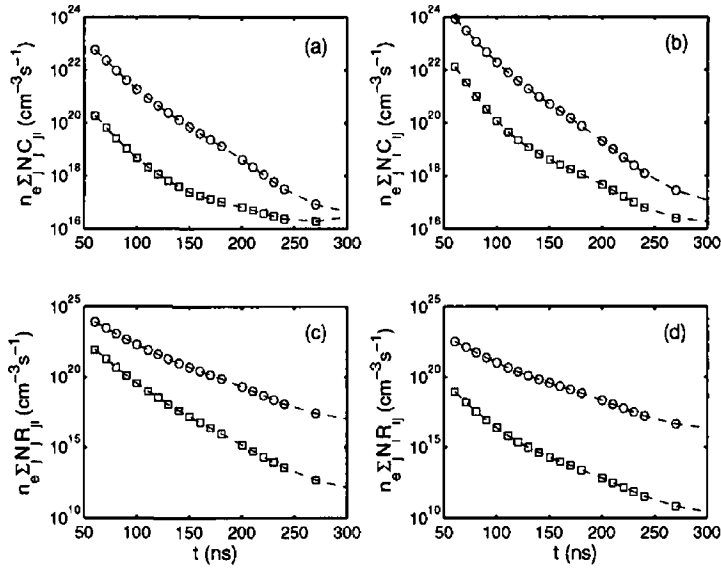

Figure 3 45 Time history of (a) Number of collisional excitations into levels 2^2p ($-\square-$) and 3^2d ($- \circ -$) per unit volume per second (b) Number of collisional excitations out of levels 2^2p ($-\square-$) and 3^2d ($- \circ -$) per unit volume per second (c) Number of collisional deexcitations into levels 2^2p ($-\square-$) and 3^2d ($- \circ -$) per unit volume per second (d) Number of collisional deexcitations out of levels 2^2p ($-\square-$) and 3^2d ($- \circ -$) per unit volume per second All are displayed as a function of time at 1 mm above target on the target normal axis

From these figures, it becomes clear that for sufficiently high electron densities the total impact of the other coefficients is much higher than that of spontaneous transitions It is when spontaneous transitions out of the levels of interest become significant, for $n_e \approx 10^{15}$ (around 200 ns), that the population inversion of these

113

two levels is reversed, see figure 3 41 This signature is clear on the time resolved synthetic spectra From these figures, it also becomes clear that the electron density remains relatively high, $> 10^{14}$, for a long period during the expansion, see figure 3 27, and by the time that the population inversion relents, the intensities of these lines will have diminished so much that they will have a negligible impact on the intensities of the time-integrated spectrum, see figure 3 42

In [68, 69], it was also shown that the intensity of L1 dominates at very early times and very close to target ($t = 50$ ns, $x = 170$ μm) and that this situation is reversed at $t = 75$ ns and $x = 450$ μm This situation is plausible and may occur if the
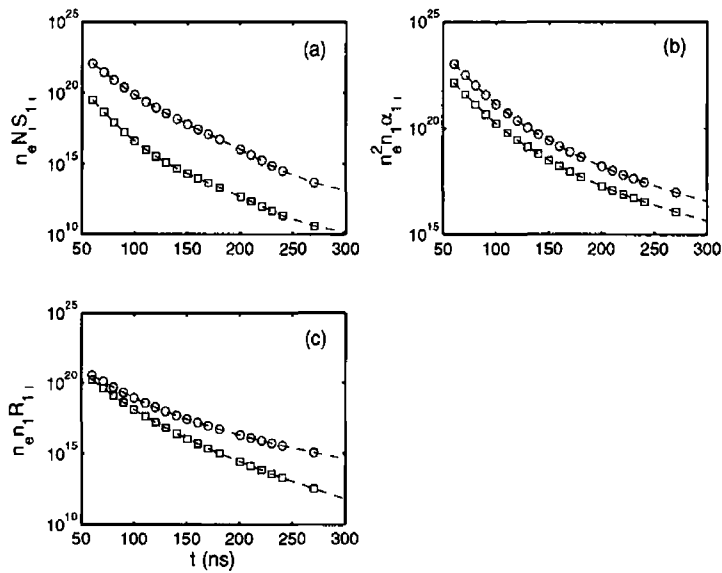
Figure 3 46 Time history of (a) Number of collisional ionizations out of levels 2^2p (−□−) and 3^2d (− ○ −) per unit volume per second (b) Number of three body recombinations into levels 2^2p (−□−) and 3^2d (− ○ −) per unit volume per second (c) Number of radiative recombinations into levels 2^2p (−□−) and 3^2d (− ○ −) per unit volume per second All are displayed as a function of time at 1 mm above target on the target normal axis

plasma is initially in a state of LTE where a Boltzmann distribution of level populations will occur To test for this situation in our conditions, synthetic spectra

has been generated at 0 5 mm above the target surface where we are much closer to LTE conditions since the plume will expand to this point earlier than to 1 mm, see figure 3 23 The results of these calculations are shown in figure 3 47 In figure 3 47(a) and (b), line L2 appears shifted to lower wavelengths This is due to continuum effects around 600 nm when the continuum contribution is significant,
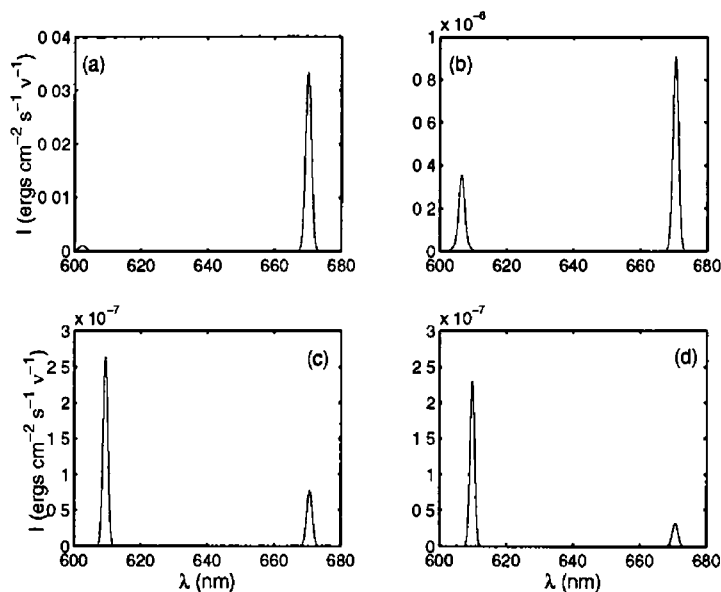
Figure 3 47 Synthetic spectra at 0 5mm above target surface for times (a) 30 ns, (b) and 40 ns, (c) 60 ns and (d) 70 ns

so that once L2 is convoluted may shift the peak intensity This effect of continuum on L2 is clear on figure 3 32(a), where this line has not been convolved and, as time progresses, the role of continuum emission becomes negligible In figure 3 47, the intensity of line 1 is initially larger before reverting to the case where line 2 becomes stronger at a time of about 55 ns Although, this is just outside the LTE spatial domain, it shows that the departure from LTE conditions may be estimated using this type of method In the sample synthetic spectrum at 200 μm above target at 20 ns, see figure 3 32, there is a portion of the plume in LTE con-

ditions, see figure 3 23 This spectrum shows a higher maximum intensity for L1, but the L2 line is much broader

This indicates a population inversion in some region of the plume and shows that emission spectra may be used to analyse plume spatial domains of LTE validity From these arguments, it is possible that the results shown in [68,69], where L1 is the dominant line at early times and close to the target surface before the line ratio is reversed, may be attributed to initial LTE conditions For a full and comprehensive answer to the problem of the line intensity anomaly, a comparison of a time dependent collisional radiative model to the time independent model is required in the conditions presented here and is a subject for future work

Chapter 4

Conclusions

In this work a full numerical model has been created to describe the expansion dynamics of a Li ablation plume in vacuum This model incorporates three main areas, hydrodynamics, atomic physics and spectroscopy

The hydrodynamics was analysed from isothermal and isentropic self-similar viewpoints with both models successfully modified to include the evolution of the plume position of maximum density via the bulk motion of the plume A best-fit procedure was applied to results from gated ICCD photography to analyse the hydrodynamics predictions of two self-similar expansion models

The fluence and laser wavelength were varied in the case of the smallest spot size of 50 μm The effect of laser wavelength was apparent through the significantly higher absorbance at 266 nm However, it appeared that as the wavelength and fluence were increased, the differing target absorbance became insignificant compared to effects resulting from the raised fluence and plasma absorbance

The initial spot radius was also varied over a wide range, varying between 50 μm and 1 mm As the spot radius increases from tens to hundreds of μm, there is a transition from an isothermal to isentropic self-similar solution as the more accurate model to predict the expansion dynamics The cause was attributed to the

117

increased initial pressure in the direction of smaller dimension (normal to target) as the laser spot radius is increased, and that large temperature gradients are more likely in the larger initial plume where the thermalization time may be increased

The method used for the plume bulk motion, calculating the position of maximum density, also shows quite a good agreement with the position of maximum luminosity observed experimentally Values calculated for pressure on target indicated reasonable compatibility with values published in the literature, where the pressure was calculated using the dynamic source effect

The connection of hydrodynamics to atomic kinetics enabled the analysis of applicability regions for various simplified equilibrium models It was shown that these simplified models are, generally, unsuitable for Li plumes in the conditions typical of pulsed laser deposition We explicitly evaluated the range of applicability of LTE in the lithium expansion plumes studied as a function of space and time It was seen that LTE is restricted to early times and limited portions of the expanding plume The atomic kinetics was calculated assuming time independence, i e steady state behaviour, and this assumption was analysed showing the space and time resolved region of its validity All subsequent calculations were performed within these regions of applicability Using the atomic kinetics, it was also possible to calculate space and time resolved electron, ion and energy level populations, which were then used to solve the full radiative transfer equation

The full radiative transfer equation was evaluated one-dimensionally along chords through the plume diameter This was employed to analyse time-integrated experimental spectra, which had yielded a counter-intuitive line ratio This ratio had been previously reported in the literature and had been ascribed to opacity effects or the prevalence of non steady-state conditions in the plume However, the model was successfully used to exclude these possibilities so that the cause was contained within the rates populating and depopulating the levels involved

118

in this ratio, rather than opacity or time dependant effects If LTE conditions were present in the plume, this ratio would not be seen in steady state optically thin plume conditions at the temperatures of interest in this work It was shown that when LTE conditions are present early in the expansion that this ratio is not observed in the synthetic spectra and indicates a possible use of this line ratio "anomaly" to characterize LTE conditions in Li ablation plumes

There is an abundance of future work possible to enhance and improve the current model It could be improved to consider other elements used as the target material and, with the availability of the various atomic cross-sections, a general full model of this kind would be possible The inclusion of a background gas would enhance the general use of the the plume expansion model Also the model could be improved to allow for multi-element targets, the rate equations for the different elements would be solved separately, from a common pool of electrons

The model used here is only valid where steady state conditions apply A further improvement would be obtained by generalizing this model so that it is applicable where non steady state conditions prevail at late times of the expansion However, this would also question the validity of a continuum hydrodynamics model to predict the dynamics of the expanding plume and induce the requirement of a more generally applicable expansion model, i e kinetic theory (Boltzmann equation)

This model only applies to plasmas containing up to doubly ionized atoms and the extension of the included ionization stages would require the solution of higher order equations in the calculation of electron densities However, if average rates for ionization and recombination between ionization stages were replaced by the individual rates connecting levels the only obstacle would be in regard to the availability of measured atomic cross-sections

The full radiative transfer equation could also be modified to allow chords

in any direction through any portion of the plume to be used, where refractive effects of light as it travels through the plume are included, to predict and interpret experimentally observed spectra

Appendix A

Appendices

A.1   Runge-Kutta Method

A.1.1   Solution to Hydrodynamics Models

In the hydrodynamics expansion models, in both the isothermal and isentropic cases, the flow is considered to be constant on the moving plume surface Hence, the hydrodynamics equations reduce to three coupled second order differential equations that can be written

$$X\frac{\delta^2 X}{\delta t^2} = Y\frac{\delta^2 Y}{\delta t^2} = Z\frac{\delta^2 Z}{\delta t^2} = \beta \left(\frac{X_0 Y_0 Z_0}{XYZ}\right)^{\gamma-1} \tag{A 1}$$

where X, Y and Z are the plume dimensions and the 0 indicates initial conditions at time $t = 0$, β is $(5\gamma - 3)E/M$ and $(1 - \gamma)E/M$ in the isentropic and isothermal cases, respectively

In both cases, the Runge-Kutta 5th order method has been implemented to solve equation A 1 The general form of this type of solution yields the following array of equations [71]

$$k_1 = hf(x_n, y_n)$$

$$k_2 = hf(x_n + a_2 h, y_n + b_{21}k_1)$$

$$k_3 = hf(x_n + a_3 h, y_n + b_{21}k_1 + b_{32}k_2)$$

$$k_4 = hf(x_n + a_4 h, y_n + b_{41}k_1 + b_{42}k_2 + b_{43}k_3)$$

$$k_5 = hf(x_n + a_5 h, y_n + b_{51}k_1 + b_{52}k_2 + b_{53}k_3 + b_{54}k_4)$$

$$k_6 = hf(x_n + a_6 h, y_n + b_{61}k_1 + b_{62}k_2 + b_{63}k_3 + b_{64}k_4 + b_{65}k_5)$$

$$y_{n+1} = y_n + c_1 k_1 + c_2 k_2 + c_3 k_3 + c_4 k_4 + c_5 k_5 + O(h^6) \qquad \text{(A 2)}$$

To ensure that this algorithm retains a high level of accuracy requires the use of adaptive step-size control, which achieves some predetermined accuracy in the solution with minimum computational effort The method used here was originally developed by Fehlberg and is based on embedded Runge-Kutta formulae Fehlberg discovered the fifth-order method with six function evaluations, equation A 2, with another combination of the six functions, k_i, giving a fourth order method and the difference between the two estimates may be used to estimate the truncation error to adjust the stepsize The embedded fourth-order equation is written

$$y_{n+1}^* = y_n + c_1^* k_1 + c_2^* k_2 + c_3^* k_3 + c_4^* k_4 + c_5^* k_5 + O(h^6) \qquad \text{(A 3)}$$

so that the error estimate becomes

$$\Delta \sim y_{n+1} - y_{n+1}^* = \sum_{i=1}^{6} (c_i - c_i^*) k_i \qquad \text{(A 4)}$$

The values of the various constants were calculated by [72] and are displayed in table

122

i	a_i	b_{ij}					c_i	c_i^*
1							$\frac{37}{378}$	$\frac{2825}{27648}$
2	$\frac{1}{5}$	$\frac{1}{5}$					0	0
3	$\frac{3}{10}$	$\frac{3}{40}$	$\frac{9}{40}$					$\frac{18575}{48384}$
4	$\frac{3}{5}$	$\frac{3}{10}$	$-\frac{9}{10}$	$\frac{6}{5}$			$\frac{125}{594}$	$\frac{13525}{55296}$
5	1	$-\frac{11}{54}$	$\frac{5}{2}$	$-\frac{70}{27}$	$\frac{35}{27}$		0	$\frac{277}{14336}$
6	$\frac{7}{8}$	$\frac{1631}{55296}$	$\frac{175}{512}$	$\frac{575}{13824}$	$\frac{44275}{110592}$	$\frac{253}{4096}$	$\frac{512}{1771}$	$\frac{1}{4}$
$j=$		1	2	3	4	5		

Table A 1 Cash-Karp parameters for the embedded Runge-Kutta method

A.2 Romberg Integration Method

In the Romberg scheme, a triangular array of entries is generated, where each entry is an approximation to the integral

$$I(y) = \int_a^b f(x)dx \qquad (A\ 5)$$

Consider the approximate formula for the integral, equation A 5,

$$A_{n,k} = \frac{h}{2}\left[f(a) + f(b) + 2\sum_{j=1}^{n} f(a + jh) \right] \qquad (A\ 6)$$

with the step-size, h,

$$h = \frac{b - a}{2^{k-1}} \qquad (A\ 7)$$

and

$$n = 2^{k-1} - 1 \qquad (A\ 8)$$

Equation A 6 is equivalent to a repeated trapezoidal rule and the Romberg method is a method of evaluating this formula Table A 2 displays a typical table

123

m=1	$A_{0,0}$			
m=2	$A_{0,1}$	$A_{1,0}$		
m=3	$A_{0,2}$	$A_{1,1}$	$A_{2,0}$	
m=4				
m=5	$A_{0,k}$	$A_{1,k-1}$	$A_{3,k-2}$	$A_{k,0}$

Table A 2 Array of entries, $A_{n,k}$, for the Romberg scheme

for the Romberg method, with the general formula for the entries given by [73]

$$A_{n,k} = \frac{1}{4^{n-1} - 1} \left(4^{n-1} A_{n-1,k+1} - A_{n-1,k} \right) \qquad \text{(A 9)}$$

The entry $A_{n,k}$ is in the $(n + 1)th$ position of the $(k + 1)th$ column $(n, k = 0, 1, 2, \ )$ The entry $A_{0,j}$ in the first column is obtained by repeating the trapezoidal rule $m\lambda$ times, where $m = 2^j$ and λ is fixed Hence, increasing points in the trapezoid rule goes down the left side, and increasing extrapolation goes along the diagonal The process stops when two successive estimates on the diagonal agree

This integration method has been used to evaluate equations 1 31 in the calculation of the position of maximum density and also in the calculation of the electron impact excitation coefficient, see section 2 3 4   The computer program used to implement this integration method was adapted from [71]

124

Bibliography

[1] B M Smirnov *Physics of Ionized Gases* John Wiley and Sons, New York, 2001

[2] F F Chen *Introduction to Plasma Physics and Controlled Fusion* Plenum Press, New York, 1984

[3] T P Hughes *Plasmas and Laser Light* Adam Hilger, London, 1975

[4] J C Miller and D B Geohegan(Eds) *AIP Conference Proceedings 288, Laser Ablation and Applications II* AIP Press, New York, 1993

[5] E D Palik *Handbook of Optical Constants of Solids II* Academic Press, London, 1991

[6] S Amoruso, R Bruzzese, N Spinelli, and R Velotta *J Phys B At Mol Opt Phys*, 32 R131–R172, 1999

[7] E Hecht *Optics, Third Edition* Addison-Wesley, New York, 1998

[8] H Hora Technical report, Rensselaer Polytechnic Institute, Hartfordshire Graduate Center, June 9-13, 1969

[9] A F Haught and D H Polk *The Physics of Fluids*, 9,10 2047–2056, 1966

[10] P Kaw J Dawson and B Green *The Physics of Fluids*, 12,4 875–882, 1969

125

[11] K R Chen, J N Lebeouf, R F Wood, D B Geohegan, J M Donato, C L
Liu, and A A Puretzky *Physical Review Letters*, 75,25 4706–4709, 1995

[12] H Hora *Plasmas at High Temperature and Density Applications and Im-
plications of Laser-Plasma Interaction* Springer-Verlag, Berlin, New York,
1991

[13] P Loiseleur, T N Hansen, J Larour, and J G Lunney *Appl Surf Sci*, 197-
198 164–168, 2002

[14] G J Pert *J Fluid Mech*, 100,2 257–277, 1980

[15] S I Anisimov, D Bauerle, and B S Luk'yanchuk *Physical Review B*,
48,16 12076–12081, 1993

[16] W J Fader *The Physics of Fluids*, 11,10 2200–2207, 1968

[17] R K Singh and J Narayan *Physical Review B*, 41,13 8843–8859, 1990

[18] G A Bird *Molecular Gas Dynamics and the Direct Simulation of Gas
Flows* Oxford Science Publishers, New York, 1994

[19] I NoorBatcha, R Lucchese, and Y Zeiri *Journal of Chemical Physics*,
86,10 5816–5824, 1987

[20] A Miotello and R Kelly *Applied Physics A*, 69[Suppl] S67–S73, 1999

[21] R Kelly and R W Dreyfus *Surface Science*, 198 263–276, 1988

[22] R Kelly and R W Dreyfus *Nuclear Instruments and Methods in Physics
Research*, B32 341–348, 1988

[23] P K Wu, B R Ringeisen, D M Bubb, R C Y Auyeung, J Horwitz, E J
Houser, A Pique, R A McGill, and D B Chrisey *Journal of Applied
Physics*, 90,7 3623–3631, 2001

[24] W Guan, T Matsumoto, and T Kawai *Chemical Physics Letters*, 291 161–166, 1998

[25] F E Irons *Journal of Quantitative Spectroscopy and Radiative Transfer*, 22 1, 1979

[26] S Suckewer *Physical Review*, 170,1 239–244, 1968

[27] J A Kunc *Journal of Applied Physics*, 63 656–664, 1988

[28] D Colombant and G F Tonon *Journal of Applied Physics*, 44,8 3524–3537, 1973

[29] J Cooper *Report on Progress in Physics*, 29,1 36–130, 1966

[30] D Salzmann *Atomic Physics in Hot Plasmas* Oxford University Press, New York, 1998

[31] http //www physics nist gov/

[32] R Dendy *Plasma Physics* Cambridge University Press, Cambridge, 1993

[33] T Fujimoto and R W P McWhirter *Physical Review A*, 42,11 6588–6601, 1990

[34] H R Griem *Principles of Plasma Spectroscopy* Cambridge University Press, Cambridge, 1997

[35] M Arnaud and R Rothenflug *Astronomy and Astrophysical Supplement Series*, 60 425–457, 1985

[36] H A Kramers *Philosophy Magazine*, 46 836–871, 1923

[37] W Lochte-Holtegreven *Plasma Diagnostics* American Institute of Physics Press, New York, 1995

[38] A Corney *Atomic and Laser Spectroscopy* Oxford University Press, New York, 1977

[39] R D Cowan *The Theory of Atomic Structure of Spectra* University of California Press, Berkeley and Los Angeles, California, 1981

[40] A B McLean, C B Mitchell, and D M Swanston *Journal of Electron Spectroscopy and Related Phenomena*, 69 125–132, 1994

[41] A P Thorne *Spectrophysics, Second Edition* Chapman and Hall, New York, 1988

[42] G Bekefi *Principles of Laser Plasmas* Wiley and Sons, London, 1976

[43] H R Griem *Plasma Spectroscopy* McGraw-Hill, New York, 1964

[44] H R Griem *Spectral Line Broadening in Plasmas* Academic Press, New York, 1974

[45] http //mesunb obspm fr/cgi-bin/w3msql/firsta htm/

[46] F E Irons *Journal of Physics B Atomic and Molecular Physics*, 8,18 3044–3068, 1975

[47] F E Irons, R W McWhirter, and N J Peacock *Journal of Physics B Atomic and Molecular Physics*, 5 1975–1987, 1972

[48] Yu P Raizer and Ya B Zeldovich *Physics of Shock Waves and High-Temperature Hydrodynamic Phenomena* Academic Press, New York, London, 1966

[49] V I Mazhukin, V N Nossov, G Flamant, and I Smurov *Journal of Quantitative Spectroscopy and Radiative Transfer*, 73 451–460, 2002

[50] J R Ho, C P Grigoropoulos, and J A C Humphrey *Journal of Applied Physics*, 79,9 7205–7215, 1996

[51] F Garrelie, J Aubreton, and A Catherinot *Journal of Applied Physics*, 83,10 5075–5082, 1998

[52] K Mizuno, Y Masuyama, M Kiso, J Suzuki, and T Kobayashi *Applied Surface Science*, 197-198 490–493, 2002

[53] T E Itina, L Patrone, W Marine, and M Autric *Applied Physics A*, 69[Suppl] S59–S65, 1999

[54] S I Anisimov, B S Luk'yanchuk, and A Luches *Applied Surface Science*, 96-98 24–32, 1996

[55] K R Chen, T C King, J H Hes, J N Leboeuf, D B Geohegan, R F Wood, A A Puretzky, and J M Donato *Physical Review B*, 60,11 8373–8382, 1999

[56] D A Verner and G J Ferland *The Astrophysical Journal Supplement Series*, 103 467–473, 1996

[57] Y Hahn *Journal of Quantitative Spectroscopy and Radiative Transfer*, 49,1 81–93, 1993

[58] P Mazzotta et al *Astronomy and Astrophysics Supplement Series*, 133 403–409, 1998

[59] http //cdsweb u-strasbg fr/abstract html

[60] J Schweinzer, R Brandenburg, I Bray, R Hoekstra, F Aumayr, R K Janev, and H P Winter *Atomic Data and Nuclear Data Tables*, 72 239–273, 1999

[61] D C Griffin and D M Mitnik *Physical Review A*, 64 032718 1–6, 2001

[62] T N Hansen, J Schou, and J G Lunney *Applied Physics A*, 69 S601–S604, 1999

[63] M Aden and E W Kreutz *Applied Surface Science*, 96-98 39–44, 1996

[64] G J Pert *Plasma Physics*, 16 1051, 1974

[65] J Dawson *The Physics of Fluids*, 7,7 981–987, 1964

[66] F J Gordillo-Vazquez *Journal of Applied Physics*, 90,2 599–606, 2001

[67] http //heasarc gsfc nasa gov/topbase/xsections html

[68] M E Sherrill, R C Mancini, J E Bailey, A Filuk, B Clark, P Lake, and J Abdallah *SPIE Conference Proceedings*, 3935 14–22, 2000

[69] M E Sherrill, R C Mancini, J E Bailey, A Filuk, B Clark, P Lake, and J Abdallah *Review of Scientific Instruments*, 72,1 957–960, 2001

[70] S J Henley, M N R Ashford, and S R J Pearce *Applied Surface Science*, 217 68–77, 2003

[71] W H Press, S A Teukolsky, W T Vetterling, and B P Flannery *Numerical Recipes in C, Second Edition* Cambridge University Press, Cambridge, 1994

[72] J R and A H Karp *ACM Transactions on Mathematical Software*, 16 201–222, 1990

[73] C T H Baker *The Numerical Treatment of Integral Equations* Oxford University Press, Oxford, 1978